The Study of Shear and Longitudinal Velocity Measurements of Sands and Cohesive Soils

by

Jana Marjanovic

S.B. in Civil and Environmental Engineering, Massachusetts Institute of Technology, Cambridge, MA (2010)

Submitted to the Department of Civil and Environmental Engineering in partial fulfillment of the requirements for the degree of

Masters of Science in Civil and Environmental Engineering

at the

MASSACHUSETTS INSTITUTE OF TECHNOLOGY

June 2012

Author .....
Department of Civil and Environmental Engineering
May 11, 2012

Certified by .....
John T. Germaine
Senior Research Associate and Lecturer of Civil and Environmental Engineering
Thesis Supervisor

Accepted by .....
Heidi M. Nepf
Chair, Departmental Committee for Graduate Students

The Study of Shear and Longitudinal Velocity Measurements of Sands and Cohesive Soils

by

Jana Marjanovic

Submitted to the Department of Civil and Environmental Engineering
on May 11, 2012, in partial fulfillment of the requirements for the degree of
Masters of Science in Civil and Environmental Engineering

Abstract

This thesis evaluates some methods for the measurement of stiffness parameters of soils, with an emphasis on the use of bender element technology in obtaining the shear modulus. The experimental program consisted two primary stages. The beginning part of the experimentation was concerned with evaluating the behavior of bender elements, both free-standing and when applied to soil. For this case, experiments were performed on dry Ticino sand. It was concluded that the bender element tip geometry has a much greater impact than previously perceived, in particular with long, slender geometries sometimes creating directly-propagating compressional waves that interfere with the shear wave arrival detection. To reduce the uncertainty in signal interpretation, a specimen aspect ratio of 1 was adopted, with a minimum wavelength ratio of 2. The second part of the experimentation consisted of using bender elements on Boston Blue Clay, both intact samples as well as Resedimented Boston Blue Clay, created in the laboratory from processed powder. The results obtained from loading normally consolidated specimens were generally consistent and in good agreement with the literature. The unloading portion was observed to behaves differently as a function of maximum consolidation stress, with the shear modulus decreasing less during unloading as higher stress ranges are reached. In addition to the testing performed on soils, a parametric study was conducted on common materials including steel, aluminum, acrylic, and rubber in order to evaluate the results for stiffness parameters measured using extensometers, accelerometers, and ultrasonic P-wave transducers. With the conclusion of these experiments, the accelerometers were shown to have highly variable results, especially for shear wave velocity, while the other methods yielded relatively consistent, reliable results as compared to published values. Finally, a new design for a triaxial setup that enables integrated measurements of compressional and shear velocities in soil over a wide stress range is presented as groundwork for the characterization of the complete stiffness matrix of BBC.

Thesis Supervisor: John T. Germaine
Title: Senior Research Associate and Senior Lecturer of Civil and Environmental Engineering

Acknowledgments

First and foremost I would like to thank my research advisor, Dr. Germaine, for guiding me throughout the duration of my Master's. He was especially patient and always encouraging me whenever I hit a road-block.

A special thanks goes out to all the faculty and staff in the civil department at MIT. There are too many to list but I would like to acknowledge the geotechnical professors: Prof. Einstein, Dr. Jen, and Prof. Whittle. I have learned an incredible amount of information in the past few years from your classes. In addition, I am very grateful to Steve for all the help he has given me in the shop and taught me how to use all the tools I need.

I would like to thank all the people on the third floor, who have really made it a fun environment and I am thoroughly grateful for all the laughs we have shared. Off-campus, I would like to thank my roommate Sue for making our little household a never-ending bundle of joy.

Finally, I would like to thank all of those who listened to me whine and complain, and always had an ear and a shoulder whenever I needed them, including Amy, Brendan, Aiden, and especially Nick, who bore the brunt of it. Lastly, my family is largely to thank for all the things that I have accomplished, and I could not have done it without their everlasting support.

Contents

1 Introduction **17**

1.1 Problem Statement 17

1.2 Scope and Objectives 19

1.3 Organization 19

2 Background **23**

2.1 Introduction 23

2.2 Velocity Testing 24

2.3 History of Bender Element Testing 27

2.4 Applications of Bender Elements 28

2.5 3D Velocity Behavior 29

2.6 Methods of Obtaining the Shear Modulus 32

2.6.1 Resonant Column 32

2.6.2 Torsional Shear 33

2.6.3 Triaxial Apparatus 34

2.6.4 Bender Elements 34

2.7 Comparing Different Methods 35

3 Materials and Specimen Preparation **53**

3.1 Materials 53

3.2 Ticino Sand 53

3.2.1 Procedures and Experimental Setup 54

3.3 Boston Blue Clay 55

3.3.1 Sample Preparation 57
3.3.2 Resedimentation 57
3.3.3 Stages of Resedimentation 57
3.3.4 Experimental Setup 59

4 Testing Equipment **73**
4.1 Introduction to Laboratory Equipment 73
4.2 Bender Elements 73
4.2.1 Introduction 73
4.2.2 Description of Equipment Characteristics 74
4.2.3 Data Acquisition System 78
4.2.4 Spring System 80
4.3 P-wave Transducers 80
4.3.1 Introduction 80
4.3.2 Description of Equipment Characteristics 80
4.3.3 Data Acquisition System 81
4.4 Accelerometers 82
4.4.1 Introduction 82
4.4.2 Description of Equipment Characteristics and Experiment . . 82
4.4.3 Data Acquisition System 83
4.5 Extensometers 84
4.5.1 Introduction 84
4.5.2 Description of Equipment Characteristics and Experiment . . 84
4.5.3 Data Acquisition System 85
4.6 New Equipment Development 85
4.6.1 Introduction 85
4.6.2 Triaxial Setup 86
4.6.3 Data Acquisition 87
4.6.4 Square Triaxial Endcaps 87

5 Investigation of Variables that Affect Bender Element Measurements **105**

5.1 Frequency Effect 105

5.1.1 Bender Element Frequency Behavior 105

5.1.2 Frequency Effect on Modulus Results 106

5.2 Bender Element Tip Geometry 107

5.3 Specimen Boundary Effects 109

5.3.1 Geometric Ratios 109

5.3.2 Ray Path Analysis 111

5.3.3 Soft vs. Hard Boundary 113

5.4 Stress Effect on Output Signal 114

5.5 Lag in Response 115

6 Data Analysis Methods **131**

6.1 Arrival Time Selection 131

6.1.1 Time Domain 132

6.1.2 Cross-Correlation 133

6.1.3 Frequency Domain 134

6.1.4 Comparison of Different Methods 134

6.2 Square versus Sinusoidal Wave Input 135

6.2.1 Bender Elements 136

6.2.2 Ultrasonic Transducer 136

7 Results and Discussion **141**

7.1 Ticino Sand Results 145

7.1.1 Ticino Sand Velocity and G_{max} measurements 145

7.1.2 Comparison with Published Data 147

7.2 Boston Blue Clay 148

7.2.1 Compression Behavior 148

7.2.2 In situ v. Resedimented Behavior 149

7.2.3 Comparison with Published Data 150

7.2.4 OCR Effect 151
7.3 Anisotropy Measurements in Clay 153
7.3.1 Evaluation of cross-anisotropic behavior 153
7.3.2 Anisotropy Results in Clay 154
7.3.3 SEM Image Analysis 156
7.4 Comparison of Different Methods of Measuring the Constrained Modulus, and Others 157

8 Conclusions and Further Research **179**
8.1 Summary of Conducted Work 179
8.2 Interpretation of Velocity Results 180
8.3 Equipment Effect on Stiffness Parameters 182
8.4 Future Work 182

List of Figures

2-1 BE compared to field results 40
2-2 Field results compared with other methods 41
2-3 Average Strain vs. Engineering Strain 42
2-4 Axis convention for wave propagation 42
2-5 Vertical propagation through cross-anisotropic medium 43
2-6 Vertical propagation through cross-anisotropic medium 43
2-7 Strain effect on stiffness results 44
2-8 BE compared to others during parallel testing 45
2-9 BE compared to others during parallel testing 45
2-10 BE compared to others during parallel testing 46
2-11 BE compared to others during parallel testing 46
2-12 BE compared to others during parallel testing 47
2-13 BE compared to RC results 48
2-14 BE compared to RC and TS results 49
2-15 BE compared to RC and TS results 49
2-16 Comparison of RC and TS results for wet and dry conditions 50
2-17 Comparison of RC and TS results for wet and dry conditions 51

3-1 Preparation of sand specimen 61
3-2 Loading of sand specimen 62
3-3 Previous testing of BBC 63
3-4 Index properties of RBBC 64
3-5 GSD of RBBC 65

3-6 Components of slurry mixture 66
3-7 De-airing procedure 66
3-8 Funneling of the slurry into the floating tube setup 67
3-9 Settlement curve for RBBC 68
3-10 Beginning of resedimentation loading 69
3-11 Resedimentation setup loading increments 70
3-12 Bender element tips 71
3-13 Terzaghi load frame 72

4-1 Bender Element tip deflection 89
4-2 Bender Element tips with acrylic housing 89
4-3 Bender Element tips without housing and epoxy 90
4-4 Casting the bender elements in epoxy 91
4-5 Circuit diagram of BE testing 92
4-6 BE Data Acquisition System (DAQ) 93
4-7 Load application via springs 94
4-8 P-wave transducer housing 95
4-9 Ultrasonic P-wave transducer 95
4-10 Pulse Generator 96
4-11 Dual-axis accelerometer 96
4-12 Schematic of accelerometer and pin connections 96
4-13 Accelerometer dimensions 97
4-14 Accelerometer signal output 97
4-15 Test setup for accelerometer measurements 98
4-16 Closeup of extensometer 99
4-17 Test setup using extensometers 100
4-18 CAD of modified triaxial velocity measurement setup 101
4-19 Closeup of square endcap 102
4-20 Closeup of square endcap with porous stone 102
4-21 Square triaxial endcaps 103

4-22 Closeup of bender element and P-wave transducer 103

5-1 Frequency-dependent signal amplitude 116
5-2 Frequency response of bender element 117
5-3 Frequency response of bender element 117
5-4 Frequency-scale effect 118
5-5 Frequency effect under different boundary conditions 118
5-6 Frequency effect under different boundary conditions 119
5-7 Bender element tip geometry effect 120
5-8 Side-traveling P-waves from bender element 120
5-9 Bender element setup schematic 121
5-10 Near-field effect 121
5-11 Ray Path Analysis 122
5-12 Small diameter specimen 123
5-13 Medium diameter specimen 123
5-14 Large diameter specimen 124
5-15 Ray path analysis of 20cm diameter tube with Geometry A 125
5-16 Ray path analysis of 20cm diameter tube with Geometry B 126
5-17 CAR reflection for Geometry A 127
5-18 CAR reflection for Geometry B 127
5-19 Soft v. hard boundary 128
5-20 Displacement vs. force of bender element tip 129
5-21 Stress influence on bender element signal 130

6-1 Time domain method of travel time selection 138
6-2 Time domain method of travel time selection with varying frequency 138
6-3 Comparison of CC to TD 139
6-4 Different data analysis methods 139
6-5 A square wave used with bender elements 140

7-1 Ticino sand velocities with different widths 163

7-2 Ticino sand velocities with different widths 163
7-3 Ticino sand velocity measurements 164
7-4 Ticino sand velocity measurements 164
7-5 Ticino sand shear modulus measurements 165
7-6 Ticino sand shear modulus measurements for the different BE geometries 165
7-7 Ticino sand shear modulus measurements compared to published data 166
7-8 Compression curve of BBC specimens 167
7-9 Compression curve of BBC specimens 167
7-10 Velocity curves for resedimented v. natural BBC 168
7-11 Velocity curve of BBC specimens 168
7-12 Velocity curves of RBBC specimens 169
7-13 Shear modulus G_{max} curves of RBBC specimens 169
7-14 Triaxial testing with yolk attachment 170
7-15 Comparison of G_{max} results for BBC 170
7-16 Velocity curve for BE046 171
7-17 Velocity curve for BE047 171
7-18 Compression curve for BE046 172
7-19 Compression curve for BE047 172
7-20 Shear modulus curve for BE046 173
7-21 Shear modulus curve for BE047 173
7-22 Schematic of clay particles during loading 174
7-23 P-wave velocity of dry RBBC 175
7-24 P-wave anisotropy of RBBC 175
7-25 SEM Image of RBBC 176
7-26 SEM Image of RBBC 176
7-27 Constrained modulus values for various materials 177
7-28 Shear modulus values for various materials 177
7-29 Young's modulus values for various materials 178
7-30 Young's modulus values for various materials 178

List of Tables

2.1 Dynamic vs. Static testing 24
2.2 Modulus comparisons for different instrumentation 39

3.1 Ticino sand properties 54
3.2 Ticino sand properties 54

5.1 Bender element tip geometry 108
5.2 Travel times for different aspect ratios 112

7.1 List of Experiments 142
7.2 List of Experiments 143
7.3 List of Experiments 144
7.4 OCR effect on shear modulus 153
7.5 Constrained Modulus (M) for various materials 158
7.6 Shear Modulus (G) for various materials 159
7.7 Young's Modulus (E)for various materials 160

Chapter 1

Introduction

1.1 Problem Statement

Obtaining the elastic properties of soil has been a topic of interest in the geotechnical field for many decades and there have been continuing strides to improve the measurements and technology used to acquire these parameters. When dealing with highly nonlinear materials with very low yield strains such as clays, it becomes difficult to perform non-destructive experiments that remain within the range of elastic deformation, which is usually taken to be below 0.01% strain. Wave propagation, however, is a method that allows for the measurement of stiffness parameters while inducing very small amounts of strain, attributing to its widespread popularity.

The stiffness parameters obtained from wave propagation testing have many important applications. They facilitate a higher level of understanding of the basic natural behavior of soils, which can be translated to better predictions of how soil will behave in certain circumstances. During site characterization, the use of wave propagation becomes a vital component in obtaining elastic properties of soils, which allows for a more comprehensive insight into the conditions that will be encountered during construction. Moreover, they also aid in the development of an optimized construction of structures, both with respect to foundation design and construction sequencing. Finally, the wave propagation results can be used to develop models that describe soil behavior as a function of various parameters, including void ratio, stress

level, etc.

The great variability that exists between methods of modulus measurements has made it difficult to determine which technique provides the most accurate result, and moreover which one should be used in design. In addition, there have not been many systematic studies that develop a continuous relationship between stress level and shear modulus value, which is also the cause of an average value of shear modulus usually being used over a soil layer in the field that does not change as a function of the applied loading. This static value can foster inaccurate predictions that underestimate the stiffness likely faced in the field. Although it does introduce an inherent safety factor into the results, it does not allow for an optimized system of structural design. In additional, modulus values obtained in the laboratory are usually conducted in a singular direction, which then translates to modeling environments. The introduction of anisotropy can greatly refine the soil behavior predictions, which is one of the reasons why bender elements have been gaining popularity in recent years.

While bender elements have the advantage of providing shear modulus values for soft materials at a range of stress levels for a single specimen, as well as multiple directions, there are still some uncertainties regarding the reliability of bender element results. The signal interpretation aspect can lead to large errors. While there has been a great effort to shed light on the behavior of bender element technology with parallel studies and parametric studies, few institutions have looked at all the aspects concerned with bender element testing that would allow for an unambiguous velocity result, and no standards have been established.

Bender elements are valuable for measurements in soft materials that allow good coupling to occur between the bender element and surrounding soil. Little research has been conducted that looks at a very wide range of stress levels. Since there exists a limit at which the bender element can no longer overcome the confining lateral stresses that restrains it from deflecting, most bender element testing only covers a stress range of up to 400kPa. Conversely, ultrasonic transducers optimally perform at high stresses at which the soil has a high stiffness that overcomes the attenuative nature of soft materials. Hence the transitional range between the low and the high

stress levels has not been well-studied.

1.2 Scope and Objectives

One of the primary goals of this research has been to better understand the behavior of bender element technology and eliminate factors that can cause ambiguous signal interpretations leading to inaccurate shear modulus values. By conducting parametric studies and comparing the experimental results obtained in the laboratory with various other sources of published results, a testing environment was established for the bender elements that would provide consistent, reliable results.

Additionally, an investigation into the equipment effect on stiffness testing was of interest in order to compare well-established results of common materials such as metals and polymers. By using a variety of techniques, including accelerometers, extensometers, and ultrasonic transducers, a better understanding of how the equipment and electronics themselves yield different results when all other testing conditions and specimens are held identical.

The final aspect of this research consisted of establishing the groundwork needed to carry forward with multi-directional velocity testing that would allow for the characterization of the stiffness matrix of various clays. This entailed the design of a cubic triaxial setup that would allow for seamless velocity measurements in a controlled environment under K_0 conditions.

1.3 Organization

The sequence of this thesis is based on the intent to describe to the reader the relevant steps taken during the during of this research. This document is divided into eight chapters, which are described as follows.

Chapter 2 gives a summary on the background of bender element testing and how the development of this technology has evolved over the years. First, there is a brief introduction on the general principles of wave propagation and how they are applied

to bender elements. Next, an outline of why velocity testing is important and how it is applicable to the field. Finally, a literature review is conducted that compares different experimental works, all of which used bender elements in some capacity.

Chapter 3 introduces the materials, which includes Boston Blue Clay (BBC) and Ticino sand, used during this research, as well as how they are processed and the specimen preparation. This section also covers the resedimentation process, also known and reconstitution, that is used to create specimens at stress levels and with consistent characteristics that allows for a controlled set of experiments without sample variation.

Chapter 4 covers the testing equipment used, which includes bender elements, ultrasonic transducers, accelerometers, and extensometers. Details on how each type of instrumentation works are presented here, as well as limitations and advantages of these different methods, followed by descriptions of the different data acquisition systems used. Finally, a brief introduction to the new testing equipment developed during this research with the intent of significant use in the future completes the end of this chapter.

In order to better understand the behavior of bender elements and all the variables that could profoundly affect the measurements obtained using this technology, Chapter 5 describes parameters that were varied in order to establish the significance of its effect on the results. This includes the frequency, specimen geometry, boundary conditions, and stress level used during the experimentation.

Chapter 6 investigates the data analysis component of bender element testing and refers to the literature for the comparison of results obtained using various data interpretation techniques. A brief explanation on the driving signals for BE testing and ultrasonic transducers is included.

Finally Chapters 7 and 8 present the results of the experimentations conducted at the MIT Geotechnical Laboratory, also comparing them to published results. In addition, different methods of measuring the modulus of materials are used on common materials that have well-established published values as a form of evaluation on the relative magnitude of scatter cause by purely the equipment in an attempt to

better understand the variability present in the testing conducted on soil. Concluding remark are found in Chapter 8, as well as an introduction to the possible future work pertaining to this research.

Chapter 2

Background

2.1 Introduction

The use of wave propagation to describe the small strain behavior of a material has been a well documented, widely-used technique, as evidenced in the literature. There are a number of ways with which to measure the elastic properties of soils, including torsional shear, resonant column, on-specimen strain, and proximity sensors; however, the use of wave propagation has become a prevalent technique due to its relative ease of implementation. While the dynamic testing method of wave propagation has shown to produce results well within the very small strain pre-failure region, the repeatability of results and strain rate effects are still topics of research. There still exist many questions on the interpretation of results produced by wave propagation techniques despite its wide use in industry. Moreover, there have not been proper comparisons between the static and dynamic methods of obtaining stiffness parameters. A description of static and dynamic testing can be seen in Table 2.1. The difference between the two types of testing methods is that dynamic testing occurs at a strain rate high enough to initialize an inertial effect within the specimen, whereas static testing occurs at a much lower repetition rate at which inertial effects are obsolete [Santagata, 1998].

Table 2.1: List of experiments classified as dynamic or static and their stain levels (adapted from [Santagata, 1998])

	Test	Strain (%)
Static	Triaxial (TX)	> 0.05 external, > 0.0001 on specimen
	Torsional Shear (TS) ML (Monotonic)	> 0.0001
	Torsional Shear (TS) CL (Cyclic Loading)	$0.0005 - 0.001$[1]
Dynamic	Resonant Column (RC)	$0.00001 - 0.01$[2]
	Bender Element (BE)	< 0.001
	Ultrasonic Transducer (UT)	$\ll 0.0001$

In the subsequent sections, various methods of obtaining the modulus values of soils will be compared, as well as a more detailed look in particular at bender element technology.

2.2 Velocity Testing

Velocity testing, which includes BE and UT technology, has been gaining popularity as an experimental method due to its relative ease of obtaining the modulus of a material. The bender elements themselves provide a shear wave velocity through the soil (V_s), which can be used with the bulk density of the material (ρ) to calculate the shear modulus G_{max} as follows:

$$G_{max} = \rho \times V_s^2 \tag{2.1}$$

where the subscript "max" signifies the initial stiffness, which is the maximum stiffness measured.

The relationship between the P-wave velocity and the modulus it yields is not as

[1]From [Youn et al., 2008]
[2]From [Nishimura, 2005]

straightforward. Depending on the boundary conditions, one of the following moduli are obtained: elastic, bulk, or constrained. The elastic modulus is the case where a theoretical elastic rod is uniaxially loaded and lateral deformation is permitted. The bulk modulus is in the case of an infinite medium. Finally, the constrained modulus is when an elastic rod is uniformly loaded under uniaxial conditions with no lateral deformations [Johnson, 2011].

When using an ultrasonic P-wave transducer, the P-wave propagates directly down the path orthogonal to the surface of origin. Since the P-wave can be appropriately described as a compressional wave that moves in the vertical direction (without lateral movement), the measured P-wave velocity is used to calculate the constrained modulus:

$$M = \rho \times V_p^2 \tag{2.2}$$

While the constrained modulus is directly calculated from the compressional velocity, the more commonly used modulus to describe the behavior of materials is the bulk modulus (K) [Mondol et al., 2008]. (K) can be calculated using the following relationship:

$$K = M - \frac{4G}{3} \tag{2.3}$$

All the elastic parameters, including the moduli and Poisson's ratio, are related to each other. More extensive derivations can be seen in [Stein and Wysession, 2003] and [Van Der Hilst, 2004], but the final simplified versions can be seen as follows:

$$M = \frac{2G(1-\nu)}{1-2\nu} \tag{2.4}$$

$$G = \frac{E}{2(1+\nu)} \tag{2.5}$$

$$E = \frac{9KG}{3K+G} \tag{2.6}$$

where ν is Poisson's ratio and E is Young's modulus. Although these relations are

useful tools, the abide by the assumption that the material is linearly elastic and isotropic. Although it is clear that the materials tested during this research are not isotropic, the equations are still used.

One of the great advantages of velocity testing is the ability to perform non-destructive testing on specimens. Whereas the torsion shear and triaxial methods of obtaining the shear and bulk modulus of a material require loading increments, from which the behavior of the material dictates the stiffness parameters, velocity testing does not require deformation of the entire specimen. The amount of deformation necessary to obtain interpretable results for each type of testing is represented by the strain values seen in Table 2.1.

One of the overlying questions regarding the different ways of measuring modulus values of soils is whether one method provides the necessary values to accurately assess in situ conditions. Historically, the laboratory-measured stiffness parameters have underestimated the actual values seen in the field; however, this was usually thought to have been caused by sampling disturbance [Santagata, 1998].

As seen in Figure 2-1, [Cho and Finno, 2010] conducted experiments comparing seismic cone penetration test (sCPTs) performed on site with bender element experiments performed on minimally-disturbed specimens from the same location. The indicated bender element velocity is V_{vh}, which means it is a vertically propagating, horizontally polarized wave. The thick line indicates sCPT results within 5m of the location where the samples were taken from to be tested in the laboratory. At the same elevation, the BE velocity results ranged from 180-195 m/s, while the sCPT results varied from 185-225 m/s. This indicates good agreement between field and laboratory results, with the slight difference in range likely caused by sample disturbance. The range of the in situ behavior is slightly higher than the bender element results, which is consistent with the previous observation regarding field versus laboratory measurements stated above.

Another study, performed by [Nishimura, 2005] on London Clay, compared different methods of measuring the stiffness parameters using bender element testing, resonant column, and cross-hole field measurements. The results are shown in Fig-

ure 2-2, where the subscripts hh indicate horizontally propagating, horizontally polarized shear wave velocity values and vh indicates vertically propagating, horizontally polarized shear waves. Ranges for the various testing methods are given, with arrows spanning the range of the measured parameters. It was evident that the field measurements demonstrated the highest stiffness values, followed by resonant column, and then bender element results.

While the discrepancies between field measurements and laboratory measurements have been well-documented and widely accepted, few systematic attempts have been made at establishing a correlation that resolves this misalignment of laboratory stiffness parameters. While there have been a few studies done on rectifying the gap, such as [Gist, 1994] who used the gas pocket model and corrected for local flow to translate ultrasonic velocity measurements to seismic field measurements, attempts to do so with bender element results are scant.

2.3 History of Bender Element Testing

The piezoceramic material used to construct bender elements was initially discovered in the 1940s, but was first used in the application of wave propagation through soils by [Shirley and Hampton, 1978]. Since its first use in the laboratory, bender elements have been incorporated in many functional capacities of already-existing geotechnical experimental setups. Not only have they been used in triaxial cells in multiple directions [Cho and Finno, 2010, Fioravante and Capoferri, 2001, Gajo et al., 1997, Leong et al., 2009], but have also be used in oedometer cells [Yamashita et al., 2004, Zeng and Ni, 1999], resonant column apparatuses [Ferreira et al., 2007, Youn et al., 2008], torsional shear [Youn et al., 2008], and in the field under unconfined conditions [Asaka et al., 2008]. Due to its ability to measure the shear modulus at low stresses, bender elements remain widely used today, despite the difficulties experienced in signal interpretation.

2.4 Applications of Bender Elements

Small strain shear modulus measurements are a vital component in the geotechnical design process. It was observed that most of the ground deformations occurring in the field due to excavations and construction are in the small strain region of $0.001 - 0.5\%$ [Jardine, 1995], thus the pre-failure behavior of soils at small strains is a major area of interest. Strains below 0.001% are in the elastic range, which allows for the assumption of useful tools and relations, such as, for example ray path analyses and equations 2.1 through 2.6. Bender elements have strains below the 0.001% boundary, which makes them a worthwhile tool to characterize the stiffness parameters of a soil.

In addition to the ability of bender elements to greatly enhance soil characterization, they can be used as a method of better understanding velocity measurements observed in soils. It is of great interest to the oil industry to develop a better understanding of the velocity behavior exhibited in soils and rocks as a way of enhancing basin modeling techniques and locating hydrocarbon-rich reservoirs. The interpretations and analysis of sonic logs has become very sophisticated over the past decade; however, there remain some uncertainties regarding the unloading behavior of soils and rocks as well as the anisotropy they exhibit, sometimes making pore pressure prediction techniques inaccurate [Bowers, 1995]. While very stiff soils and shales have been extensively tested with ultrasonic transducers, little research has been conducted on the low-stress regime and the transition from overconsolidated regions to normally consolidated regions with respect to this application. Additionally, the extensive ultrasonic transducer measurements that have been conducted sometimes prove to be inconsistent and arbitrary interpretation techniques are utilized, such as seen in [Yamashita et al., 2004].

2.5 3D Velocity Behavior

The relationship between the stress and strain experienced by a medium can be related through an adaptation of Hooke's law, which originally related force to displacement as follows:

$$F = k * u \tag{2.7}$$

This equation was generalized into a 3 dimensional expression that can be simply stated as the following relation:

$$\sigma_{ij} = c_{ijkl} * \epsilon_{kl} \tag{2.8}$$

where σ is the stress tensor, c is the elastic stiffness tensor, and ϵ is the strain tensor. Since the subscript can range from 1 to 3 due to its 3 dimensional nature, and there are 4 subscripts that define one term, there is a possibility of 81 independent terms; however, for linear elastic material, the following holds true:

$$c_{ijkl} = c_{jikl}$$

$$c_{ijkl} = c_{ijlk}$$

$$c_{ijkl} = c_{klij}$$

This reduces the expression to 21 independent constants, as opposed to the initial 81 independent constants. These 21 independent constants describe an anisotropic medium. Different types of symmetry can reduce this number even further, until isotropy is reached, which consists of only 2 independent constants. In between these two limits, there are many different levels of symmetry that the specimen can exhibit. In the case of the clay specimens tested in this research, the material is taken to be transversely isotropic (also called cross anisotropic). Using Voigt notation, the matrix

form of equation 2.8 can be expresses as follows:

$$\begin{pmatrix} \sigma_1 \\ \sigma_2 \\ \sigma_3 \\ \sigma_4 \\ \sigma_5 \\ \sigma_6 \end{pmatrix} = \begin{pmatrix} C_{11} & C_{12} & C_{13} & C_{14} & C_{15} & C_{16} \\ C_{12} & C_{22} & C_{23} & C_{24} & C_{25} & C_{26} \\ C_{13} & C_{23} & C_{33} & C_{34} & C_{35} & C_{36} \\ C_{14} & C_{24} & C_{34} & C_{44} & C_{45} & C_{46} \\ C_{15} & C_{25} & C_{35} & C_{45} & C_{55} & C_{56} \\ C_{16} & C_{26} & C_{36} & C_{46} & C_{56} & C_{66} \end{pmatrix} \begin{pmatrix} \epsilon_1 \\ \epsilon_2 \\ \epsilon_3 \\ 2\epsilon_4 \\ 2\epsilon_5 \\ 2\epsilon_6 \end{pmatrix} \tag{2.9}$$

where $\sigma_1 = \sigma_{11}$, $\sigma_2 = \sigma_{22}$, and $\sigma_4 = \sigma_{12}$, and $C_{11} = C_{1111}$, etc.

The factor of 2 is present in the strain tensor to account for the difference between the average shear strain and the total engineering shear strain. The average shear strain takes into account the average movement in the x direction relative to y and the y direction relative to x, whereas the engineering strain is the total strain in the x-y plane. γ is the engineering strain, while ϵ is the average strain. γ and ϵ are equal when i=j. Otherwise $\gamma = 2\epsilon$. See Figure 2-3 for a schematic representation.

As previously mentioned, the specimens tested in this research are transversely isotropic, which means they have 5 independent constants. The above stiffness matrix for a transversely isotropic medium can be populated as follows:

$$[C_{ij}] = \begin{pmatrix} M_1 & M_1 - 2G_1 & F & 0 & 0 & 0 \\ M_1 - 2G_1 & M_1 & F & 0 & 0 & 0 \\ F & F & M_2 & 0 & 0 & 0 \\ 0 & 0 & 0 & G_2 & 0 & 0 \\ 0 & 0 & 0 & 0 & G_2 & 0 \\ 0 & 0 & 0 & 0 & 0 & G_1 \end{pmatrix} \tag{2.10}$$

The subscripts represent the directions in which the constrained and shear moduli were obtained. The coordinate system can be seen in Figure 2-4. A, B, and C represent the possible directions to consider for a specimen. Since the specimen is transversely isotropic, the A and B directions are identical and yield the same

results. Hence, there are two directions of interest, which are labeled with subscripts 1 and 2. The horizontal direction is described by 1, while the vertical direction is described as 2. The P and S in the figure represent a P-wave and S-wave. It should be noted that the shear wave can be polarized in two principle directions, which is described by the two S arrows orthogonal to each other. A graphic representation of the possible waves is seen in Figures 2-6 and 2-5. The blue rectangles represent the bender element tip and the red arrows indicate the direction of deflection. When a vertically-propagating shear wave is sent through a transversely isotropic medium, the polarization of the wave is irrelevant, since in both cases the wave travels through the same layering. For a horizontally-propagating wave, however, the shear velocity depends on the polarization of the wave, which determines the layers that it travels through. In the case on the left in Figure 2-5, the S-wave is traveling completely in the layer at which the bender element is placed. The case on the right, the wave is propagating horizontal but has a vertical polarization, in which case the wave travels across multiple layers. This wave yields the same value as a vertically-propagating S-wave [Nihei et al., 2011].

F is the term that takes into account the diagonal direction and is expressed by the following terms:

$$F = -C_{44} + \sqrt{4\rho^2 V_{pT}^4 - 2\rho V_{pT}^2 (C_{11} + C_{33} + 2C_{44}) + (C_{11} + C_{44})(C_{33} + C_{44})} \quad (2.11)$$

V_{pT} is the P-wave velocity in the 45° diagonal direction that links the vertical to the horizontal directions. When measuring the off-axis velocity, the difference between the group velocity and phase velocity arrises. There has been some debate over how the velocity data should be interpreted [Dellinger and Vernik, 1994]. One widely accepted method was formulated by Dewhurst et al. as follows [Dewhurst and Siggins, 2006, Kuila et al., 2011, Sarout and Gueguen, 2008]. In a transversely isotropic medium, waves traveling in any direction is considered to be a group velocity, with the exception of the principle axes where the group velocity is equal to the phase velocity. Since the phase velocity is needed to complete the stiffness matrix, the P wave traveling

at a 45° angle needs to be converted from a group to a phase velocity by solving the relationship between phase and group velocities and the Christoffel equation. The V_{pT} term needs to be the phase velocity measurements in order to obtain the correct stiffness matrix.

2.6 Methods of Obtaining the Shear Modulus

There are many methods of obtaining the shear modulus of a soil, with the four most common being resonant column, torsional shear, triaxial deformation measurements, and bender elements. The stiffness values obtained from each method are not consistent from one method to another, which can be attributed to the strain levels associated with the type of experiment. A schematic seen in Figure 2-7, which approximately describes the expected behavior of the experimental results based on strain values. As seen in the figure, at very low strain levels, the stiffness values are very high and constant, in section (a). During section (b), the stiffness begins to decrease in a non-linear manner, which is where most of the variability in the results originates. Finally in part (c), the soil exhibits a slow decrease in stiffness with large strain levels, which is where plastic deformation occurs.

2.6.1 Resonant Column

Resonant column tests are based on the vibration of a wave through the soil specimen caused by an excitation force. The excitation force is produced by a coil and magnet system that generates an electromagnetic force that moves the top plate appropriately. Based on the measurements of resonant frequency of the specimen, as well as the specimen geometry, amplitude of vibration, and the characteristics of the driving vibration, the calculation of the shear modulus and shear velocity through the system is performed [Isenhower et al., 1987]. Although the resonant column is a well-respected testing method that has shown to yield consistent results since its first introduction in 1963 by Hardin and Drenevich, there are some limitations attributed to this experimentation technique. One shortcoming of the RC test is the inability to

control the frequency at which the experiment is conducted since it is a function of the soil being tested. Additionally, transitioning from one stress level to another due to consolidation can make the RC technique more problematic than other methods, as far as equipment setup is concerned. In addition, the excitation power needs to be continuously adjusted. This can introduce some scatter in the results. The RC test can also only be conducted in one direction at a time, thus lacking the multi-directional capabilities that bender elements possess. Another concerning factor is the occasional utilization of cement paste to cement the specimen to the endcaps, in order to prevent bedding errors. This can cause some end-boundary effects and non-uniform stress distributions [Kim and Stokoe, 1992]. Finally, to obtain measurements, even with an experienced technician, at least 500 cycles of loading are required before measurements can be taken [Isenhower et al., 1987]. Although the RC tests are conducted under the assumption of a visco-elastic constitutive model, the other methods also make similar assumptions.

2.6.2 Torsional Shear

The torsional shear method of obtaining the shear modulus is based on the principle that applying a torque to a cylindrical specimen will yield a reaction equivalent to the shear modulus of the specimen. Usually the TS experimentation is conducted in a triaxial setup, with the ability to control the stress level at which testing is done. Usually the amount of torque applied is non-destructive, thus multiple measurements can be taken. The shear modulus is calculated by the simple relation below:

$$G = \frac{T}{\theta} \times \frac{L}{J} \tag{2.12}$$

where T is the applied torque, θ is the angle of rotation, L is the length of the specimen, and J is the polar moment of inertia of the specimen. One of the disadvantages of torsional shear tests is that the amount of strain experienced in the specimen varies as a function of the distance from the center of the specimen, thus causing a non-uniform strain distribution. Another shortcoming is that, once again, only a

single-directional shear modulus can be obtained and each data point requires one specimen.

2.6.3 Triaxial Apparatus

Deformations monitored in triaxial specimens have been a useful tool in the measurement of the Young's modulus while obtaining other parameters such as undrained shear strength and friction angle values. The hardship faced with this method of obtaining stiffness parameters of soil is the need to mount on-specimen measurement devices that can monitor the deformations occurring without incurring deformations themselves. Some methods used to perform such measurements include high-resolution miniature LVDT's (Linear variable differential transformers), proximity sensors, and local deformation transducers [Santagata, 1998]. Developing on-specimen measurement techniques is vital in order to remain in the small strain measurement region since off-specimen forms of measurements cannot reach nearly as high of a resolution of less than 0.05% strain. A study performed by [Santagata, 1998] established an on-specimen yolk system fitted with LVDT's that was able to measure the Young's modulus of the specimen for strains of 0.0001% or greater. This remains in the region of small strain measurements, which is below 0.01% strain. It was found, however, that the linear region characterized by section (b) in Figure 2-7 only requires strain levels below 0.05%.

2.6.4 Bender Elements

Bender elements have many resounding benefits that make them a desirable technology to use of material property testing of soils. They are a non-destructive way of dynamic testing on soils and can measure the stiffness parameter at a specific stress level without having to actively apply stresses or deform the specimen in order to perform the measurement. The frequency at which the bender element is driven can be changed to better accommodate the material being tested and to obtain the clearest signal possible. It has multi-directional capabilities and can be integrated in

many setups including triaxial, RC, TS, or simply in the field without any constraining conditions. The strain levels incurred on the specimen are very small relative to TX and TS methods and remain entirely in the elastic region, as is calculated in section 4.2.2. Overall, bender elements are a relatively economical alternative to the instrumentation listed above.

2.7 Comparing Different Methods

One of the greatest uncertainties regarding stiffness parameter testing is the scatter attributed to the data and the misalignment of results obtain from different methods. One commonly believed explanation regarding the differences in results based on the technology used is the strain level effect. If more strain is imparted during the testing procedure, this incurs a softer response, hence yielding lower modulus values. Based on this principle, bender elements would have the highest stiffness values, while deformations measured with LVDT's in the triaxial apparatus would have the lowest modulus measurements.

While not explicitly addressed in this thesis, the strain rate also has an influencing factor on the measurement results for various instrumentation. For example, the strain rate exhibited in the triaxial apparatus is usually around $0.5\%/hr$, torsional shear as around $0.1-10\%/hr$ [Santagata, 1998]), while dynamic testing is at least over an order of magnitude larger. These rates are not absolutely correct calculations since they vary so widely, but they do give approximate values and ranges. The resonant column strain rate is between $10^2 - 10^5\%/hr$ and bender elements can have a strain rate of approximately $2.5 \times 10^6\%/hr$, as calculated in section 4.2.2. There is debate over how much of an effect strain rate has on the shear modulus results and whether a higher strain rate decreases the stiffness, thus creating a softer measurement. Rate sensitivity is a topic that needs further investigation.

In order to further investigate the differences observed between testing methods, a review of a few publications will be presented in an attempt to establish a consistent trend in stiffness results according to testing methods.

The first study is an inter-laboratory study by [Yamashita et al., 2004] conducted in 11 countries by 23 institutions willing to follow a strict set of guidelines for making specimens and performing experiments using both bender elements and some alternatives including TX, RC, and TS. Toyoura sand was prepared using the air-pluviation technique to achieve a relative density of 50% and 80%. One of the key observations of this study was that when all the raw data provided by the different institutions was re-evaluated by one person, the scatter in the data set reduced significantly, which is evidence of the user-bias present in the signal interpretation of the results.

The G_{max} obtained from bender elements was compared with the G_{max} obtained from accelerometers, P-waves, TS, TX, and RC. The accelerometer measurements were performed using bender elements with the accelerometers reading the signals that the BE's sent. The 'P-wave' method is using a bender element to send a P-wave signal, which is used to back-calculate the shear modulus assuming a Poisson's ratio of $\mu = 0.5$. While the $K = 0.5$ condition is of more interest for the research pertaining to this thesis since all the past and future experimentation is using K_0 conditions, the $K = 1$ condition is presented initially for comparison. As can be seen for a dry specimen at $K = 1$ conditions in Figure 2-8, there is very little difference in the results, with triaxial generally yielding shear modulus values lower than BE, while the accelerometer and P-wave methods have generally higher stiffness values, and finally RC and TS have very similar results compared to BE. The higher values obtained using the accelerometer and P-wave methods could be attributed to the assumption of a Poisson's ratio since they were both back-calculated. Observing the $K = 0.5$ case for a dry specimen, it is evident that there is much more scatter than for the $K = 1$ case, and this is likely due to the process of load application, since maintaining $K = 0.5$ is technically more difficult than $K = 1$, which can lead to some minor errors in stress levels. Putting this aside, the values seen in Figure 2-9 can still give an approximate idea about the trend of results. The $K = 0.5$ conditions showed the P-wave and accelerometer results once again yielding higher G_{max} values than the BE's. The triaxial was still generally lower in stiffness parameters than the BE, although with slightly more variability than in Figure 2-8. The resonant column was almost

identical to the bender element results. The saturated specimens exhibited somewhat different results. As can be seen in Figures 2-10 and 2-11, the bender elements tended to exhibit larger shear modulus values than both the TS and RC values. Finally, a compilation of the different methods under saturated conditions for Toyoura sand is shown as a function of void ratio in Figure 2-12, which was conducted during the previous iteration of the parallel testing committee. The results showed relatively good agreement between BE, RC, and TS tests with no distinctive trend. The largest observable difference was found in the undrained triaxial testing techniques, which were consistently 15% lower than the other methods. Since little detail was provided regarding the precise triaxial apparatus implementation, it is not conclusive whether the lower values were caused by bedding errors, due to the higher strain level, or a combination of the two.

A study conducted by [Ferreira et al., 2007] performed simultaneous measurements of the shear modulus of Porto residual soil using resonant column and bender element methods. The results were plotted as a function of mean effective stress (as seen in Figure 2-13), with best fit lines indicating the trend of the results. The (TD) and (FD) indicate the method used to analyze the bender element signals and are addressed in Chapter 6. The resonant column results were shown to produce consistently higher values of the shear modulus as compared to the bender element results.

Another study performed by [Youn et al., 2008] performed torsional shear and resonant column tests on Toyoura sand, both of which were retrofitted to contain bender elements. A series of experiments were conducted for multiple void ratios as well as dry versus saturated conditions. The results can be seen in Figures 2-14 and 2-15. The bender element velocity results were selected according to the peak-to-peak method. For dry conditions, the bender element results were shown to yield higher shear modulus results, followed by resonant column then torsional shear. At a lower void ratio, the differences are amplified, whereas for a higher void ratio, the differences are minimal. Void ratio e is calculated as the volume of voids divided by the volume of soil grains. This supports the fact that the results diverge more at higher densities, which could be a result of the grain contact engagement and the

respective mechanisms exhibited in the respective methods. For saturated conditions, these differences are not as pronounced, which would imply that the saturation effect seen with the bender elements is more pronounced than for RC or TS. This could be attributed to weak fluid flow effects due to the frequency range utilized (11kHz).

As a final form of comparison, it is warranted to look at both RC and TS relative to each other, and observe whether there is a saturation effect such as seen in Figures 2-14 and 2-15. A study performed by [Iwasaki et al., 1978] compared TS and RC at various strain levels. The results seen in Figure 2-16 show an experiment conducted on dry and saturated Toyoura sand at a mean principle stress of $p = 1ksc$. The y-axis is normalized to the the value of G at 0.01%. It can be observed that there is a slight trend of higher shear modulus values for dry specimens under RC testing. For TS, there was essentially no observable trend. In Figure 2-17, the shear modulus is seen as a function of void ratio at $p = 1ksc$, with the RC tests once again showing marginally higher values for dry specimens, while no observable trend for TS is seen. Since the void ratio used in these experiments is approximately $e = 0.7$, it can be compared to the study conducted by [Youn et al., 2008]. While [Youn et al., 2008] does show the same trend of decreasing shear modulus for saturated specimens, a much larger difference is seen, as opposed to [Iwasaki et al., 1978]. Additionally, no difference in the shear modulus obtained from the TS is seen in the study conducted by [Iwasaki et al., 1978], whereas [Youn et al., 2008] shows a significant decrease in TS results with saturated specimens.

After considering all the publications described above, the results were somewhat inconclusive. Although the RC generally produced either the same shear modulus or higher than the bender element [Nishimura, 2005, Ferreira et al., 2007, Yamashita et al., 2004], the study conducted by [Youn et al., 2008] showed higher values for BE as opposed to RC for dry samples of Toyoura sand. The TS results were very similar to RC, with [Youn et al., 2008] showing slightly lower values for TS as compared to RC and BE for dry sand. Finally, the results obtained via TX were usually lower than those obtained by BE [Yamashita et al., 2004]. The lower value for TX can be most readily explained through the strain softening effect; however, the strain rate

Table 2.2: Summary of shear modulus values exhibited by the respective instrumentation from various publications

Source	Hierarchy of G_{max} values
[Yamashita et al., 2004]	RC = TS = BE > TX
[Nishimura, 2005]	RC > BE
[Ferreira et al., 2007]	RC > BE
[Youn et al., 2008]	Dry: BE > RC > TS Saturated: BE = RC = TS

sensitivity could reduce this discrepancy. Table 2.2 summarizes the trends observed.

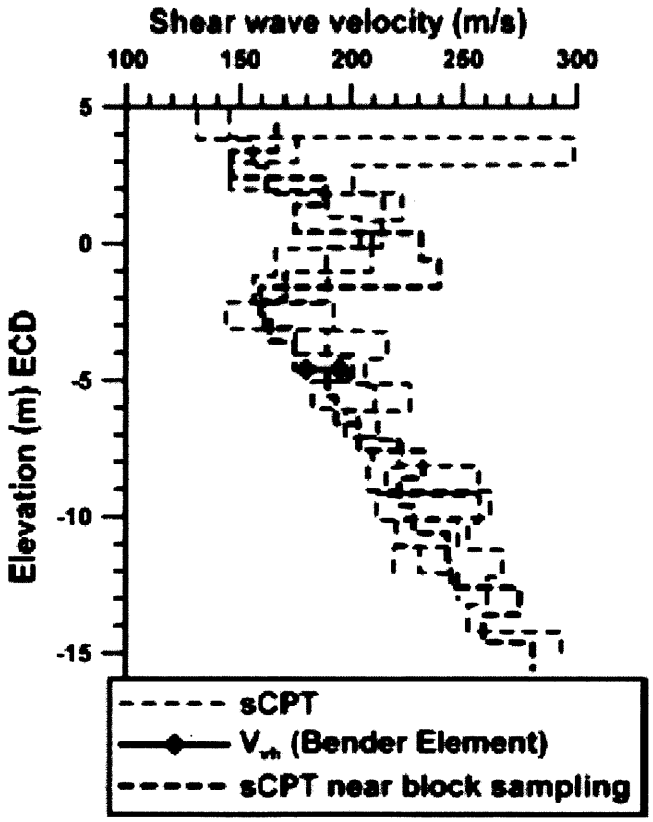

Figure 2-1: Comparing bender element results to field results obtained using seismic cone penetration tests (sCPT), both in the general site where samples for BE testing occurred as well as specifically within 5m of the sampling areas [Cho and Finno, 2010]

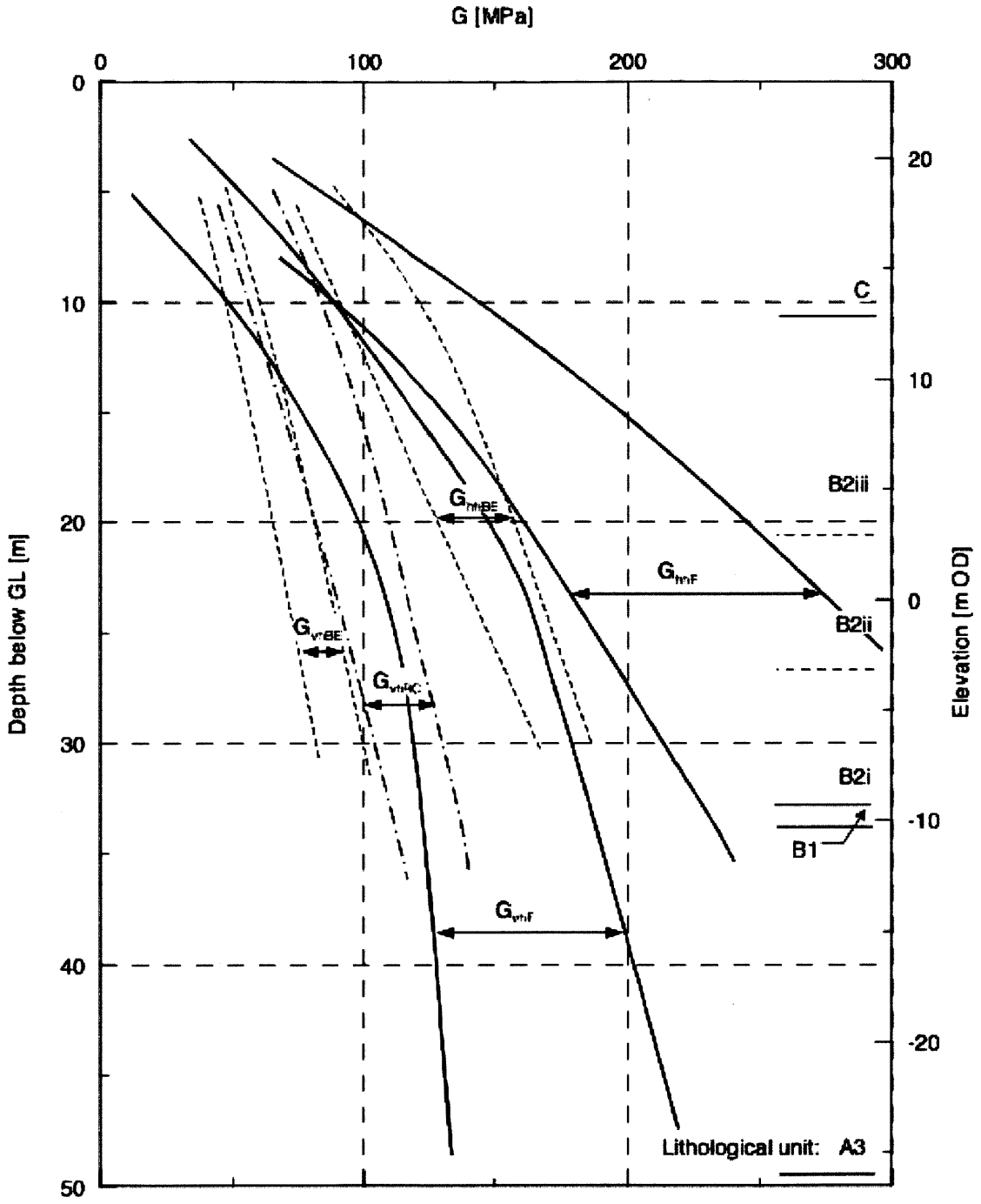

Figure 2-2: A study on London Clay conducted by [Nishimura, 2005] observed the values of shear modulus depending on testing method. As observed in this figure, in order of highest stiffness to lowest is field measurements, resonant column, then bender elements

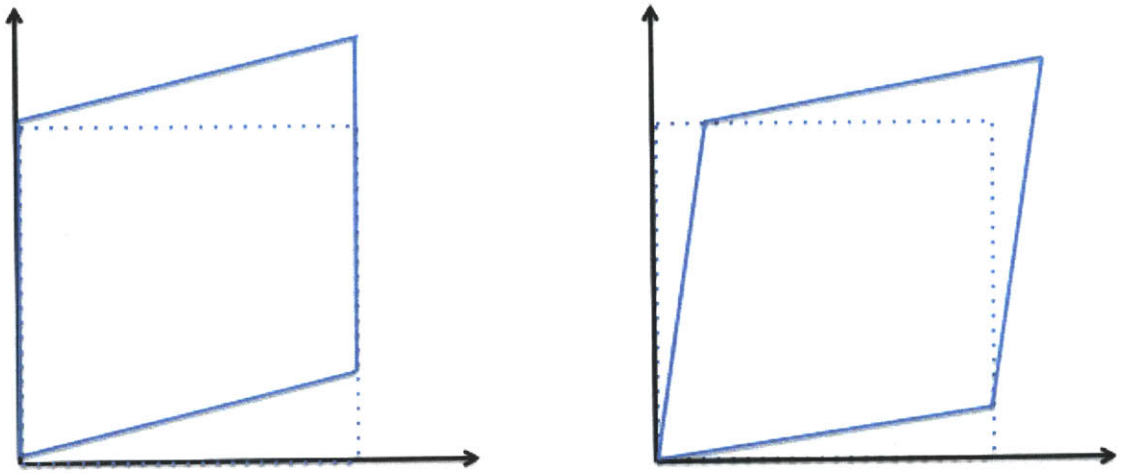

Figure 2-3: The total engineering strain is twice as much as the average shear strain since the average shear strain takes the displacements in both directions and averages rather than adds them up

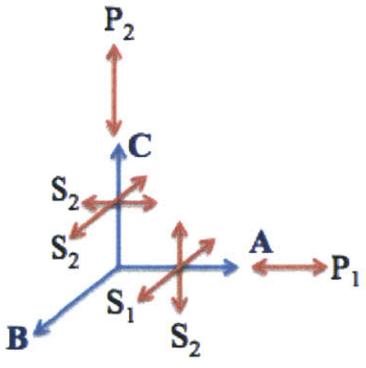

Figure 2-4: The naming convention for propagating waves in various directions is depicted here. The S and P-waves have two possible values for a transversely isotropic medium

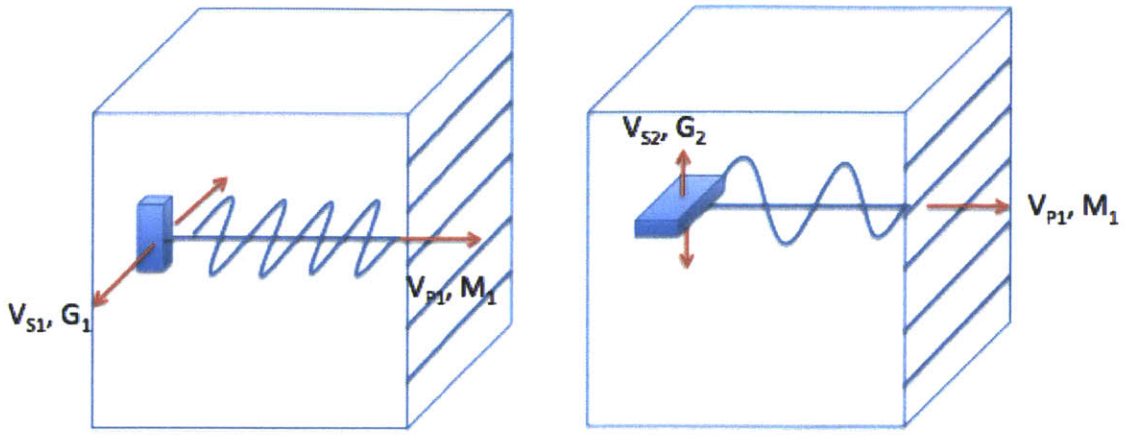

Figure 2-5: Horizontal propagation through cross-anisotropic medium. The subscripts correspond to the matrix seen in section 2.5

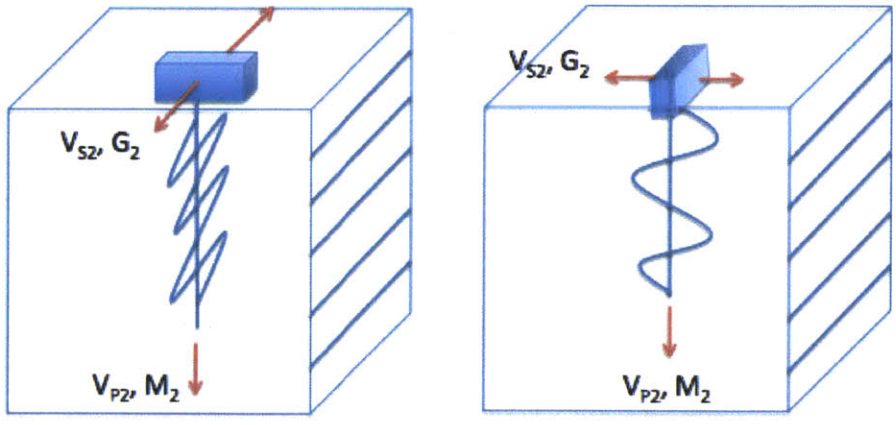

Figure 2-6: Vertical propagation through cross-anisotropic medium. The subscripts correspond to the matrix seen in section 2.5

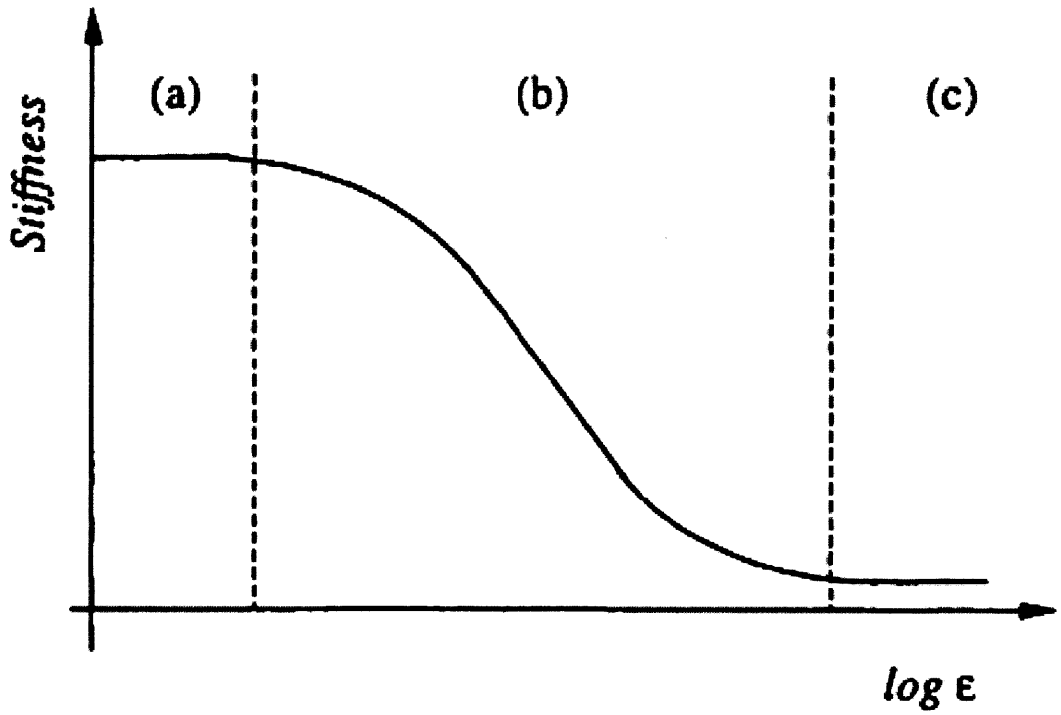

Figure 2-7: Depending on the amount of stiffness exhibited during testing, the modulus value vary as seen in the schematic above. Region (a) is the lowest strain range with constant stiffness, (b) indicates the onset of non-linear behavior, and (c) is the slow decrease of stiffness [Santagata, 1998]

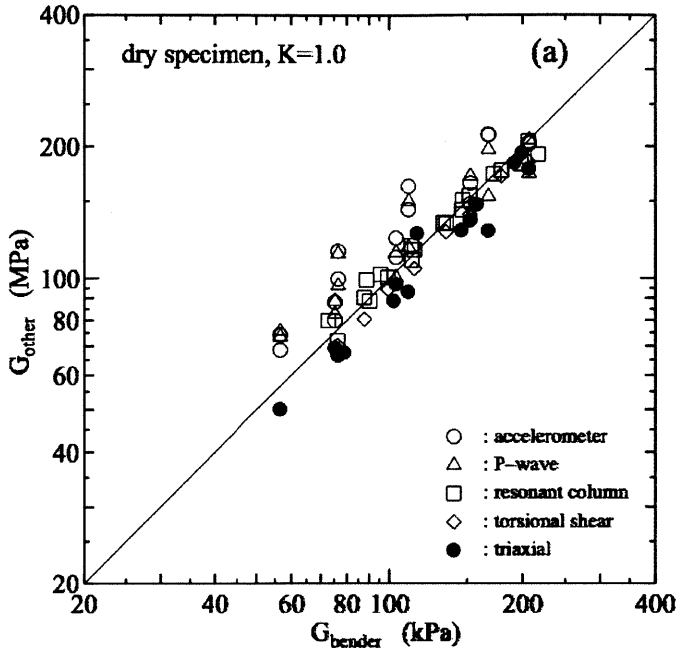

Figure 2-8: From the parallel testing results, bender element measurements were compared to accelerometer, P-wave, TX, TS, and RC for dry specimen under K=1 conditions [Yamashita et al., 2004]

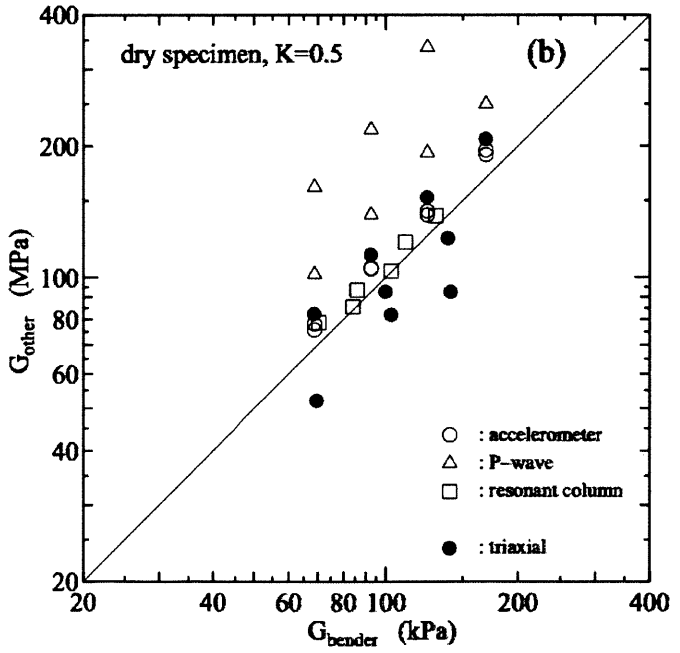

Figure 2-9: From the parallel testing results, bender element measurements were compared to accelerometer, P-wave, TX and RC for dry specimen under K=0.5 conditions [Yamashita et al., 2004]

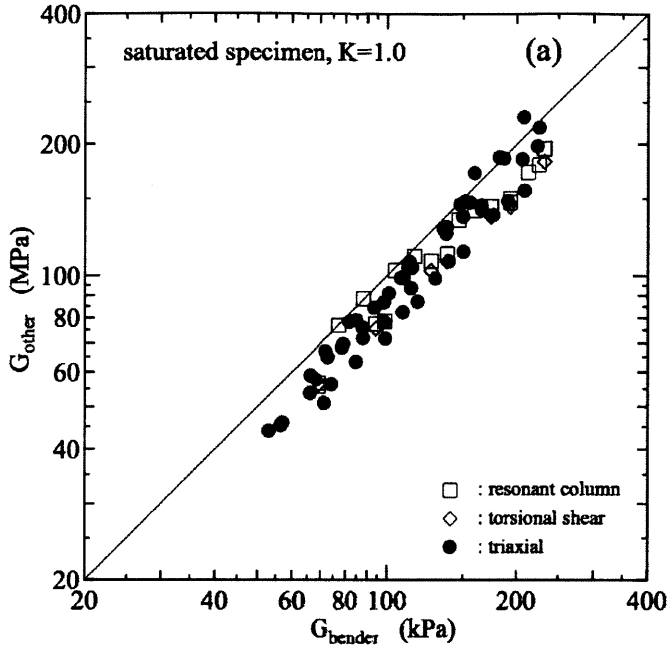

Figure 2-10: From the parallel testing results, bender element measurements were compared to TX and RC for saturated specimen under K=1 conditions [Yamashita et al., 2004]

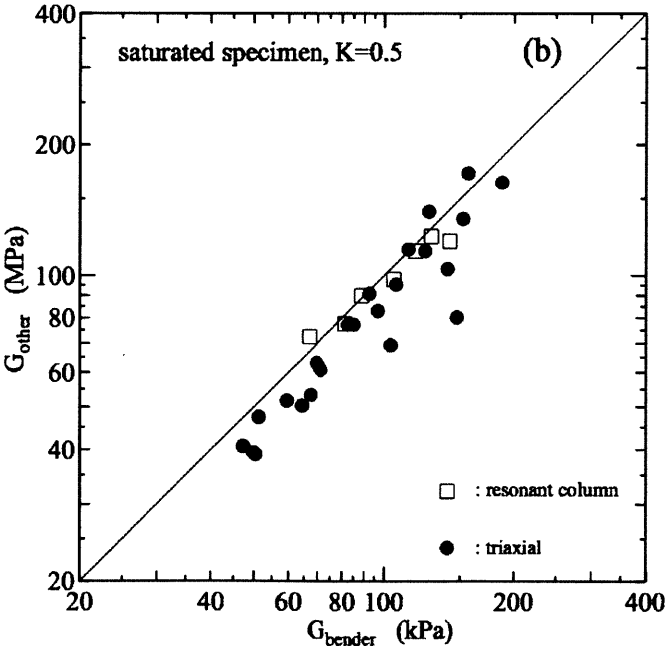

Figure 2-11: From the parallel testing results, bender element measurements were compared to TX, TS, and RC for saturated specimen under K=0.5 conditions [Yamashita et al., 2004]

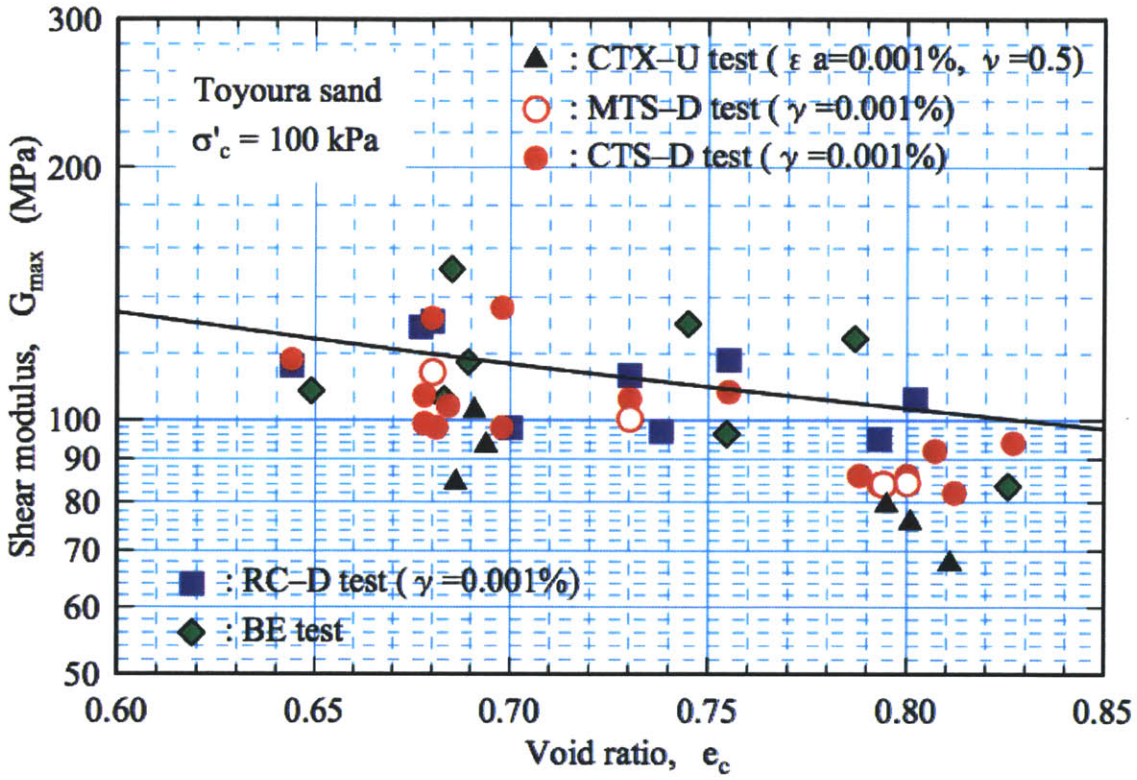

Figure 2-12: From the parallel testing results, bender element measurements were compared to TX, TS, and RC for saturated specimen [Yamashita et al., 2004]

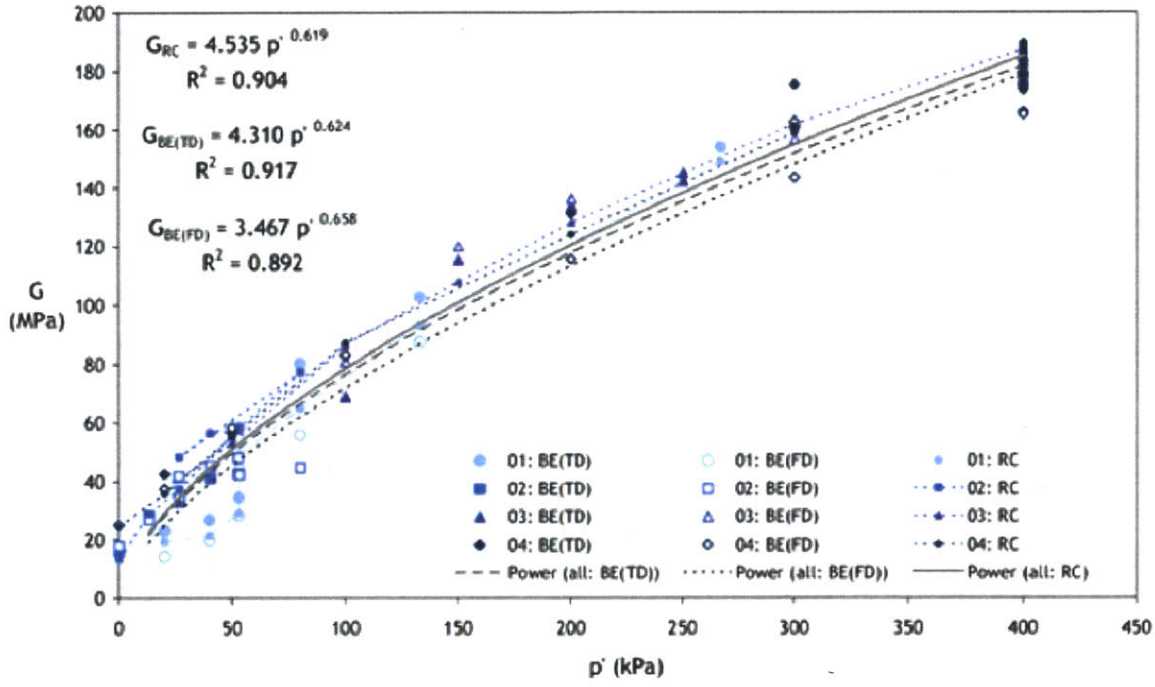

Figure 2-13: Resonant column and bender element measurements were performed on the same Porto soil specimens in a single apparatus. Results indicate good agreement between the two methods. Both frequency domain (FD) and time domain (TD) methods are shown in the results as a function of mean effective stress [Ferreira et al., 2007]

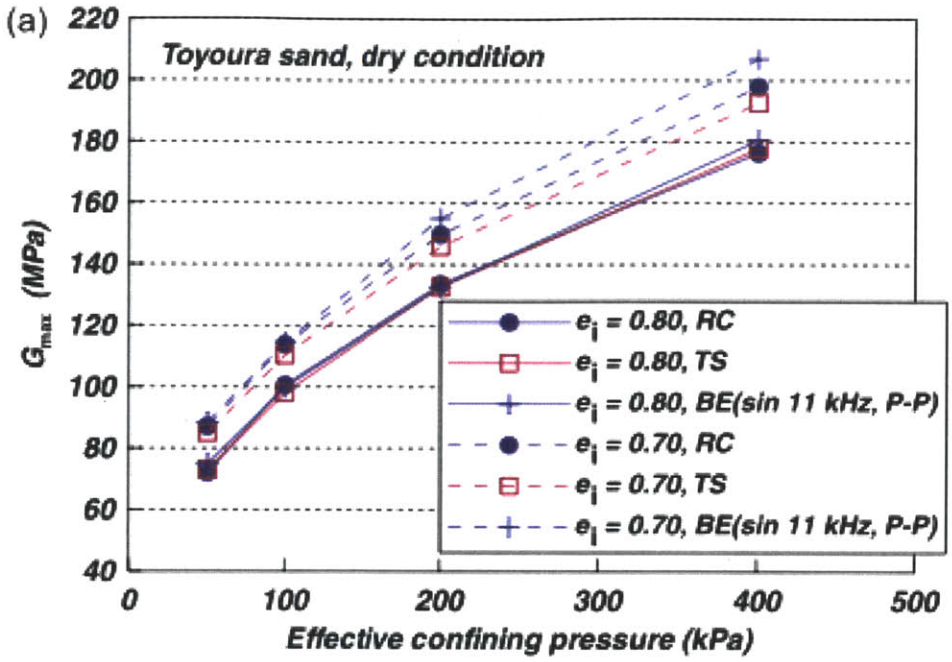

Figure 2-14: Resonant column and torsion shear experiments with added bender elements in the setups were conducted on Toyoura sand under dry conditions [Youn et al., 2008]

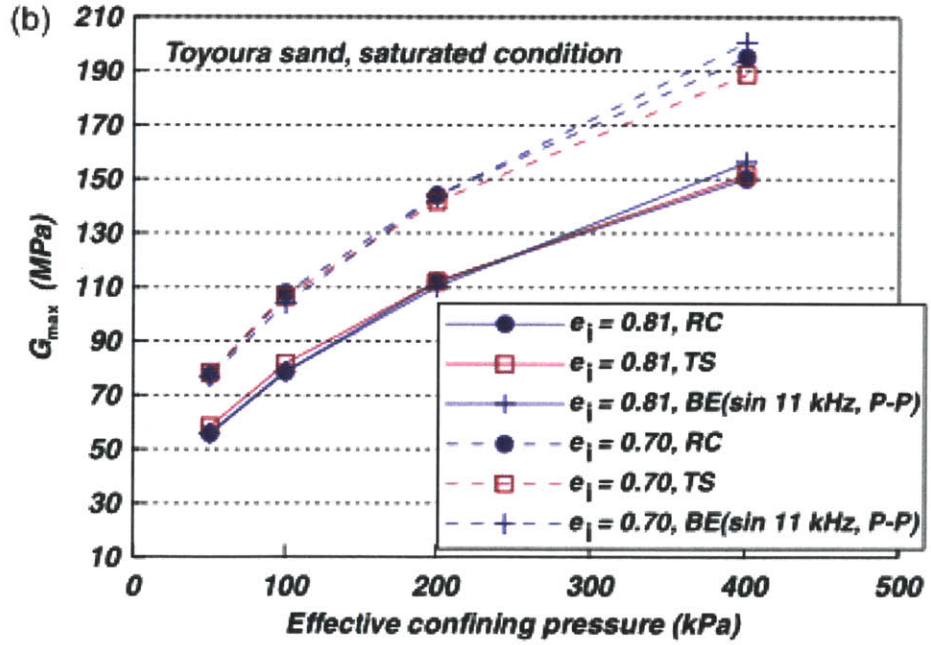

Figure 2-15: Resonant column and torsion shear experiments with added bender elements in the setups were conducted on Toyoura sand under wet conditions [Youn et al., 2008]

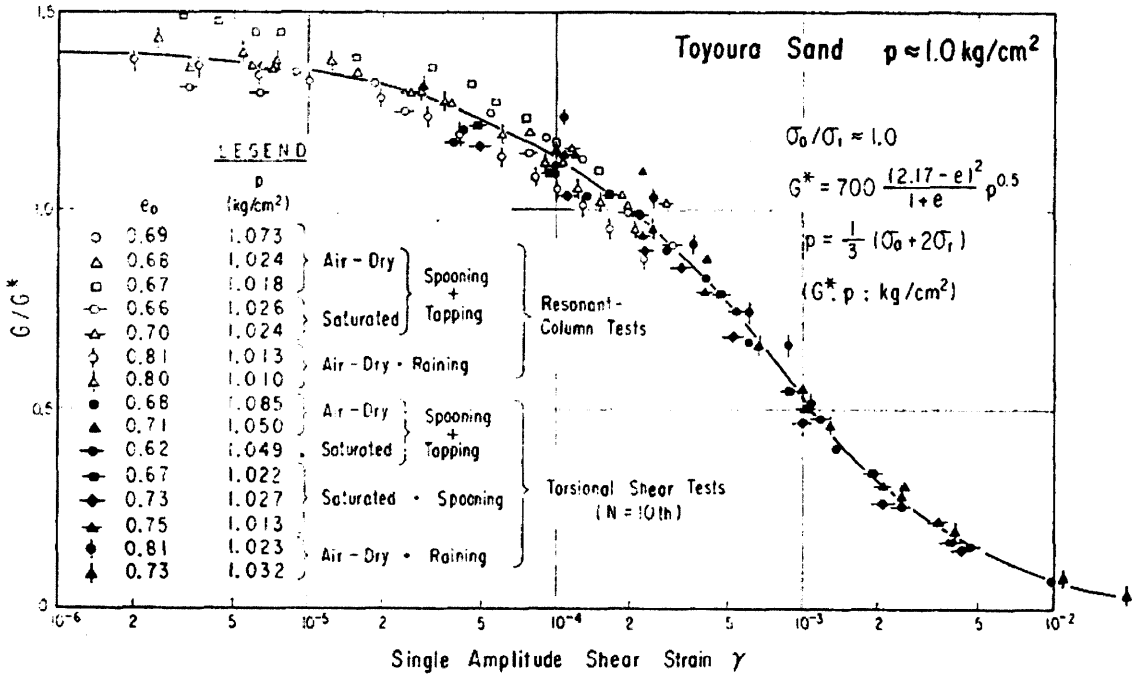

Figure 2-16: A comparison of RC and TS tests conducted at a confining pressure $p = 1ksc$ on saturated and dry specimens of Toyoura sand as a function of strain level. The y-axis is normalized to the the value of G at 0.01% strain [Iwasaki et al., 1978]

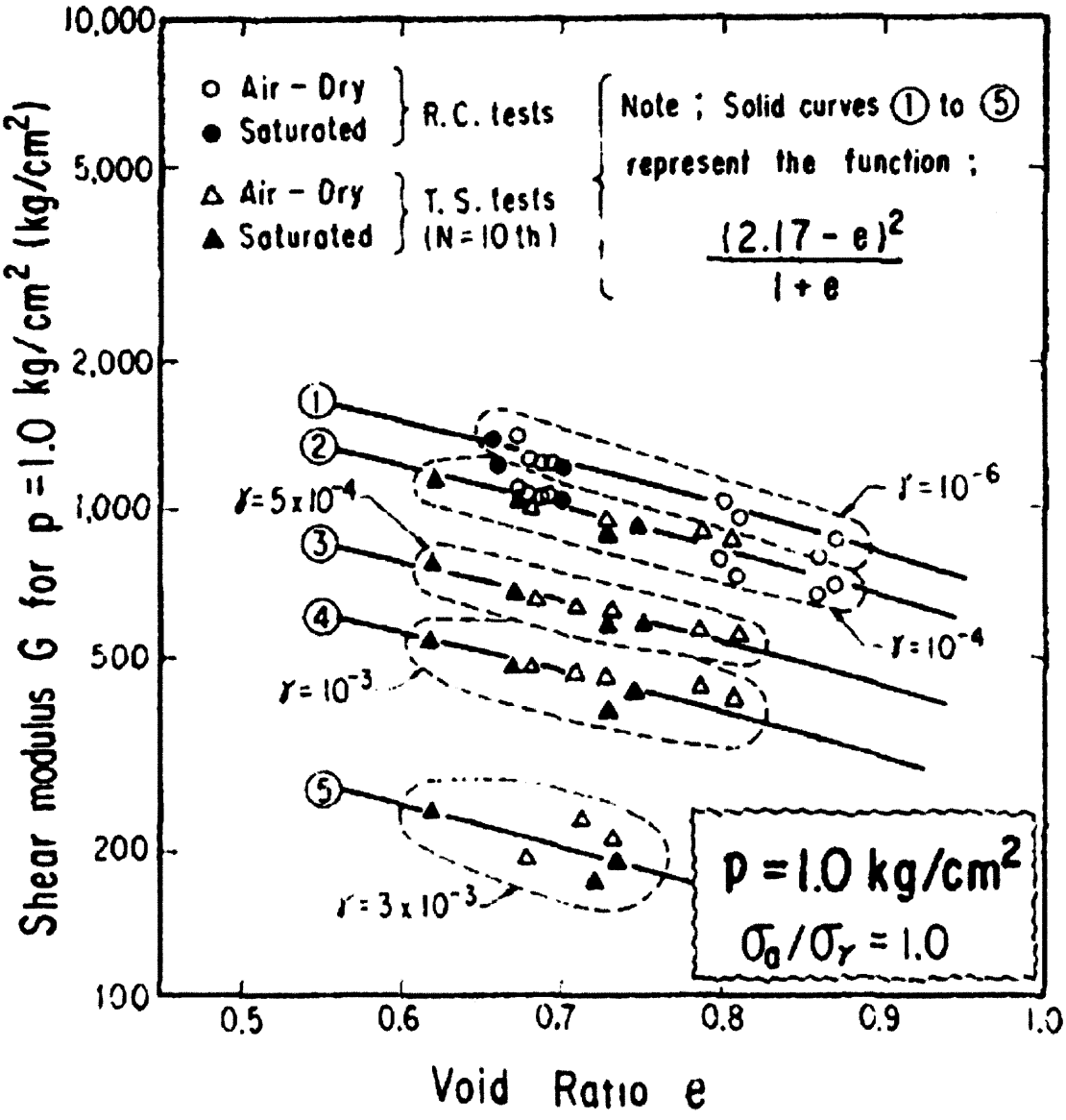

Figure 2-17: A comparison of RC and TS tests conducted on saturated and dry specimens of Toyoura sand as a function of void ratio. The y-axis is the shear modulus G at mean principle stress of $p = 1ksc$ [Iwasaki et al., 1978]

Chapter 3

Materials and Specimen Preparation

3.1 Materials

Two primary materials were used in the study of velocity testing using bender elements. The first half of the research was performed on Ticino sand, while the second half was conducted on Boston Blue Clay (BBC). Dry sand was initially used due to its greater ease of preparation, since the first portion of the experimentation was focused on observing the behavior of the bender elements and how they transmit signals through soft mediums. Once the results obtained from testing by sand were sufficiently understood and provided consistent results, wet clay was used. Although the clay introduced many more complications, the results are more pertinent to extensions of in situ behavior.

3.2 Ticino Sand

The beginning portion of the experimental progress was conducted on Ticino sand. Sand was used due to its ease of specimen setup, and Ticino sand was in particular chosen since it is a well-tested sand with published results for various parameters. The initial experimentation was focused on establishing the behavior of the BEs, hence,

Table 3.1: Range of test setup parameters for Ticino sand

Unit	Range
Porosity, $n()$	0.33 - 0.45
Density, $\rho(g/cm^3)$	1.4 - 1.6
Void ratio, $e()$	0.6 - 0.85

Table 3.2: Material properties of Ticino Sand [Fioravante and Capoferri, 2001]

Property	Specific gravity:	$G_S = 2.681$
	Mean particle size:	$D_{50} = 0.55$ mm
	Uniformity coefficient:	$C_U = 1.6$
	$\gamma_{min} = 13.65kN/m^3$	$e_{max} = 0.927$
	$\gamma_{max} = 16.67kN/m^3$	$e_{min} = 0.578$
Description	Uniform coarse to medium sand	
Morphology	Angular (20%), Sub-angular (55%), Sub-rounded (25%)	
Mineralogy	Quartz (30%), Feldspar (30%), Mica (5%), Opaque (35%)	

beyond comparison between the sequence of experiments and other published results, no care was taken to perform extensive testing on Ticino sand at different loading conditions. For a description of material properties of Ticino sand, see Tables 3.1 and 3.2.

3.2.1 Procedures and Experimental Setup

First the bottom bender element endcap is placed on the loading surface. A 3-inch diameter brass tube is placed onto the lip of the endcap, which constrains any sand from spilling out of the setup. The sand is poured into the brass tube in three separate layers, of approximately the same quantity. After each layer is poured, the rodding method is used, during which a long slender rod is forced through the layer, in a circular motion around the specimen to ensure uniform distribution of sand. Regard Figure 3-1 for the setup of this part of the experimentation. When complete, the top endcap is simply placed on the surface of the sand, slightly pushing the bender element in to ensure full contact around the tip. When the bender element endcaps

(seen in Figure 3-12) are safely positioned on either side of the specimen, it can be put under a load frame, such as the Terzaghi load frame pictured in Figure 3-13. During the incremental loading process, S-wave measurements were taken immediately after load application, usually within a minute. The aim was to obtain data before any potential secondary compression could occur.

3.3 Boston Blue Clay

Boston Blue Clay (BBC) is an illitic glacio-marine clay with a low plasticity. The behavior of BBC has been extensively tested and documented by many researchers, including those listed in Figure 3-3. It is a very testable material (low consolidation time, low swelling behavior, etc.) that does not exhibit extreme behavior in any parameter, thus making it a good representative clay. The experiments of this research were conducted on both intact BBC and resedimented BBC (RBBC). The intact BBC was extracted from the courtyard outside of Killian Court at MIT into approximately 3-inch diameter metal boring tubes. The specimens tested were from Bore No. B10-TP2B, Sample No. S1, from depths of 47-49 feet below ground surface.

The powder clay used to make RBBC is from batch Series IV BBC powder. The series number represents the location of the source material. Thus far, testing at MIT has been conducted on Series I-IV material, as listed in Figure 3-3. The exact origin of Series I and II was not precisely recorded; however, Series III was known to originate from an excavation site near Kendall Square (during the construction of a parking garage) from a depth of 23m [Casey, 2011]. Series IV BBC was obtained from an excavation site at MIT's Koch Biology Building (Building 68) in 1992.

The intact material was processed before it could be used to create reconstituted samples. The processing steps comprised of the following:

1. Add tap water to wet material to create thick slurry;

2. Sieve the slurry through a #10 standard US sieve to remove detritus, which includes any shells, twigs, rocks, etc.;

3. Oven dry at 60° C;

4. Grind the clay to meet a specification of 95% passing a #100 standard U.S. sieve. For Series IV this was performed by the Sturtevant Company using a roller mill.

After the material was processed as prescribed above, it was mixed in a manner to ensure homogeneity and stored in 40-gallon containers [Cauble, 1996]. While the above method was used for the Series IV batch, there are many different alternatives to the process, which include breaking the pieces of wet clay and picking the detritus out by hand or other such methods. A temperature of 60°C was chosen to prevent any intrinsic changes to the properties of the soil. The produced powder form of clay was used for the resedimentation process, which will be discussed in further detail in section 3.3.2.

As previously mentioned, BBC has been extensively tested. It is a low plasticity clay, which is a (CL) designation based on the Unified Soil Classification System (USCS). Some additional index properties for Series IV are listed in Figure 3-4, including the specific gravity, Atterberg limits, and plasticity index values. Atterberg limits were obtained using the rolling method for the plastic limit and the Casagrande cup for the liquid limit, yielding a plastic limit of $w_P = 23.5 \pm 1.1\%$ and a liquid limit of $w_L = 46.5 \pm 0.9\%$. The plasticity index was calculated to be $I_P = 22.7 \pm 1.2\%$ [Abdulhadi, 2009]. The specific gravity G_s was found based on the specific gravity procedures in ASTM D854 using a calibrated iodine flask, providing a $G_s = 2.72 \pm 0.07$. The Grain Size Distribution (GSD) tests performed on the processed Series IV BBC powder using the hydrometer test, as seen in Figure 3-5, indicate that 98% of the BBC powder passed sieve #200. The #200 sieve indicates the upper bound for the fines section of the grain size spectrum; therefore, the majority of the grains in the BBC clay powder are less than 0.075mm in diameter [Germaine and Germaine, 2009].

3.3.1 Sample Preparation

The majority of the specimens tested in this research were fabricated in the laboratory (both the sand and clay). The advantages of making the specimens in the laboratory are extensive. It allows the experiment to focus on the material properties or experimental equipment in a controlled manner rather than allowing the sampling and transportation of the specimen to have a dominating effect. In addition to being aware of any damage or potentially anomalous features of the specimen incurred during the production, one can control the characteristics of the specimen itself. By varying the components used to create the specimen, one can test the exact effects that each component has on the soil behavior. Although this research does not exploit the latter benefit, there is much future potential for velocity testing in this regime, since the majority of velocity testing, as described in Chapter 2, has been conducted on intact specimens.

3.3.2 Resedimentation

Following its initial introduction in 1961 by Bailey at the MIT Geotechnical Laboratory [Abdulhadi, 2009], the process of resedimentation has been extensively used and adapted to optimize the procedures. The governing idea is to create a cross-anisotropic (to be discussed further in section 7.3.1), K_0 consolidated specimen. The resedimentation process involves incrementally loading a slurry until it reaches a prescribed stress level. The stages are described in the following section.

3.3.3 Stages of Resedimentation

The three main steps involved in resedimentation after the clay powder is processed are the following: mixing stage, loading stage, and extrusion stage.

The first step is creating a uniform slurry using the processed clay powder described in section 3.3. The slurry consists of distilled water, sea salt, and clay powder. For this research the slurry was mixed to 100% water content, meaning equal parts of water and dry powder by mass. The salt concentration was set at 16g/L.

Since the natural salt concentrations of BBC range from 4 to 32 g/L depending on the deposit and depth, having a mid-range salinity prevents excessive changes to the pore chemistry of the soil, which can alter the material properties of the specimen as observed in [Horan, 2012]. The value of 16g/L was also used since it is the historical batching value for the last few decades at MIT, and continuing to use this value allows for comparison of current results to previous results. Additionally, the increased salt concentration has not shown significant differences between the in situ tube BBC and RBBC, as has been verified by many [Adams, 2011, Casey, 2011, Horan, 2012], including results seen in Chapter 7.

The components seen in Figure 3-6 were mixed together to create the slurry. First, the salt was dissolved in the water. Then, clay powder was incrementally added to the water solution, taking care not to agitate the powder and cause loss of fines. The components were mixed together using a KitchenAid mixer with a flat beater attachment for a duration of about 30 minutes, which was long enough to ensure thorough blending of the clay and sufficient time to allow the clay particles to swell. For high-swelling clays, more time is needed for equilibration. After the mixing process, the slurry was transferred into a Büchner flask under vacuum of 15 to 25 inches of mercury (in Hg). See Figure 3-7. The flask was sealed off and the de-gassing process ensued for approximately 30 minutes to 1 hour. After the de-gassing stage, the slurry was transferred to a rigid tube. To reduce side-wall friction, the interior of the acrylic tube is greased with vacuum grease, and a floating tube setup is used after a consolidation stress over 100kPa is reached. For the resedimented specimens used in this research, the maximum stress reached was 100kPa, hence the floating setup was not utilized. The bottom of the rigid tube is sealed off with a tightly-fitting porous stone and nylon filter; thus, when the slurry is poured into the tube, it remains constrained inside. The funneling process can be seen in Figure 3-8. Care must be taken to perform the funneling in a continuous, fluid motion to avoid air entrapment. The top of the tube is closed off with another nylon filter and porous stone. Once the setup is complete, the outside container is filled with saline water to create a bath at the same salinity as the slurry to maintain a consistent

pore chemistry. The specimen is subsequently loaded with a Load Increment Ratio (LIR) of 1, to obtain enough primary consolidation without causing extrusion. LIR is the ratio of the added increment of stress over the current stress. The first load is the mass of the porous stone, followed by loading until a maximum load of 100kPa is reached. An LVDT (Linear Variable Differential Transformer) is anchored to a stationary surface and measures the displacement of the specimen when the spacer is protruding above water. An example of a curve with adequate resolution of vertical displacement can be seen in Figure 3-9. In the figure, the black circle indicates End Of Primary (EOP) consolidation, which is the point at which the majority of the deformation has occurred and the next load increment can be applied. After the first few increments, the setup should look similar to Figure 3-10. Once higher stresses are required, the hanger gravity system is utilized, as seen in Figure 3-11. The hanger system ensures even application of the stress, creating a level surface and a laterally uniform specimen. If the specimen is to be extruded and trimmed to be tested in a triaxial cell, an overconsolidation ratio (OCR) of 4 must be reached before extrusion. The OCR is the max(imum) past stress divided by the current stress. Hence if the max stress the specimen is taken to is 100kPa, this load must be held well into secondary compression to ensure sufficient settlement, with the final loading stage being 25kPa.

The final step in the resedimentation process is the extrusion of the specimen. In the case where the testing was performed in the rigid tube used for resedimentation, as seen in Figure 3-13, the clay specimen was taken to an OCR=1, and only partially extracted from the tube. Approximately 1 inch was cut off from either end of the specimen to eliminate any surficial inhomogeneities and to ensure a surface exactly orthogonal to the length of the tube. The clay specimen would remain in the tube for testing, with bender elements on either end, which will be described in section 3.3.4.

3.3.4 Experimental Setup

During the experimental process, the bender element endcaps, porous stones, and nylon filters are placed on either side, taking care to align the bender element tips

in phase with each other. The porous stones have a hole in the center to allow the bender element tip to protrude while maintaining a double-drainage system. In order to create contact between the bender element and the clay, a small disc of clay is cut to fit into the hole of the porous stone. This disc is scored and pushed onto the main body of the clay specimen at the appropriate place for alignment. The bender element tip is subsequently pushed into this disc of clay as the endcap comes into contact with the porous stone. The experimental setup is placed in the saline bath and incremental consolidation is performed on the clay specimen. Velocity measurements using the bender elements are taken at the EOP, which is the characteristic time when the majority of settlement has occurred, as marked in Figure 3-9. At this point, all the pore pressure incurred by the application of load has dissipated and will not present an effect in the velocity results. During each increment, the axial deformation is measured with an LVDT or measuring device in order to calculate the travel length of the S-wave for the velocity calculation.

Finally, at the conclusion of the experiment, the dimensions and masses are measured. After the soil has been oven-dried for 2-3 days, record the dry mass and to perform the necessary void ratio calculations.

Figure 3-1: The specimen of Ticino sand is prepared using a funnel and the rodding method, which involves using a long slender rod to puncture the sand and ensure uniform distribution. This is performed in three stages.

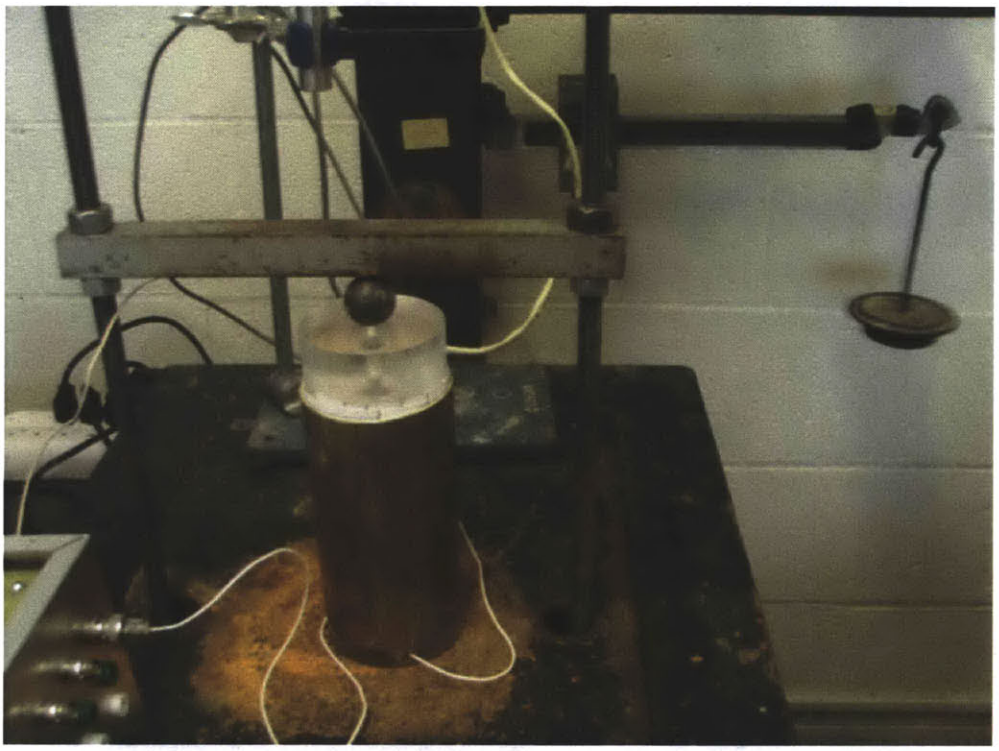

Figure 3-2: The dry sand specimen is loaded using the Terzaghi load frame pictured here

Series	Year	Researcher	Topic	Tests Performed
I	1961	Bailey	Effect of salt concentration on undrained shear strength	-
	1963	Jackson	Thixotropy	Triaxial
	1964	Varallyay	Influence of stress system on undrained strength	Triaxial
	1965	Ladd	Use of pressure transducer to measure soil pressure	-
	1965	Preston	Sample disturbance	Triaxial
	1966	Braathen	Disturbance effects on undrained strength	Triaxial
	1967	Dickey	Developpment of plane strain device	Plane Strain Device
	1967	Rixner	Behavior in plane strain at OCR 1, 2, 4	Plane Strain Device
	1968	Bovee	Behavior in plane strain at OCR 1, 2, 4	Plane Strain Device
	1970	Kinner	Behavior of strip footings during undrained loading	Model footing tests
II	1982	Germaine	Cross-anisotropic behavior at OCR 4	DSC, Triaxial
	1984	Bensari	Stress-strain and yielding behavior	Triaxial
	1985	O'Neill	Anisotropy of Thixotropic clay	DSC, Triaxial
	1986	Fayad	Volumetric and undrained behavior	Triaxial
	1987	Malek	Behavior under cyclic loading	DSS
III	1988	Walbaum	Investigation of sample disturbance	DSS
	1988	Sheahan	Modification of computer controlled triaxial apparatus	Triaxial
	1989	DeGroot	Behavior in undrained multidirectional DSS at OCR 1	DSS
	1990	Ahmed	Normalized behavior in DSS	DSS
	1990	Seah	Anisotropy at OCR 1	DSC
	1991	Ting	Performance of sand drains	Model testing
	1991	Sheahan	Time dependent material	Triaxial
	1992	Ortega	Computer automation of DSS	DSS
	1993	Cauble	Cyclic and post-cyclic behavior in simple shear	DSS
	1994	Santagata	Simulation os sampling disturbance in soft clays using triaxial tests	Triaxial
IV	1994	Sinfield	Simulation of sampling and effects on compression and shear	CRS, Triaxial
	1996	Cauble	Behavior of model suction caisson	Model caisson
	1998	Santagata	Pre-failure behavior	Triaxial
	1998	Force	Strain rate selection in triaxial tests	CRS
	2000	Gonzalez	Investigation of CRS consolidation	CRS
	2009	Abdulhadi	Stability of boreholes	Triaxial, Model BH
	2009	Moniz	Normalized behavior in triaxial extension	Triaxial

Figure 3-3: Many experiments have been conducted on BBC. These listed above represent tests performed on RBBC alone, indicating the large availability of data on this material [Abdulhadi, 2009].

Year	Researcher	Batch	w_l (%)	w_p (%)	I_p (%)	G_s	Clay fraction (%)	Salt g/L
1994	Zriek	powder	46.4	22.5	23.9	2.78	60.1	
1994	Sinfield	powder	47.0	23.8	23.2	2.79		
		402	46.8	22.4	24.4			
		403	47.2	23.3	23.9			
1996	Cauble	powder				2.81		
		401	46.7	21.8	24.9			
		404	47.4	21.9	25.5			10.4
		405	45.2	22.1	23.1			10.0
		406	45.0	22.6	22.4		57.6	12.5
		407	44.6	23.0	21.6		57.8	13.1
		408	44.7	23.9	20.8		58.7	10.1
		409	45.4	24.0	21.4		56.8	13.0
		410	46.6	25.0	21.6			13.4
		411	46.7	24.5	22.2		56.9	10.2
		413	45.5	24.3	21.2			9.7
		414	46.3	24.3	22.0			12.0
		415	46.1	24.7	21.4			10.5
		416	46.7	24.0	22.7			12.9
		417	47.2	24.5	22.7			13.2
1998	Santagata	418						
		419	47.8	23.3	24.5			
1998	Force	420	45.2	22.6	22.6			
2009	Abdulhadi	powder	46.5	23.5	23.0	2.81	56.0	11.1

Figure 3-4: The index properties listed are for Series IV RBBC and have been performed numerous times by different researchers, yielding consistent results [Abdulhadi, 2009].

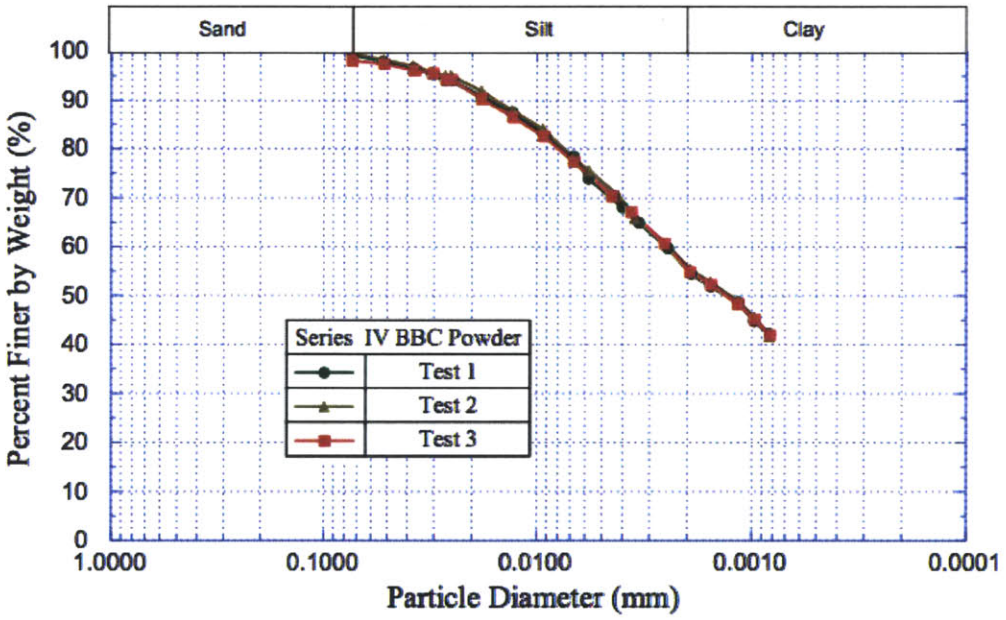

Figure 3-5: Grain size distribution tests on RBBC show consistent results within the Series IV batch [Abdulhadi, 2009].

Figure 3-6: Three components used to mix the slurry: sea salt (16g/L), ground BBC (1000g), distilled water (1L).

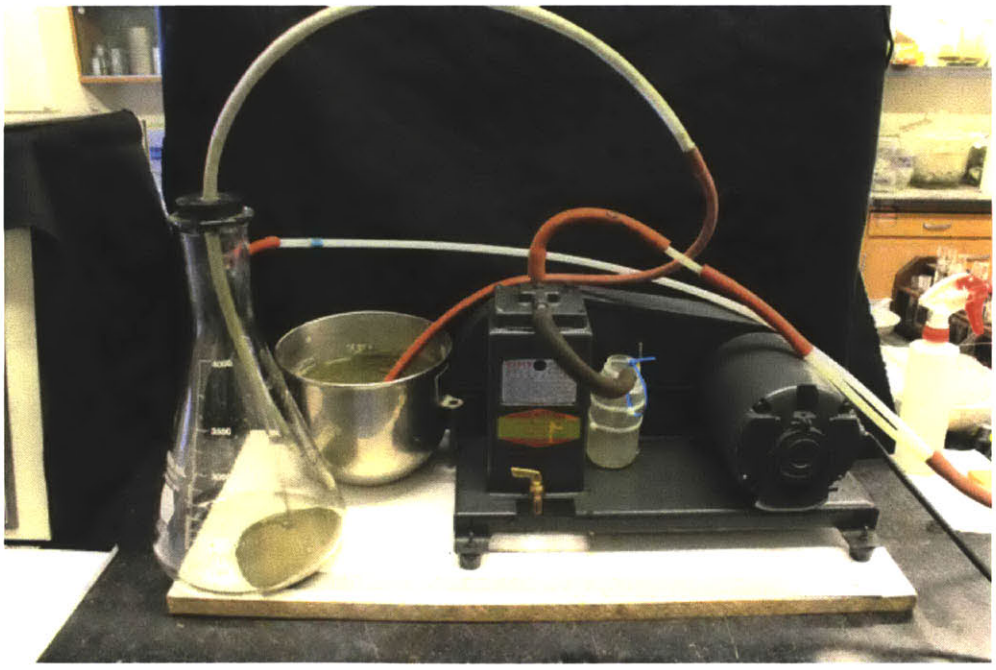

Figure 3-7: The de-airing station that ensures that no air bubbles are entrapped in the slurry.

(a) Initial stage of funneling (b) Progression of funneling

Figure 3-8: Funneling of the slurry into the floating tube setup. It is important to keep contact with the slurry continuously during deposition to avoid air entrapment.

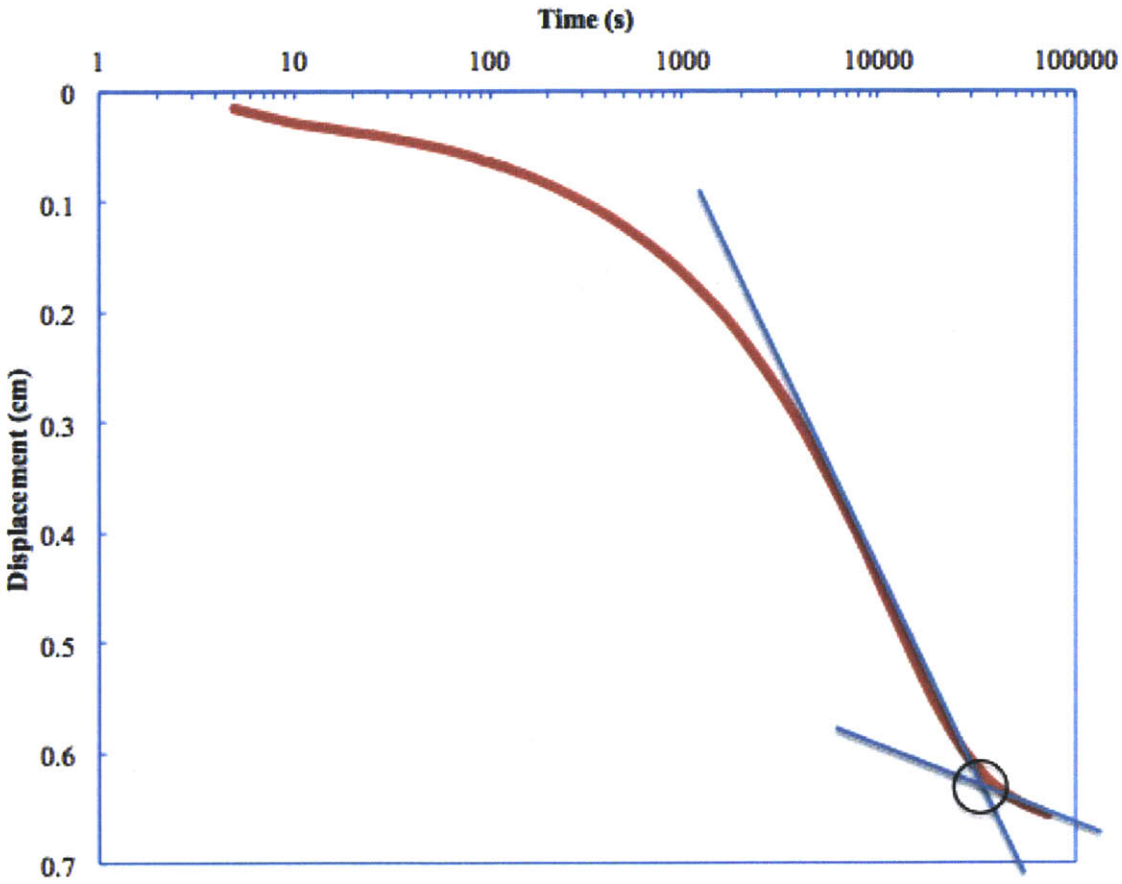

Figure 3-9: This settlement curve for RBBC indicates the End Of Primary (EOP) consolidation with a black circle. This point in time is when most of the deformation has occurred and there is an abrupt change of slope in the displacement v. time relation. The first slope is considered primary consolidation while the second slope is secondary compression which can generally be characterized as creep.

Figure 3-10: Post-funneling, a porous stone and incremental spacers are added on top of the slurry to begin the resedimentation process. It sits in a salt water bath (at the same salt concentration as the slurry was made) with double-drainage access.

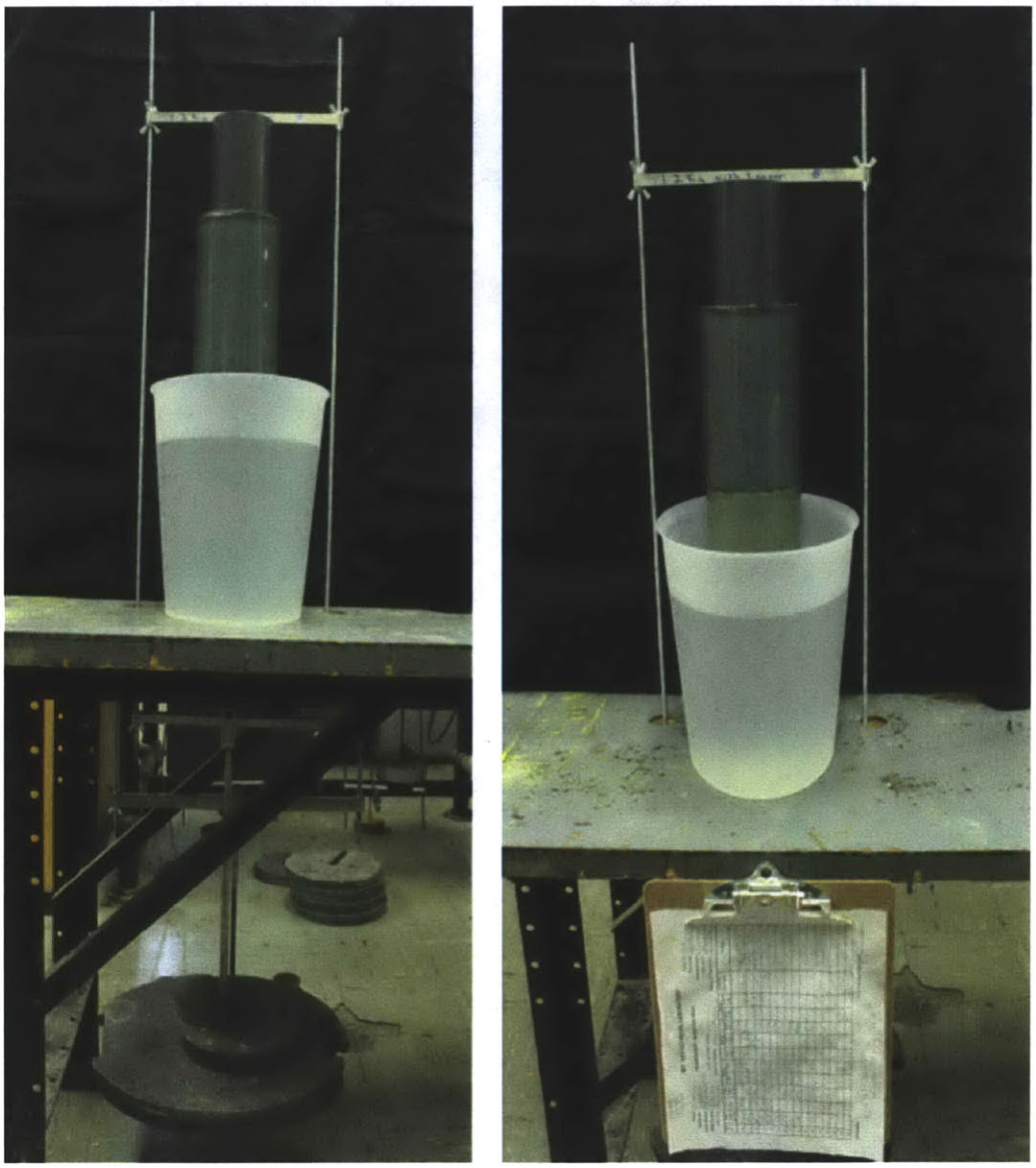

(a) Resedimentation setup with hanger (b) Resedimentation setup with clipboard

Figure 3-11: The resedimentation setup here demonstrates that the specimen is loaded using a spacer and hanger system, which ensures level application of pressure and stable setup.

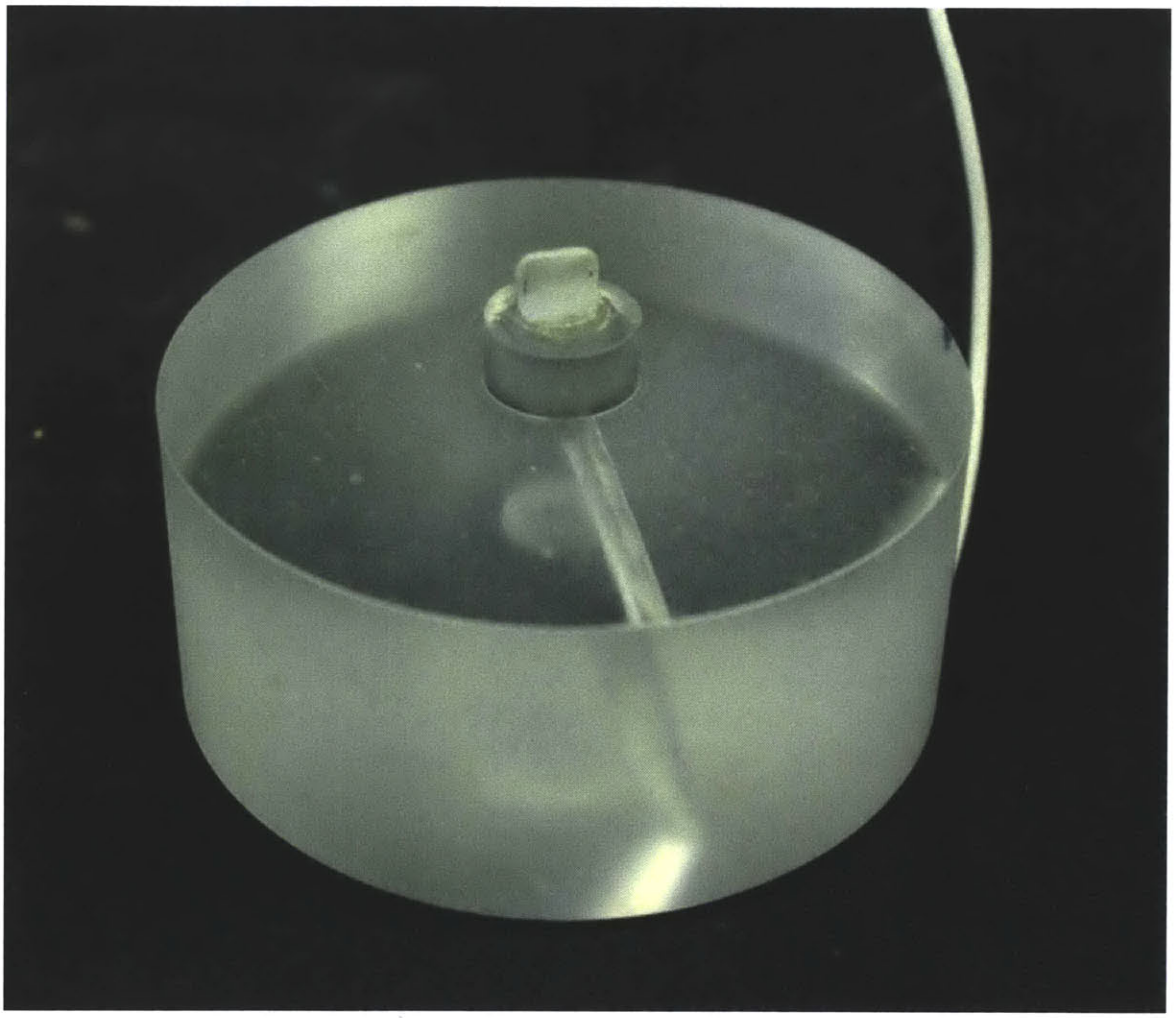

Figure 3-12: The bender element tips embedded in acrylic endcap that fits inside a standard 3 inch diameter sampling tube.

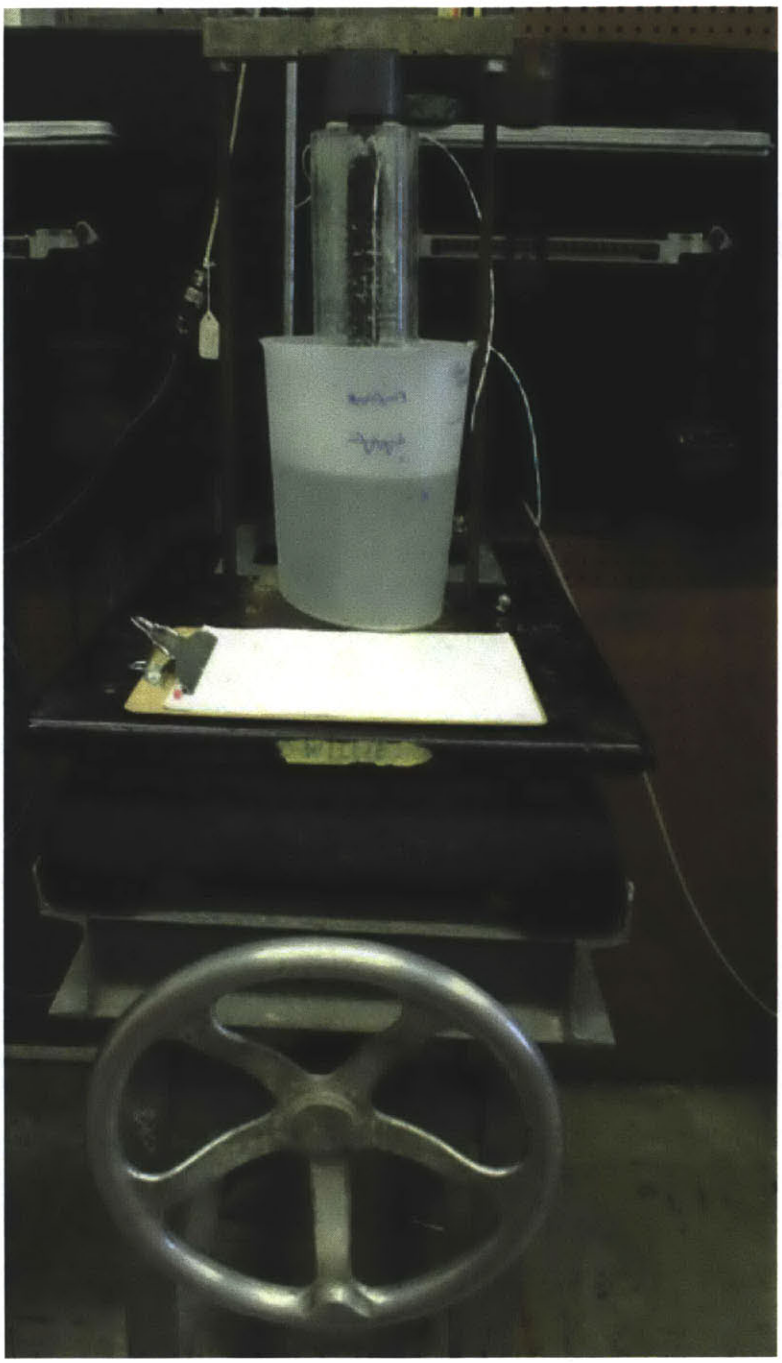

Figure 3-13: When the resedimentation process is complete, the specimen is prepared and placed in a salt water bath with bender element endcaps on either side of the specimen. It is incrementally loaded and velocity measurements are taken with the completion of primary consolidation during each increment.

Chapter 4

Testing Equipment

4.1 Introduction to Laboratory Equipment

The equipment used during this research had the express purpose of verifying the reproducibility of modulus results of a material using various different techniques. This study began and primarily focuses on the use of bender elements and the measurement of the shear modulus (G_{max}); however, the use of P-wave transducers, accelerometers, and extensometers were utilized to establish a comparison of results based on testing format. This chapter provides an introduction to the equipment used for this comparison, including how to use it as well as how it works.

4.2 Bender Elements

4.2.1 Introduction

The bender elements primarily used for the experiments in this research were made at the University of Massachusetts, Amherst from plate stock produced at Piezo Systems Inc. (PZT-5B, configuration T220-A4-X,Y). They will later be referred to as Geometry B. As will be discussed in section 5.2, there was a parametric study done during this research on the geometry of the bender element tips, and it was seen that the UMass geometry (Geometry B) had the optimal dimensions.

4.2.2 Description of Equipment Characteristics

Bender elements are made out of two piezoceramic plates (PZT-5B lead zirconate titanate) with a thin layer of brass between them. The ceramic plates are externally plated with nickel electrodes for charge transfer. Piezoceramics can be used as both actuators and sensors. Actuators convert electrical energy into a mechanical motion while sensors create a voltage signal from mechanical motion. When a voltage is applied to the 2-layered element, one side expands while the other contracts, causing a bending motion, as seen in Figure 4-1. Similarly, the physical wave passing over a receiver piezoceramic sends a response that is transmitted as a voltage whose amplitude is dependent on the force being exerted on the 2-layer element. As the force begins to bend the actuator, a differential in charge is created to balance out the motion, which is the signal being read by the receiver. The piezoceramics used in this research were purchased from Piezo Systems, Inc (Woburn, MA, USA). Initially the dimensions [length x width x thickness] of the piezoceramic plates were [12.7 x 6.35 x 0.51mm], as can be seen in Figure 4-3, with the final dimensions post epoxy coating and embedment are [5.08 x 8.64 x 1.52mm] as seen in Figure 4-2 for Geometry B.

The energy transfer between the piezoceramics and power source/receiver occurs through a wired connection to the bending elements. Two or three wires are soldered to the piezoceramic plates to transmit the voltage to the bending actuators, depending on the poling of the device. The piezoceramics can be polled in parallel or in series. In both instances there is a positive and negative charge applied to the bending actuators. The negative charge is usually ground. In Figure 4-3, the bender element on the left is an example of a parallel-poled configuration, where the positive charge is applied at the center shim between the two bending plates. The ground wires are connected on both of the external faces. This 3-wired system allows the bender element to deflect twice as much as the series-poled scenario. The bender element on the right is in series, which has a single wire on each side of the piezoceramic material, mounted on nickel electrodes. This applies a voltage over both of the piezoceramic plates at the same time, allowing the elements to bend only half as much as the parallel

configuration. A comparison to a circuit board can be made to better explain the behavior. When a constant voltage of 10V is applied to a circuit with two resistors of equal resistance (for example R=4Ω), the total current in the parallel case is 5 Amps, with 2.5 Amps in each resistor. If the resistors are in series, the total resistance is R=8Ω, yielding a total current of 1.25 Amps, which is also experienced in each resistor. Hence the deflection of the bending elements is related to the behavior of the current, which is twice as much in each resistor when they are in parallel as opposed to in series. This makes a parallel configuration optimal as an actuator versus a receiver.

The amount of displacement of the bending actuators for parallel and series can be calculated from the respective equation below:

$$\Delta x_p = \frac{3L^2 V d_{31}}{T^2} \tag{4.1}$$

$$\Delta x_s = \frac{3L^2 V d_{31}}{2T^2} \tag{4.2}$$

These equations are assuming that the elements act like beams, with one end fixed similar to a cantilever, as seen in Figure 4-1. In the above equations, Δx [m] is the amount of lateral displacement at the free end with no load, L[m] is the length of the bender element above the point of fixture, V [V] is the applied voltage, T [m] is the thickness of the bender element, and d_{31} is the piezoelectric charge constant [m/V]. The piezoelectric constant is a material property and for the piezoceramic material in the capacity of a bender actuator has a value of $d_{31} = 3.73 * 10^{-10}$ m/V, as specified by the distributor of the piezoelectrics. The length specified above is the length of the cantilever part and not the entire bender element. All the dimensional values are taken of the bender element before the epoxy coating since the behavior is based on the piezoceramic material and its material properties, thus only its dimensions are used. The presence of the epoxy coating likely decreases the displacement, although for these rough approximations, the epoxy effect was disregarded.

Using the equations above, the calculated lateral displacement was $\Delta x = 1.11 \mu m$ for the parallel configuration and $\Delta x = 0.555 \mu m$ for the series-poled case. The

larger displacement for the parallel configuration makes the energy transferal to soft mediums better, thus creating a stronger transmitted mechanical wave, which is why the parallel-poled motor is used to sending the signal. On the receiving end, the series-poled configuration is used since the same amount of deformation caused by the parallel sender causes twice as much voltage upon arrival at the receiving end. Ideally if a voltage of V=10V were sent with a parallel-poled bender element, the received output signal at the opposite series-poled end would read 20V; however, this would be the case of ideal situations and does not consider the attenuation, dispersion, and electrical losses in the system. Additionally this would require no lateral restraint, which is not the case as soon as the bender element tip is placed inside a soil specimen.

Strain rate has generally shown to have an effect on experimentally-obtained results, including strength and permeability factors. These factors vary as a function of the strain rate during the CRS and triaxial compression tests [Gonzalez, 2000]. As a first order comparison, the strain rate is calculated for the bender elements, although a comparison between various strain rates is not conducted explicitly. As will be discussed in section 5.1, there was not an observable frequency effect on the results from experiments conducted for this research. Since the strain rate is directly dependent on the frequency of the signal, it is evident that strain rate is not a governing factor in the results. The strain exhibited by the bender elements is calculated by the following equation:

$$\gamma = \Delta x / L \tag{4.3}$$

where γ is the shear strain, and L is the cantilever length of the bender element tip. The strain rate can then be calculated using the following:

$$\dot{\gamma} = 4 * \gamma / T \tag{4.4}$$

where T is the period of the signal, or the inverse of the frequency. There is a factor of 4 in the above equation to account for the fact that the maximum bending away from the resting position occurs after the completion of only a quarter of the wavelength.

Thus over the span of one period of the wave, the end of the cantilever tip travels 4 times the lateral distance calculated via equations 4.1 and 4.2.

Assuming an average shear wave velocity of $V_S = 150m/s$ and a frequency of $f = 8kHz$, the calculated strain is approximately $\gamma = 0.0219\%$ for the parallel configuration. Using this value and equation 4.4, the strain rate is $\dot{\gamma} = 700\%/sec.$ This strain rate is the maximum possible strain rate, since it considers that the full amount of deflection will occur for a given applied voltage; however, this is likely not the case after the bender element is pressed into a specimen, which incurs lateral restraint.

As previously mentioned, the bender elements were covered with epoxy to protect the piezoceramic material and electrically isolate the bender element from the soil and end pedestal. After the application of the uniform epoxy layer over the tips, the dimensions increased to [13.97 x 8.64 x 1.52mm] . The epoxy coating was cast using the molds shown in Figure 4-4, with a brass part to hold the bender element plate in place and the teflon part to house the epoxy in place. The brass rig clamps on to the small section of bender element below the area where the wires were soldered onto the plates. Thus, the soldered wires are also partly covered by epoxy to further secure the electrical connection. Due to teflon's non-adhesive behavior, the encapsulated bender element tips are easily extracted once the mold is taken apart. This system was used for the production of the bender elements with Geometry B (from UMass Amherst). At the MIT Geotechnical laboratory, the bender elements were created using a variation of the above procedures. Rather than soldering the wires onto the piezoceramic plates, a conductive epoxy was used to adhere the wires to the nickel surface. This avoided the requirement to solder wires to the piezoceramic material, which proved to be more difficult than conventional wire-to-wire soldering. Another variation to the procedures used at UMass was the epoxy coating step. Initially at the MIT laboratory, the epoxy coating was placed arbitrarily and allowed to flow until it cured. This, however, was one of the contributing factors to the different velocity results measured between different bender element tip geometries. The epoxy coating, coupled with the differences in bender element tip geometries, as discussed in section

5.2, was shown to cause a difference in velocities by more than a factor of 2.

Another consideration to be taken into account when constructing the bender elements is the crosstalk effect caused by the electromagnetic coupling of bender elements, such as exhibited by numerous researchers [Lee and Santamarina, 2005, Alramahi et al., 2008, Cha and Cho, 2007]. Crosstalk manifests itself very early in the output signal. The output signal crosstalk causes a wave to occur at the same time as the input signal, which would imply infinite velocity. It is generally easily distinguishable and does not pose an extreme impediment to signal interpretation, but the elimination of crosstalk can eliminate unwanted signal. This is achieved by ensuring the soil is electrically grounded with the bender element tips. Electrically grounding the soil to the bender element also prevents the saturation of the received signal, rendering the velocity measurements uninterpretable.

4.2.3 Data Acquisition System

The measuring system forms a closed loop as can be seen in Figure 4-5. The sending bender element is activated by a voltage sent from a function generator. The function generator is a National Instrument (NI USB-6251) device, which is controlled by the LabView Signal Express program on a PC computer. Using this program, the frequency and wave type can be specified. The prescribed frequency was chosen to be 8kHz for all the experimental results discussed in the results chapter. Additionally, a sinusoidal wave was chosen as the wave type, as opposed to a square, triangle, ramp, etc.. This topic will be discussed further in section 6.2. The input signal, upon arrival at the bender element, causes a lateral deformation of the piezoceramic tip that propagates a mechanical shear wave in the direction orthogonal to the end surface of the BE tip. The wave travels across the specimen and reaches the receiving BE tip, that generates a voltage signal as charge accumulates in an effort to equalize the movement it is experiencing from the mechanical wave. This voltage is amplified using a signal amplifier by 1000 times, and is fed into the data acquisition unit, which is combined with the function generator. Finally, this signal is fed into the computer for display and time averaging. The input signal is also displayed on the computer

along with the output signal. This is achieved by using a split BNC connector that allows the input signal to travel to both the sender bender element as well as the data acquisition system. The entire system is shown in the circuit diagram in Figure 4-5 and was used for all the bender element results from BE001 to BE043. After this point, due to technical difficulties with the computer program, the received signal was fed directly into an oscilloscope rather than into the data acquisition system and computer. This did not alter the received signals in any way and only allowed for more seamless data processing without technical interruptions. The computer was still needed since it drives the function generator that creates the input signal. The addition of the oscilloscope can be seen in Figure 4-6. On the left hand side is the signal amplifier unit which has multiple signal amplification capabilities and was used to amplify the bender element signal by 1000 times. The device in the middle is the National Instrument function generator, which transmits the voltage signal to the bender element. Lastly, on the far right hand is the oscilloscope into which the input voltage and the output voltage are fed. The signal acquisition is set to conduct continuous averaging (128 times) to obtain a smoother signal with minimal noise. Both of the signals are saved and processed manually for the calculation of the shear wave arrival time.

The data processing stage is performed using Excel to manually pick the arrival time from the output signal. This is one of the largest uncertainties concerned with the use of bender elements. If the signal is not clear, it can be difficult to decide which arrival time to select. The goal of this research has been to clarify this process by improving the quality of the output signal and control the parameters that might undesirably affect the results, such as cause side-boundary reflections that interfere with the shear wave propagating down the specimen. By conducting parametric studies with various bender element tips and various specimen geometries, the factors affecting velocity measurements have been identified. The aspect ratio of the bender element tip was shown to control the likelihood that a directly-traveling P-wave is produced. In addition, the aspect ratio of the specimen determines the clarity of the signal. Finally, with the systematic compilation and comparison of published results

for shear modulus values with those from this research have verified the validity of the measurements described in this thesis. Further details concerning the manner in which the arrival time is chosen are discussed in Chapter 5.

4.2.4 Spring System

During the testing of Ticino sand, a wider setup was utilized to control the boundary reflections discussed in Chapeter 5. When using the wider setup, such as the 20cm diameter steel tube, the load was applied directly on the acrylic bender element endcap that was placed directly on a piece of thin wooden disc with a hole in the center to allow for the protrusion of a bender element tip. Since it was deemed to insufficiently distribute the applied load over the surface of the specimen, a spring setup was adopted. As seen in Figure 4-7, load was applied on the outer ring of the specimen with springs. As the load was applied on the central acrylic endcap, the corresponding amount of compression was applied with clamps on the springs that transferred the load onto the specimen. Results are discussed in section 7.1.

4.3 P-wave Transducers

4.3.1 Introduction

The ultrasonic P-wave transducers used in this research were commercially purchased at Valpey Fisher Corporation, Hopkinton, MA. These custom piezoelectric transducers contain a $\frac{1}{4}$" 1MHz crystal that is housed in a metal casing, as seen in Figure 4-8. The size of the element determines the frequency that it produces.

4.3.2 Description of Equipment Characteristics

Requiring a peak to peak voltage of 50-100V, these immersible transducers produce a signal that does not require an amplification system like the bender elements. The transducer has a flat surface (as seen in Figure 4-9) that is put in contact with the material that is being tested. This flat surface is known as the matching layer, which

provides a reduction in the transition of impedance from the piezoelectric element and the material being tested. Impedance is the ratio of sound pressure over the particle velocity, which is an indicator of the amount of stress caused by the movement of molecules at a particular frequency [Mavko et al., 2003]. The acoustic impedance for the matching layer is between the impedance of the element and impedance of water.

The theory behind the way an ultrasonic piezoelectric transducer works is similar to the bender elements. Both use piezoceramic materials and deform when excited by a voltage. The difference lies in the way that the material deforms. The piezoelectric transducer contracts and expands longitudinally when a differential voltage is applied, which causes a mechanical vibration in the form of an acoustic wave to propagate.

Whereas the bender element needs to be inserted into the material, which is good for soft materials, the P-wave transducer only needs to contact the material at the surface. If the material is too soft, or the interface between the material and the transducer does not observe complete contact, no signal will be transmitted. This is often caused by the presence of air between the material and the transducer, which causes an acoustic impedance mismatch. The signal is reflected back rather than propagated through the material. In order to ensure coupling between the specimen and transducer, some o-ring grease can be applied. In the case of testing saturated clay specimens, the water acts as the couplant.

4.3.3 Data Acquisition System

The P-wave transducers are driven by a pulse generator. The one used in this research is the Agilent 214A Pulse Generator with the capacity to send a square wave at 1MHz and a voltage up to 100V. It can be seen in Figure 4-10. The choice of input wave is discussed in section 6.2. Similar to the data acquisition system for the bender elements, this setup is connected to an oscilloscope that reads the input and output voltage, which is then processed using Excel to select the P-wave arrival. The signals are still averaged (128 times) but no amplification system is necessary.

4.4 Accelerometers

4.4.1 Introduction

Included in this multi-equipment study of the shear and constrained moduli of materials is the accelerometer. The accelerometer used for this research is a monolithic Integrated Circuit (IC) that requires low power and yields high precision measurements of acceleration. The microchip used in this research is the Analog Devices Dual Axis Accelerometer (ADXL203), pictured in Figure 4-11.

4.4.2 Description of Equipment Characteristics and Experiment

The ADXL203 has dual axis capabilities, meaning that it can concurrently produce an analog output for the x and y directions, as depicted in Figure 4-12. Although the shear and P-wave measurements taken using these accelerometers could have been performed with a single axis, it proved useful to have dual axis functionality when the chip was mounted on the metal endcaps, thus allowing for simultaneous shear and P-wave measurements without re-orientation. These accelerometers require very little voltage (approximately 3-6V) and produce a strong signal with a sensitivity of 1000mV/g. As can be seen in Figure 4-14, given an input voltage of 5V, as was used during this research, the output voltage is approximately 0.75V, depending on the material and its attenuation properties. With an acceleration range of $\pm 1.7g$, the accelerometer has a shock survival of $3500g$.

The small size of the accelerometers (5x5x2mm), as can be seen in Figure 4-13, allows for the easy integration of the accelerometer in already existing test setups. To evaluate the potential of this technology with an application to geotechnical testing, experiments were conducted on common materials (i.e. acrylic, steel, aluminum) to compare the modulus results with other forms of measurement such as extensometers and P-wave transducers. The results will be discussed in section 7.4. The experimental setup can be seen in Figures 4-15(a) and 4-15(b). Wires were soldered to the

appropriate pins of the accelerometer, as listed in Figure 4-12, with the ground at pin 3, the outputs at pins 6 and 7, and the power wire at pin 8. The chips were then adhered to metal endcaps with superglue for signal transmission. The presence of the metal endcaps would alter the velocity reading but a zero was taken before data processing, so the offset was taken into account. Although the experimental setup is in a load frame, it was used for alignment purposes and only a nominal load was applied. The material being tested was placed between the two endcaps. An impulse was applied at the top portion of the load frame, directly above the line of propagation that would lead across both of the accelerometers. This was usually achieved by dropping a small metal ball (such as used in a ball bearing), or any other hard metal object at the top of the frame. This would send a P-wave through the specimen. For an S-wave, the top bar of the load frame would be struck in the lateral direction. Care was taken to ensure the orientation of the microchips was appropriate for the signal sent. Since the X and Y axes of the accelerometer were in the horizontal plane of the chip, it was oriented vertically, as seen in the closeup in Figure 4-15.

4.4.3 Data Acquisition System

The accelerometers were connected to a power source and an oscilloscope. The oscilloscope was able to log the impulse as it passed over the first and second accelerometer. The impulse was created by a blunt force caused by a hard object, such as a steel ball dropping at the top of the load frame. The time difference between the to signals was taken as the travel time over the length of the specimen. These calculations provided P and S-wave velocity results for various materials. No amplification or signal averaging was needed since only a single signal was measured at a time. The high sensitivity of the accelerometers powered at 5V created signals that often exceeded 5V if the impulse was struck too forcefully. When this occurred, the signal would be too saturated and square off when it reached 5V.

4.5 Extensometers

4.5.1 Introduction

As the final means of comparing the moduli of a material, extensometers were used to measure the Young's modulus of the material during uniaxial loading. An extensometer measures small deformations in length associated with applied stress. Using the stress-strain relationship during loading, the elastic modulus can be approximated from the slope of the initial portion of the curve. The contact extensometer used in this research was the Instron Industrial Products series 2620-826 item. These extensometers contain strain gauge units arranged in a Wheatstone bridge circuit and have the ability to measure dynamic testing up to $\pm 20\%$ strain with an input voltage of 4V.

4.5.2 Description of Equipment Characteristics and Experiment

The extensometers measure the amount of strain that occurs during loading of the specimen over the length of the gauge section. The displacements measured are over the length of the gauge length, thus when calculating the percent of strain, it is taken with respect to this distance. In the case of the extensometers used in this research, the gauge length was $l_g = 25.4mm$.

To attach the extensometers to the specimen, rubber bands were used to wrap around and bind one extensometer on either side of the specimen, as can be seen in Figure 4-17. While they are attached, two pins are engaged to hold the gauge length(Figure 4-16). Before loading, the pins are withdrawn, which allows the extensometer to measure displacement. The setup of the experiment can be seen in Figure 4-17. Vertical load was manually applied within the capacity of the load cell, which was 2000lbs. Both the loading and unloading portions were monitored when possible in order to verify the elastic behavior of the material.

4.5.3 Data Acquisition System

Initially the data acquisition was performed by the MIT Geotechnical Laboratory Centralized DAQ System; however, due to insufficient resolution, the AD1170 system was used to record the measurements. The AD1170 data acquisition card, as described in more detail in [Abdulhadi, 2009], is an analog to digital converter with high resolution (Analog Devices Inc.) with variable bit and integration time ratings. The bits range from 7 to 22, while the integration time ranges from 1 to 350ms. Additionally, a gain of 100 was used to further reduce the noise in the signal. For this testing, an integration time of 166.7ms with a resolution of 22 bits was used. The AD1170 averages the signal, which, combined with the high bit resolution, yields a high-quality signal with minimal noise.

4.6 New Equipment Development

4.6.1 Introduction

The Geotechnical Laboratory at MIT has been developing its equipment and procedures for many years, which includes the construction of custom equipment directly supervised by the researchers and instructors. The benefits extend from having an intimate familiarity with the equipment that allows for efficient troubleshooting and repair, to highly customized equipment that enables unique test setup parameters. The majority of this research was performed using the setup described in section 3.3.4, with two bender elements installed in acrylic endcaps that are placed on either side of the resedimentation tube; however, throughout the duration of this research, further equipment development was conducted. The goal was to have P and S-wave propagation capabilities in multiple directions. The first step is to establish a modified triaxial setup that has vertical data acquisition capabilities, as is described in subsequent sections. The prospective long-term goal is to include lateral transducers to simultaneously acquire vertical and lateral measurements.

4.6.2 Triaxial Setup

The setup used for the velocity testing of clay specimens is a modified triaxial, or more aptly named, a biaxial setup. The vertical stress and confining stress are varied to obtain the shear and constrained moduli of the specimen as a function of vertical effective stress. The specimen is loaded under K_0 conditions using a moveable vertical piston attached to a load cell, incrementally increasing the vertical stress from 100kPa to 1,000kPa, with unloading portions incorporated during this process. Figures 4-18(a) and 4-18(b) shows a 3D KeyCreator ™ representation of the experimental setup. As can be seen, a pedestal with drainage openings is inserted over the bottom pedestal to keep it in place. The top endcap is held in place by a tight flexible rubber membrane that surrounds the cubic specimen and is held onto the endcaps with greased o-rings. Both the top and bottom endcaps have drainage lines that permit flow from the porous stones to a channel that leads to either the bottom pedestal or a top drainage line. The flow is routed to the pore pressure plumbing in the manifold, which can be monitored and controlled with the use of pressure transducers. A closeup of the endcaps can be seen in Figures 4-19 and 4-20.

The triaxial setup is encompassed in a plexiglass cylindrical chamber which is transparent to allow for visual monitoring of the experiment. The chamber is filled with cell fluid (silicon oil) that surrounds the specimen and is pressurized to apply uniform lateral load on the specimen. The cell pressure and pore pressure are controlled by Pressure Volume Actuators (PVA's). The PVA's are controlled by a computer that acquires the real-time data from the monitoring transducers. Automation is an important aspect of running K_0 experiments since ensuring no deformation during loading of a flexible wall setup is a tedious process to perform manually. The K_0 conditions monitored by the computer feedback system is established by calculating the change in pore fluid relative to the axial displacement. The entire triaxial setup is held together with chamber rods, which keep the bearing plate and piston bearing assembly in place, allowing the axial stress to be applied by an external load frame. An internal load cell monitors the amount of axial load applied to the specimen and

vertical displacement is monitored using external Linear Variable Differential Transformers (LVDT's). The measured displacements are converted to strains, which are taken relative to the inputed geometry of the specimen. Before the initiation of K_0 consolidation, the volumetric strain is adjusted to match the value of the axial strain. The computer control thus keeps the volumetric strain and axial strain the same by increasing the cell pressure as the axial stress increases.

4.6.3 Data Acquisition

The advantages of a triaxial setup is complete control and automation of the setup of the experiment, which gives more accurate and precise results. In order to efficiently monitor the experiment, sensors are needed to obtain and feed back continuous information to the computer control system. The following components are required for the experimental process.

Centralized Data Acquisition System

The MIT Geotechnical Laboratory has a central data acquisition system that is used by virtually all the experimental setups. A Hewlett Packard HP3497A data acquisition unit is used as an analog to digital converter, which feeds the signals to a 486 microprocessor Windows PC. This system can monitor up to 160 channels with autoranging amplification capabilities, which enables low-noise signal detection without additional signal conditioning. The acquisition of data from the LVDT, load cell, and pressure pressure transducers are thus streamlined into one central unit for ease of analysis.

4.6.4 Square Triaxial Endcaps

The choice of square endcaps for this experimentation was a unique alteration to the normally-cylindrical triaxial setup. The reasons for this geometry include the ability to test three directions independently from each other. In addition, the equipment used to perform the velocity measurements is preferentially placed on a flat surface

rather than a curved surface to ensure optimal wave propagation. Finally, permeability and resistivity measurements are available for this geometry by [Adams, 2011], which proves a convenient form of comparison. The square endcap, as previously mentioned, houses a brass insert containing a P-wave transducer and bender element. See Figure 4-21 for the endcap without the brass insert. The P-wave transducer and bender element can be seen in Figure 4-22. They are connected to a board-board connecter header, which will be exposed at the bottom end of the brass insert. Inside the acrylic endcap is a board-board connector socket that is wired to a 9-pin electrical connector unit that passes the wires through the base of the triaxial cell. The wires are then externally connected to the signal source and oscilloscope.

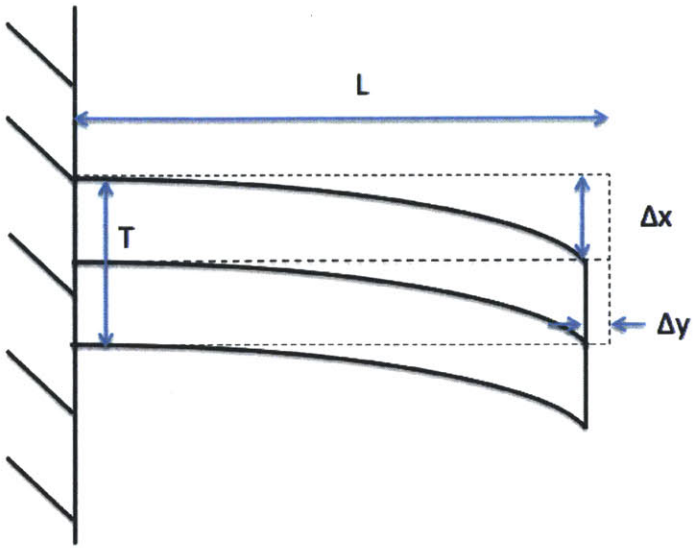

Figure 4-1: When a differential voltage is applied to the bender element, it deforms laterally as shown here. The input voltage, length (L), and thickness (T) are used to calculated the deflection (Δx). Δy is the change in length of the BE tip

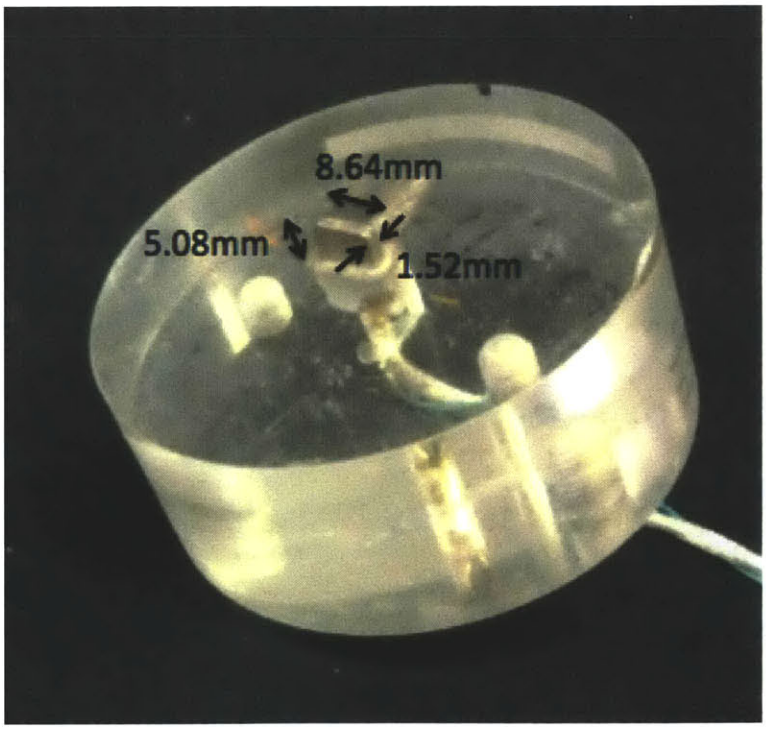

Figure 4-2: This bender element tip has been embedded into an acrylic endcap and acts like a cantilever, held rigid at one end. The dimensions shown are the ones used for the calculations of the bender element deflection. This bender element is already covered in epoxy. See Figure 4-3 for pre-epoxy example

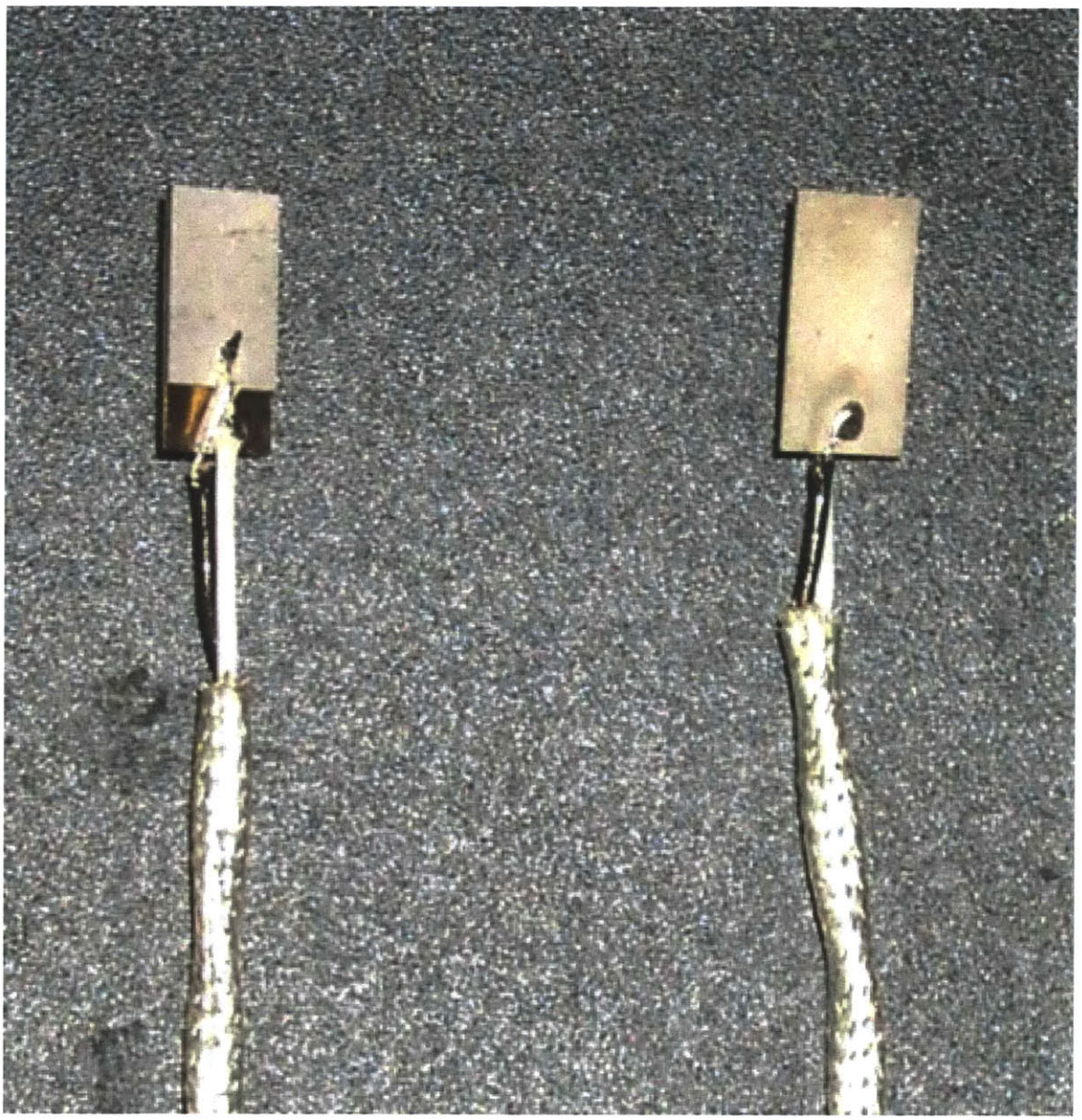

Figure 4-3: These are bender element tips that have been soldered to be in series and parallel. The left shows a piezo-ceramic plate in parallel, which is usually used as the sender since it can deflect twice as much as in series. The right hand side is wired in series, with the two lead wires on opposite sides of the plate. This configuration is usually used for receiving end (Picture courtesy [Landon, 2004])

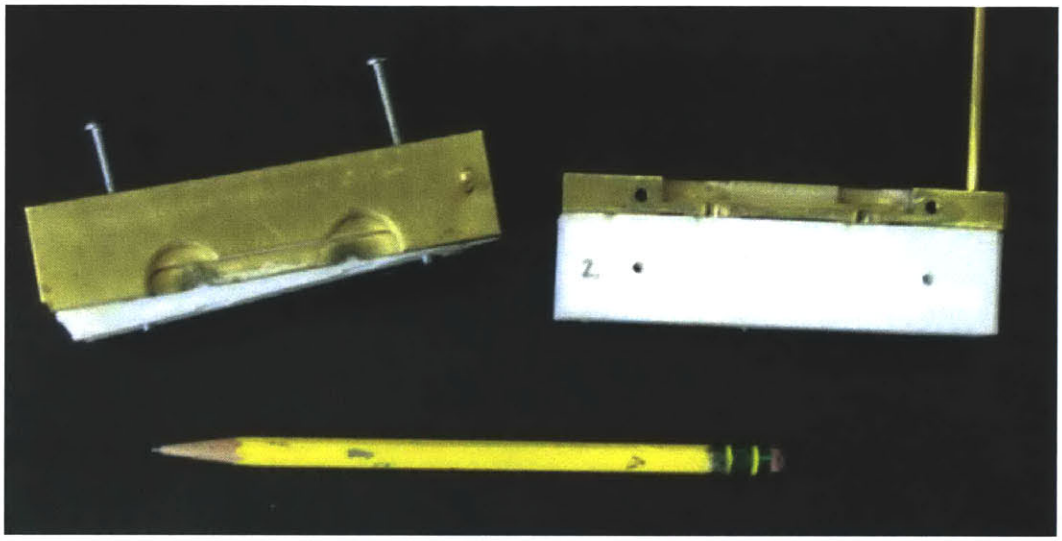

(a) First stage of casting the bender elements in the epoxy coating

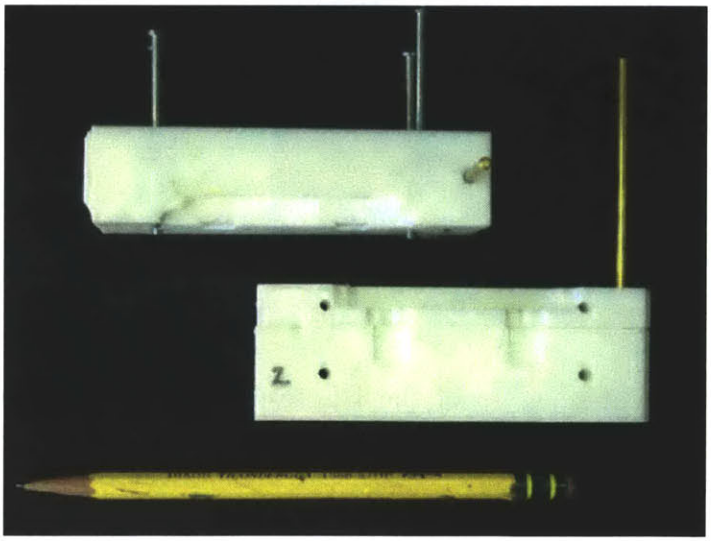

(b) Second stage of casting the bender elements, using teflon and brass cast

Figure 4-4: The wired ceramic plates are cast in epoxy for electrical insulation and water-proofing using a teflon mold and a brass clamping section [Landon, 2004]

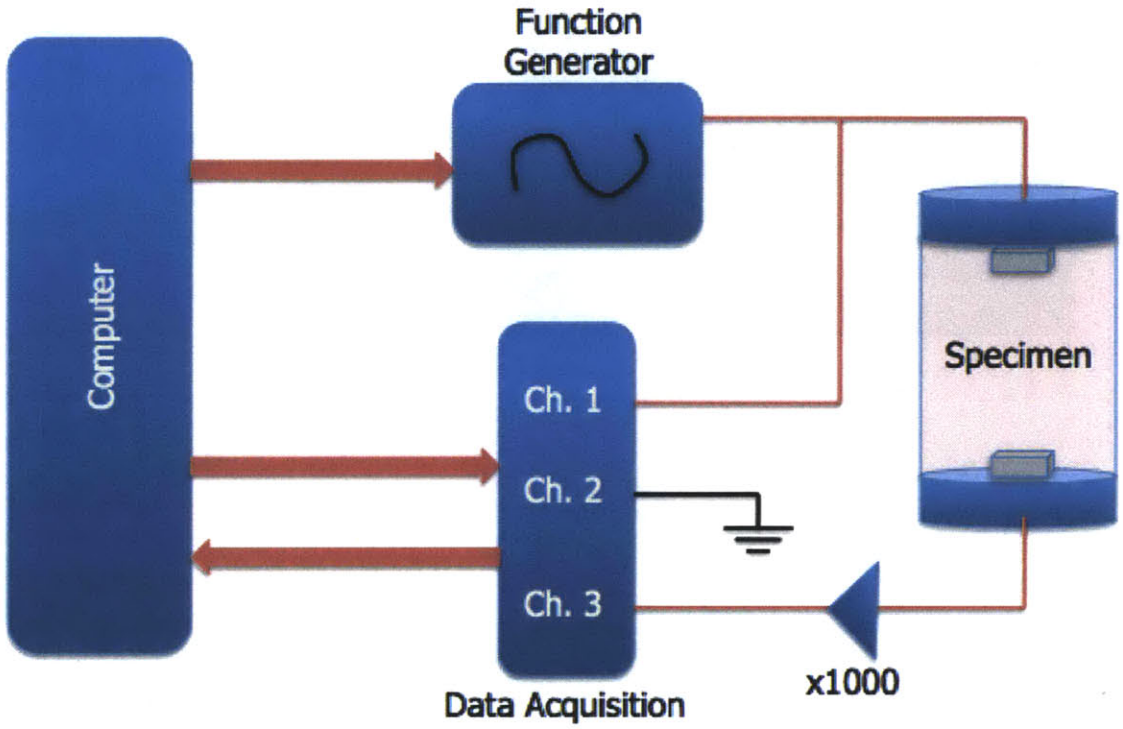

Figure 4-5: The circuit diagram of the BE testing scheme can be seen here. The function generator is commanded by a computer, which then sends an input signal into the bender element on one end of the specimen. The shear wave travels down the specimen and is received by the bender element at the other end. The signal is amplified by 1000 times and sent into the data acquisition system

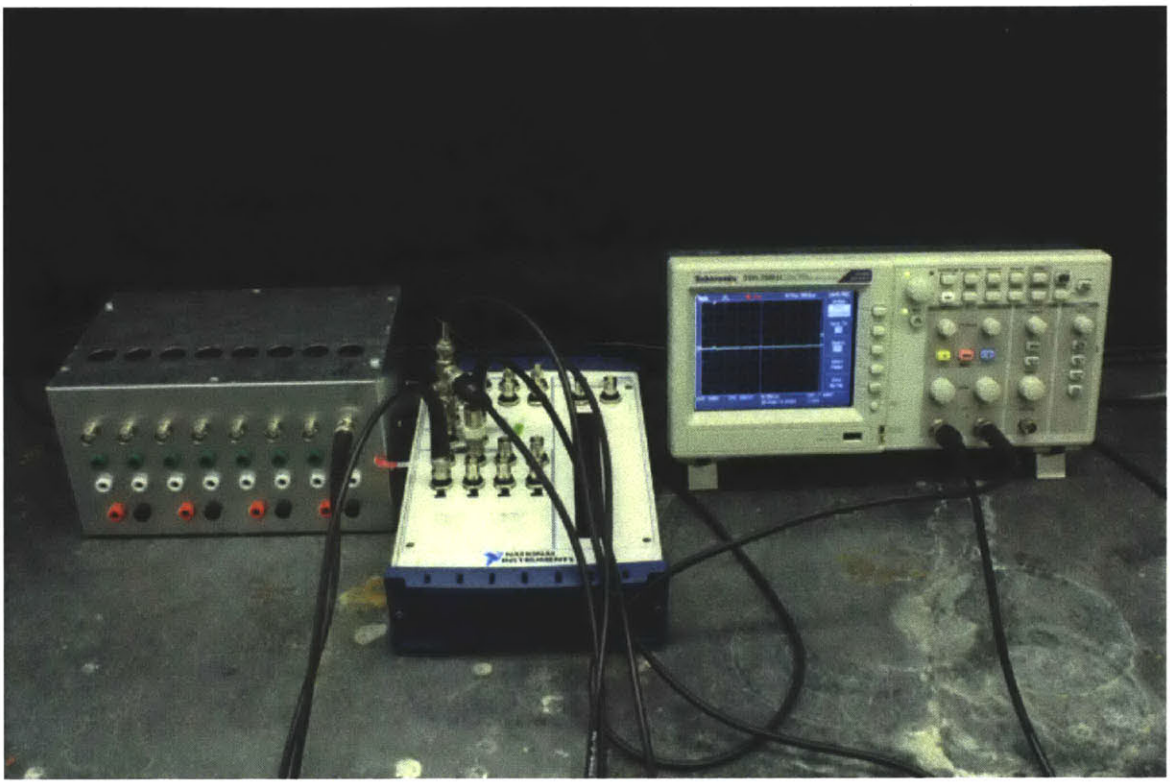

Figure 4-6: The bender element is driven by a National Instrument function generator at 10V and a frequency of 8kHz (shown in the middle and connected to a computer off to the side). On the far left is an amplifier that amplifies the output signal for higher resolution. On the far right is an oscilloscope that displays the input and output, which was incorporated for easier processing of output signal

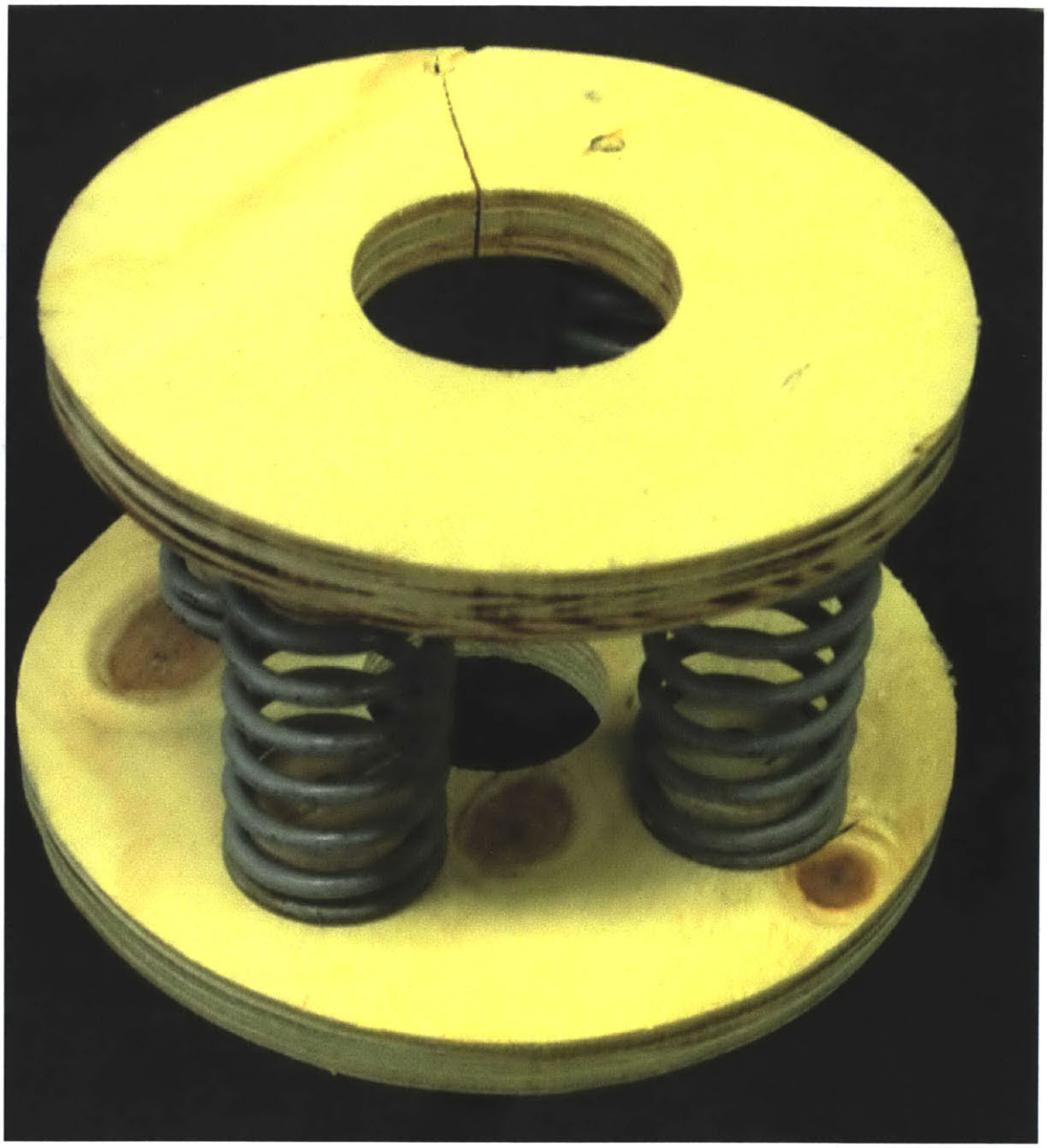

Figure 4-7: The springs seen here were compressed an amount equal to the force exerted on the central acrylic bender element endcaps that would be placed in the middle of this setup

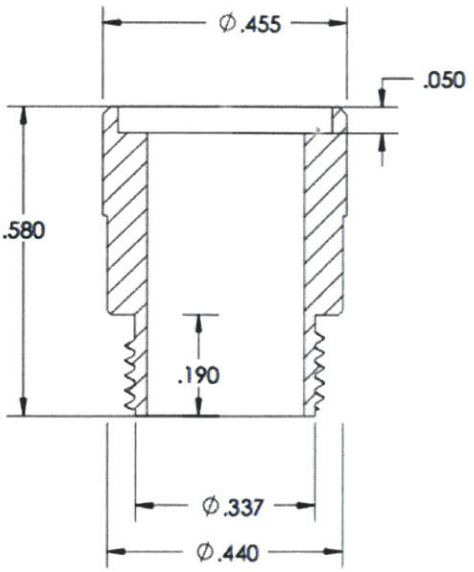

(a) Cross section of P-wave transducer

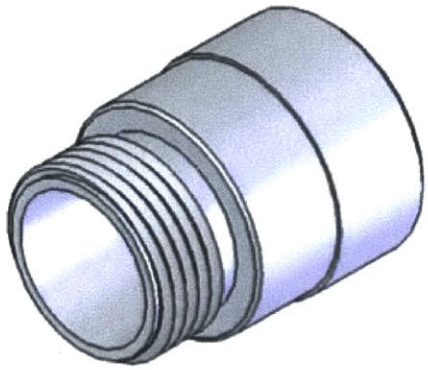

(b) 3D view of the P-wave transducer

Figure 4-8: This metal housing contains the piezoelectric crystal inside that has the capability to send a 1MHz P-wave signal through stiff mediums (Valpey.com). The side with the threading is the surface put in contact with the specimen. All dimensions in inches

Figure 4-9: An ultrasonic piezoelectric P-wave transducer, as shown here, was used for the P-wave signal transmission and acquisition

Figure 4-10: This square pulse generator sends a high voltage high frequency pulse to the P-wave transducer to propagate a signal

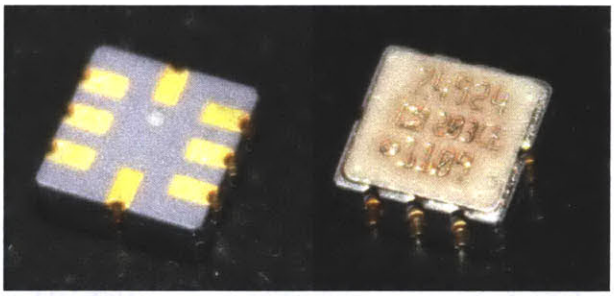

Figure 4-11: The accelerometer pictured above was used to pick up vibrations transmitted through stiff mediums

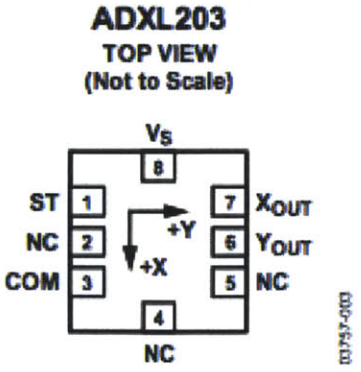

Figure 4-12: The various pins for connections are depicted above. For the dual-axis accelerometer, two signal channels are available (Analog Devices)

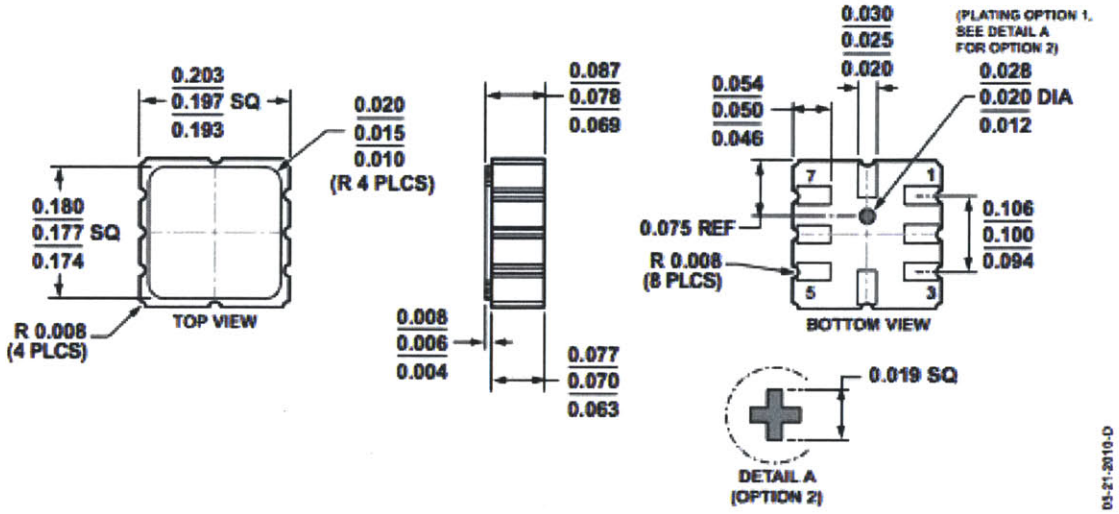

Figure 4-13: The versatility of this accelerometer is enhanced by its small size. The listed dimensions are listed in inches with a permissible margin of error (Analog Devices)

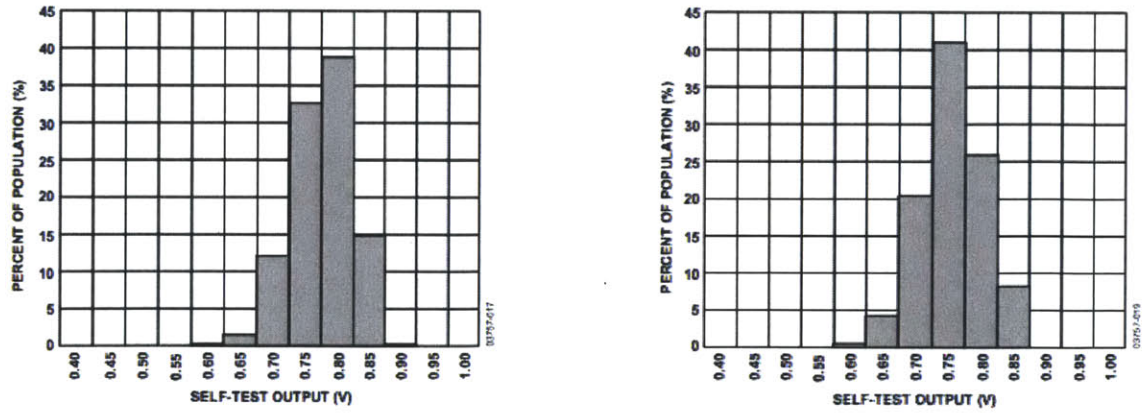

Figure 4-14: Given an input voltage of 5V, the received signal generates approximately 0.75V. The left graph is for X-axis results and the graph on the right is for Y-axis at 25°C (Analog Devices)

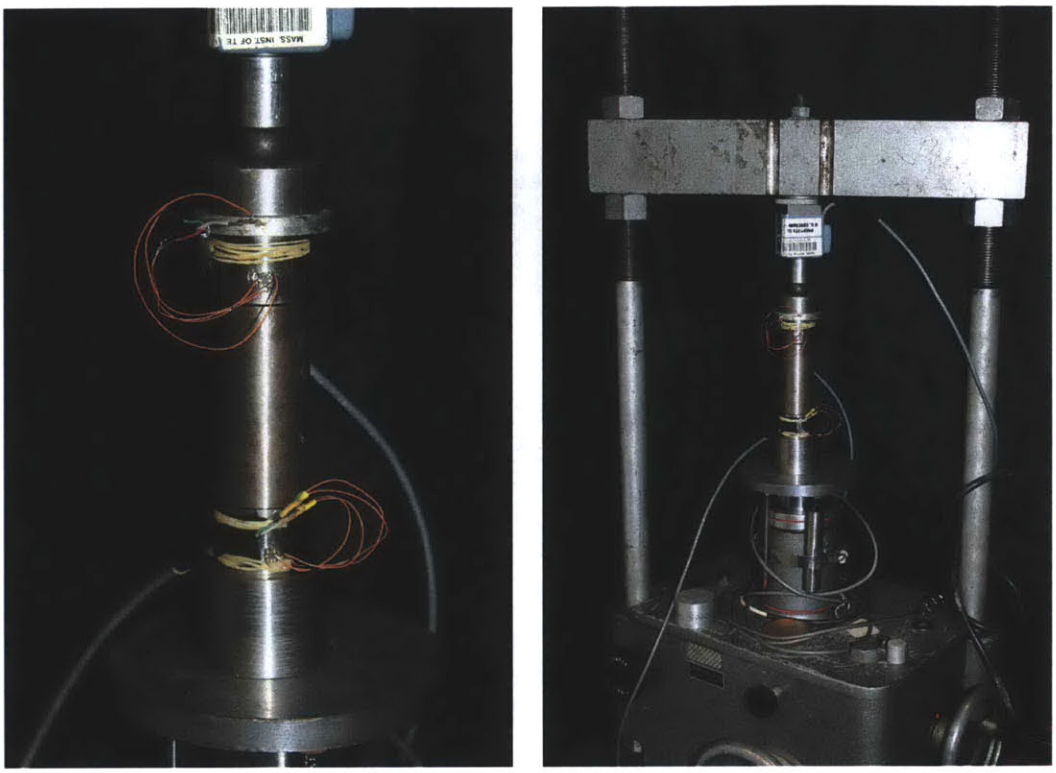

(a) Closeup of the accelerometers attached to endcaps with superglue

(b) Test setup for the accelerometer testing in a load frame

Figure 4-15: Pictured here is a setup used to measure the shear and longitudinal wave velocities through a steel cylinder using accelerometers. The signal is propagated with an impulse applied at the top extremity of the setup, thus allowing the wave to travel across both accelerometers. The travel time between the two signals is then calculated

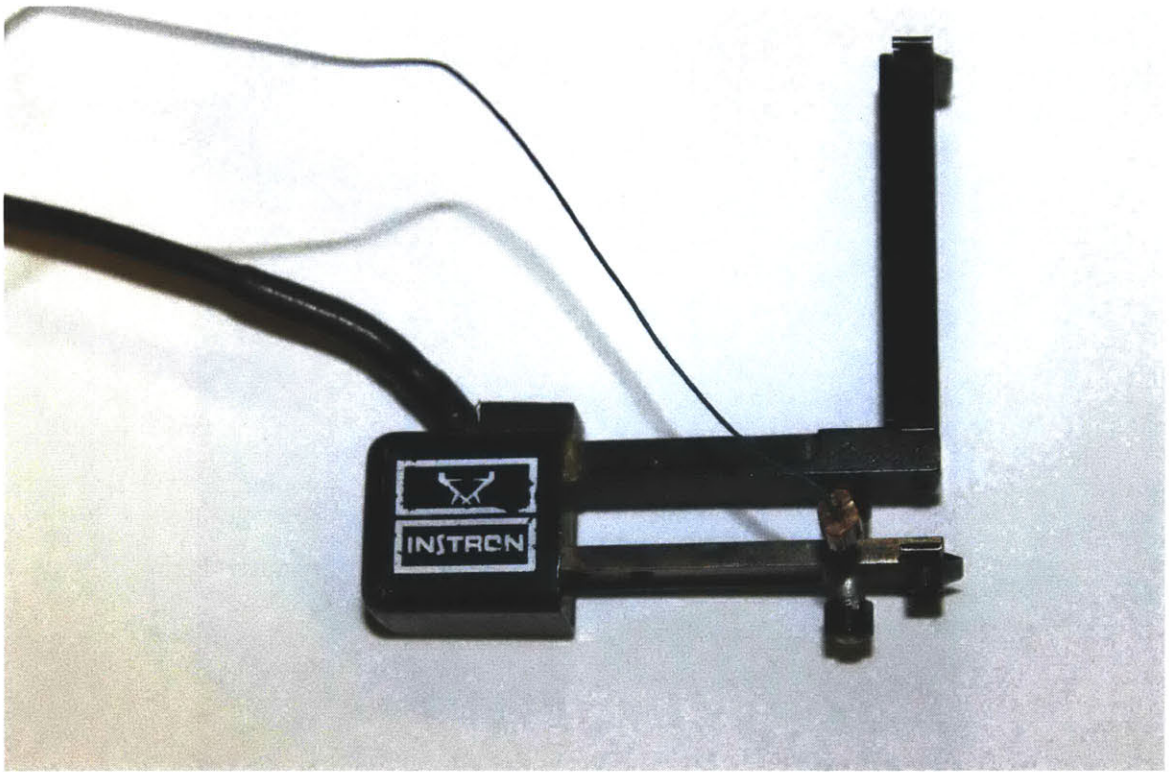

Figure 4-16: The extensometer pictured above was used for the stress-strain measurements of materials under uniaxial loading. The pin is engaged for the starting position, and before testing begins, it is taken out. This allows the extensometer to be in range when initializing the experiment

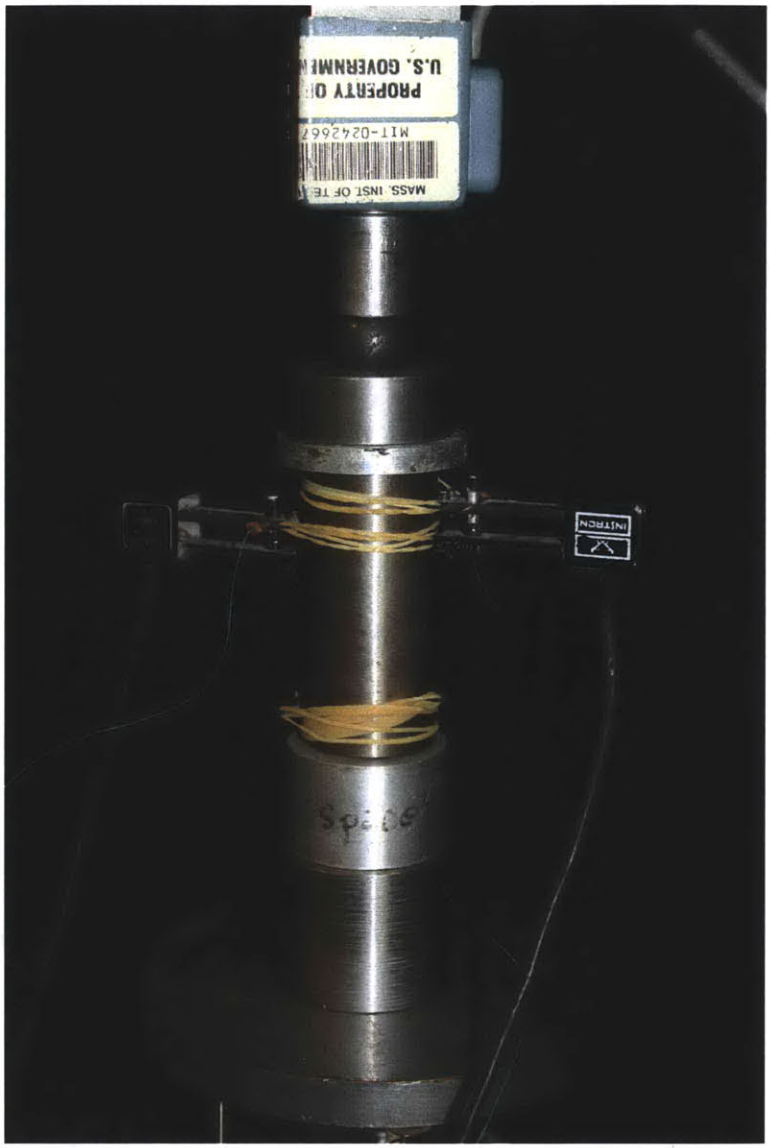

Figure 4-17: Extensometers are attached to either side of the specimen using rubber bands. The material is loaded manually up to 2000 lbs. The extensometers are attached to a AD1170 Data Acquisition Card, which feeds the results to a computer

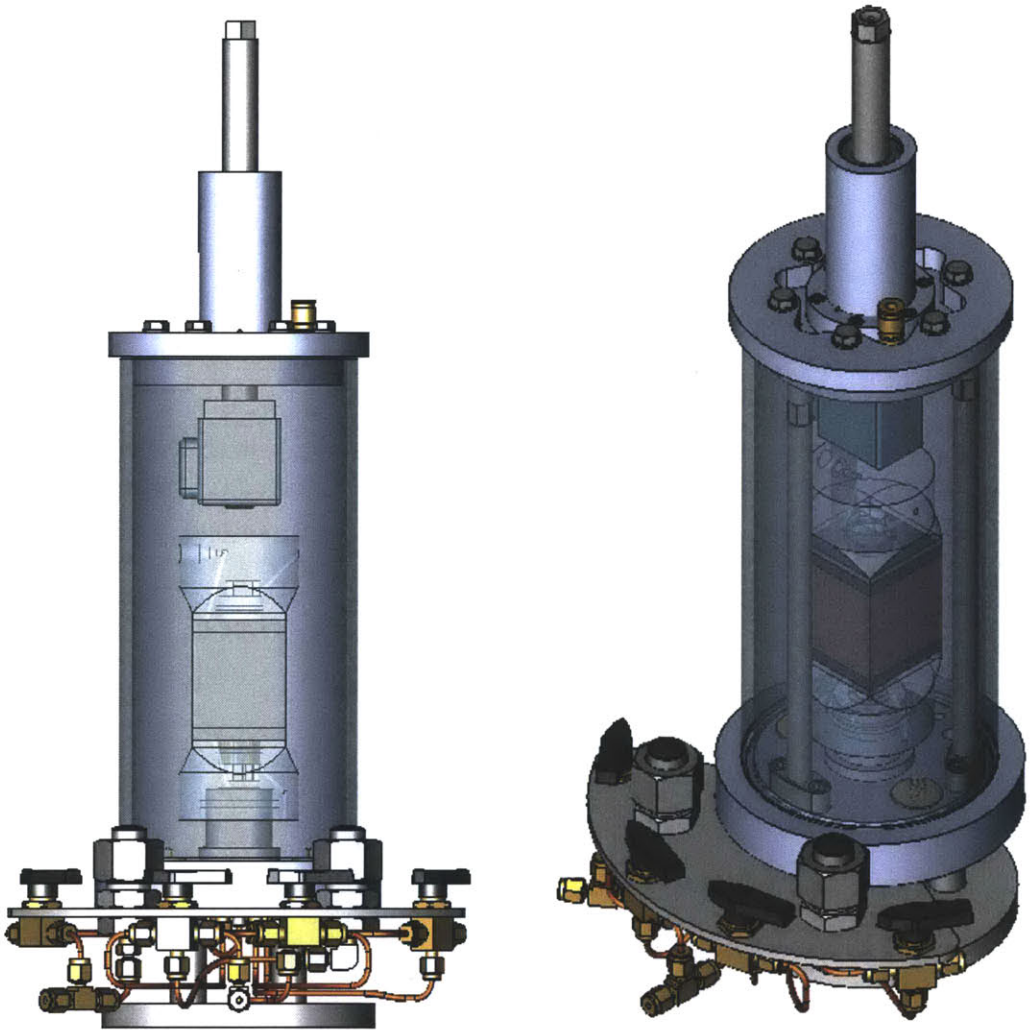

(a) Side view of modified triaxial velocity measurement setup without chamber rods

(b) 3D view of modified triaxial velocity measurement setup

Figure 4-18: Overall graphic of the modified triaxial setup used for velocity testing of cubic RBBC specimen under controlled vertical and cell pressures

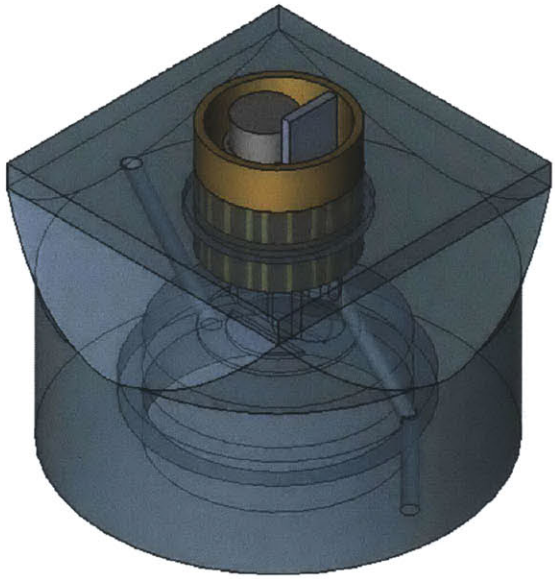

Figure 4-19: Above is a closeup of the square acrylic endcap with a removable brass cup that houses the bender element and P-wave transducer, held securely in place with an o-ring. Exposed is a drainage line that comes in contact with the porous stone and is controlled by the pore pressure PVA. The other visible channel that leads out of the bottom is for the electrical connections

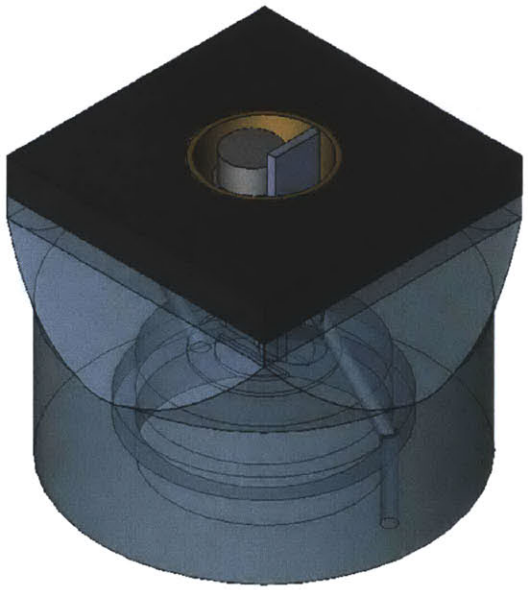

Figure 4-20: This closeup depicts how the porous stone fits around the brass cup and lies flush with the surface of the transducer. After a filter paper is placed onto the porous stone, the RBBC cubic specimen pushed onto the surface of the stone with the bender element protruding into the specimen and the P-wave transducer in contact with the surface

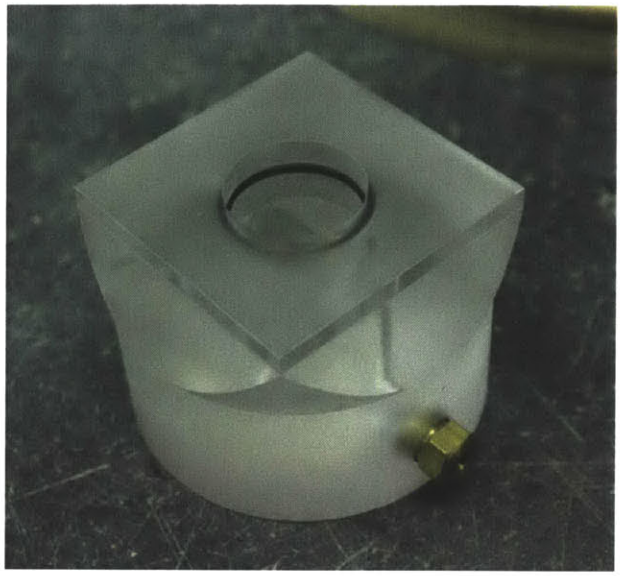

Figure 4-21: These acrylic endcaps have a versatile insert (now empty) that can house the desired transducers, including P-wave transducers and bender elements

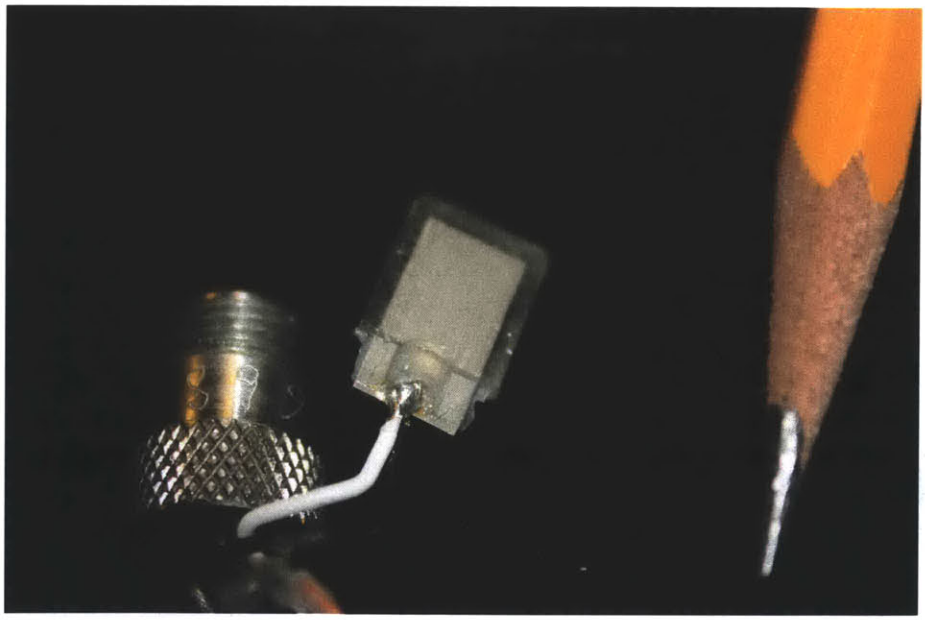

Figure 4-22: The bender element and P-wave transducer seen here are electrically connected to a board-board connector header, that are potted in a brass cup with epoxy. The brass cup is then connected to a board-board connector socket inside the acrylic endcap seen in Figure 4-21

Chapter 5

Investigation of Variables that Affect Bender Element Measurements

5.1 Frequency Effect

5.1.1 Bender Element Frequency Behavior

The input frequency at which the bender element behaves is dictated by the user. The general range for bender elements is from 2kHz to 20kHz, depending on the geometry of the tips. The decision of which frequency should be used to drive the bender elements depends on the test conditions and can be altered to produce the optimal output signal. The wavelength ratio, as discussed in section 5.3.1, is one of the limiting factors of the input frequency used and always needs to be calculated to ensure sufficient wave repetitions. The frequency chosen can also depend on the material being tested. The attenuative qualities of a medium are sometimes more effectively overcome by altering the frequency. For example it was shown that by reducing the frequency in Figure 5-1 from 1MHz to 0.1MHz (when using ultrasonic transducers) one can increase the strength of the signal by a factor of 3 or more, with all other parameters held constant. Although Figure 5-1 is from an experiment with

ultrasonic S-wave transducers, the concept transcends to other mediums.

The frequency behavior of bender elements can be further explained be observing the frequency response of two bender element tips transmitting a signal directly to each other without any medium between them. When the bender element is agitated at a frequency lower than its natural resonant frequency (f_n), the wave that travels from the sender bender element tip is at that specific frequency, and eventually will resonate at a frequency approximately at the resonant frequency, as seen in Figure 5-2. However, if a frequency higher than f_n is applied as the input frequency, the bender element cannot send a wave at that high frequency but rather sends a wave at the f_n. This behavior can be seen in Figure 5-3. It should be noted that all graphs with bender elements have the output signal amplified by 1000 by the external signal amplifier. Additionally, the signal was again multiplied by 100 when indicated in the legend for clarity in the graph, so as to approximately match the scale of the input signal. Therefore, in Figure 5-10, when the first peak of the output signal has an amplitude of 10V, this really means that the voltage measured was 0.0001V. Figures 5-2 and 5-3 were conducted using a setup without an amplifier so they do not need to be divided by 1000.

5.1.2 Frequency Effect on Modulus Results

The frequency effect on the results of laboratory experiments has been a topic of discussion when trying to relate the laboratory results with field sonic logging results. The largest frequency effect can typically be seen in the P-wave velocities of partially-saturated materials tested at seismic versus ultrasonic velocities [Hofmann, 2006]. As can be seen in Figure 5-4, depending on the boundary conditions and the frequency at which the specimen is tested, the elastic constant changes in a non-linear fashion. The theoretical explanation is derived from the ability for the stiffness to increase due to the fluid-induced pressure. For example, during drained conditions if a high frequency wave passes over a partially saturated area, the tendency for the fluid to migrate and cause a pressure gradient adds to the overall stiffness of the system, increasing the value of the elastic constants. Reference Figure 5-5 for various situations where the

frequency can have an effect on the measured bulk modulus. As can be seen, the absence of a pore fluid shows the results to be independent of frequency, as well as when the boundary conditions are undrained. The drained conditions show a dramatic increase with increasing frequency.

The issues mentioned above are mostly faced with compressional waves because the presence of fluid highly affects the bulk and constrained moduli, while relatively small effect is seen in the shear modulus. Since a shear wave cannot travel through a fluid, the presence or absence of a fluid is theoretically irrelevant to the magnitude of the shear modulus, although it has been experimentally shown that dry specimens have higher S-wave velocities than saturated specimens [Mondol et al., 2008,Hofmann, 2006, Zimmer, 2003] due to the effect fluid has on the particle contact area.

During this research, the use of bender elements to obtain the shear wave velocity was found to be independent of the frequency used for the function generator, as seen in Figure 5-6 for a saturated BBC specimen with bender elements. The range at which the bender elements were driven was extremely small relative to the range needed to see a difference. After testing at various frequencies, a frequency of 8kHz was chosen for all the experiments on BBC.

5.2 Bender Element Tip Geometry

In order to better understand the bender element signals, the effect that the geometry of the bender element tips was investigated. A parametric study was performed on Ticino sand using the same setup and K_0 loading conditions. Multiple experiments were performed in a rigid tube to ensure repeatability. The three different geometries are described in Table 5.1

The results shown in Figure 5-7 indicate a strong effect on the velocity depending on the geometry of the bender element tips. The differences can be explained by the creation of additional waves due to the geometry of the specimen. If the bender element tips are wider and shorter (i.e. Geometry B), it is less likely for a side-traveling P-wave to occur. Hence the lowest H-T ratio will produce a clear forward propagating

Table 5.1: Specifications of the three different bender element tip geometries tested under the parametric study

Geometry	Height (mm)	Width (mm)	Thickness (mm)	H-T ratio	Description
A	6.97	6.95	2.91	2.4	Tip was epoxied by dipping method, causing rounded edges
B	5.37	8.72	2.32	2.3	Epoxied using a mold to have perpendicular square ends
C	5.7	7.12	1.55	3.7	Excessing epoxy placed on tips using dipping method. Uneven distribution of epoxy, and bender element was installed at an angle to the endcap

S-wave with minimal side-traveling longitudinal waves. In the case of Geometry A, the velocities are much higher since the recorded arrival time was a P-wave rather than an S-wave. The P-wave taken as the first arrival was a directly-traveling P-wave that was caused by the bender element geometry. For longer bender element tips, the amount of vertical displacement that occurs during deflection, signified by Δy in Figure 4-1, is greater, and thus is more likely to cause a P-wave signal. This is further supported by the fact that the velocity difference between Geometry A and B is about a factor of two, and usually the P-wave velocity is roughly two times the value of the S-wave velocity. Hence to say that the observed arrivals are P-waves would be a valid assumption.

Geometry C is an anomalous geometry for a couple of reasons. It had an excessive amount of epoxy coating the piezoceramic tip, which could alter the arrival of the signal or create a damping effect that would present a much slower signal. The epoxy could have also weakened the shear wave such that the signal that presents itself is a P-wave reflection that arrives much later. Additionally, it was imbedded into the endcap at a slight angle to the surface, thus when two endcaps are perfectly aligned

with each other, the propagating shear wave would not travel directly down the path of the specimen. Instead it would travel off the vertical axis and the observed signal could be a reflection, thus explaining the unusually slow shear wave arrival time.

The conclusion was to proceed with Geometry B since it had a low H-T ratio which would decrease the likelihood of P-wave propagation. Furthermore, as is discussed in section 7.1 and 7.2, the results from this bender element geometry proved to compared well with other published results. Finally, it is unlikely that a single exact geometry exits that can provide the best results. There is a range, with an H-T ratio less than 2.3 being a good upper limit. This ratio can be decreased further, however, this also decreases the strength of the signal since there is a smaller tip-to-soil contact area and embedment length. There is a theoretical lower bound were the tip becomes too small to effectively act as a cantilever; however, more testing needs to be performed to aptly assess this lower bound.

5.3 Specimen Boundary Effects

The boundary effects alter the quality of the signal and the validity of the results. Previous studies using bender elements [Leong et al., 2009, Jovicic et al., 1996, Kuila et al., 2011, Gajo et al., 1997, Fioravante and Capoferri, 2001, Piane et al., 2011, Cho and Finno, 2010] have used the triaxial cell setup, which can cause unwanted signal interference due to the geometry of the setup. Additionally, if sufficient distance is not kept between the two bender elements, other factors can alter the signals. In the proceeding sections, the specimen geometry is discussed, illuminating the balance required between the wavelength and aspect ratio of the specimen.

5.3.1 Geometric Ratios

The geometry of the specimen can greatly affect the signals and the clarity with which they are interpreted. Since the format of the experiments as well as the geometry of the specimens can vary greatly, it is vital that the following requirements be fulfilled regardless of the setup.

Wavelength Ratio

The wavelength ratio is defined as follows:

$$r_w = \frac{d}{\lambda} \tag{5.1}$$

where d is defined as the tip-to-tip length between the edges of the bender element tips, as depicted in Figure 5-9 and λ as the wavelength of the shear wave propagated through the specimen. The wavelength ratio needs to be greater than two in order to obtain an unambiguous signal. When the bender element tips are closer than this wavelength ratio of two, the near-field effect becomes apparent. The near-field is a perturbation in the received signal which often travels at the speed of a P-wave and can cause an error in the interpretation of the arrival time [Leong et al., 2009, Wang et al., 2007, Youn et al., 2008]. An example of the near-field effect can be seen in Figure 5-10. If a specific distance is required due to equipment restrictions, the frequency of the input signal can be altered.

The ultimate outcome of an experiment that violates the wavelength ratio is no only an incorrect signal, but also an incorrect velocity. The precursory wave might be mistaken for an S-wave arrival, and hence can cause higher velocity readings.

Aspect Ratio

The second ratio that is important for the clarity of the signals is the aspect ratio. It is defined as the following:

$$r_a = \frac{d}{2r} \quad or \quad \frac{d}{w} \tag{5.2}$$

In the case of a non-cylindrical specimen, w is the horizontal width of the specimen, such as the width of a cube. r is the radius of a cylindrical specimen. Again, the length measurements can be seen in Figure 5-9. The aspect ratio should be less than one, which would allow any side traveling wave to arrive after the directly propagating wave. A further discussion of this topic is in section 5.3.2.

To have the best aspect ratio would mean that the wavelength ratio is compro-

mised. As the aspect ratio decreases (if the specimen becomes shorter and wider), the distance between the tips decreases. Recalling equation 5.1, as d decreases, the ratio r_w decreases. Since r_w needs to be greater or equal to 2, this becomes an iterative process. It is an optimization that requires careful consideration. This is one of the driving factors for the cubic triaxial setup. The square specimen allows for a much smaller aspect ratio than a triaxial experiment, which usually has an r_a of between 2 and 2.5.

5.3.2 Ray Path Analysis

In the case that side-traveling P-waves are created by the bender elements, a ray path analysis would give some insight on which kind of wave interaction is occurring. Thus with the regular brass tube and the wider tubes, a series of experiments were performed to investigate the signal interference that might obscure the arrival of the S-wave. Although the ray path analysis assumes a perfectly elastic isotropic medium, which is not the case during our experimental setup, it does allow a rough estimate of the behavior of various waves. The reflections investigated include a P-P, P-P-P, P-P-P-P, P-S, CAR, and P'. All of these cases can be seen in Figure 5-11. The multiples of the P-P reflections describe a P wave that travels at an angle θ from the original surface, with different numbers of reflections. The P-S reflection indicates a P-wave converted into an S-wave at the boundary. The CAR is the critical angle of reflection and indicates an angle at which a side-traveling P-wave reaches the vertical boundary and travels along the boundary as a P-wave, until eventually reflecting back at the same angle to the receiver. When the wave is traveling along the boundary, it travels at the speed of the confining medium, which is brass in the case of this research. The critical angle is found from the following equation:

$$\theta_c = \sin^{-1}(c_1/c_2) \tag{5.3}$$

where c_1 and c_2 are the speeds at which the wave propagates through the primary medium and the secondary medium, respectively. Although initially considered, since

File Name	r_a	P'	S	P-P	P-P-P	P-P-P-P	P-S	CAR
BE021	0.38	0.00014	0.00024	0.00037	0.00070	0.00105	0.00053	0.00075
BE016	0.51	0.00016	0.00027	0.00024	0.00040	0.00058	0.00033	0.00048
BE009	0.96	0.00018	0.00032	0.00024	0.00039	0.00055	0.00034	0.00039

Table 5.2: Travel times (in seconds) of all the different reflection for various specimens with similar height but varying aspect ratios

the secondary medium was copper and the longitudinal velocities through copper are significantly higher than those through soil, it was evident that these CAR reflections were insignificant and would occur before the completion of the input signal, especially due to the high attenuation that occurs in the secondary medium. Finally the P' wave is a weak P-wave that can travel directly down the vertical axis. A directly traveling P-wave would be caused by the change in vertical distance of the bender element tip, as denoted by Δy in Figure 4-1. See Table 5.2 for example calculations of travel times for different travel paths.

A series of experiments was conducted using bender element Geometry A, which was the geometry that produced P-waves, causing high shear velocity readings. Referring to Figures 5-12, 5-13, and 5-14 it is evident that as the side boundaries widen, the signal is much clearer and there is a strong, distinct arrival, whereas if the d length is much longer and the r is smaller, the signal is not nearly as clear due to the many reflections that occur off the boundaries. Figures 5-12, 5-13, and 5-14 correspond to diameters of 7.5cm, 11.3cm and 20cm, respectively, while vertical distance was held relatively constant. A series of ray path calculations were conducted to assess whether the assumption that Geometry A causes P-waves to propagate was accurate. The widest geometry was selected for the ray path calculations and three scenarios were considered. The first signal recorded was taken to be either the S-wave arrival, the first P-P reflection, or a directly traveling P' wave. As can be seen in Figure 5-15, the times of the corresponding reflections were calculated assuming a Poisson's ratio of 0.3. For clarity, the arrows indicate where the max point of the wave would arrive.

In Figure 5-15(a),5-15(b), and 5-15(c), it is evident that the first two cases would not correspond to reasonable arrivals. The third case, however, would support the fact that there is a single P-wave that travels down the same path that the S-wave follows, while the rest of the reflections are greatly attenuated and decrease in strength due to the long distances they travel.

The same ray path calculation was performed for Geometry B, which does not produce orthogonally-traveling P-waves. The images seen in Figure 5-16 firstly indicate that the directly-traveling P' wave is not a reasonable explanation for the waves seen in the output signal. In Figure 5-16(c), if the first peak were the arrival of the P' wave, this would also not allow for a distinct S-wave arrival, and it does not explain the second peak in the signal. In the P-P case (Figure 5-16(b)), the arrival of a valid S-wave would not occur at all. The time at which the S-wave would arrive according to the ray path calculation does not have any identifiable peaks. Since the bender elements firstly produce shear wave signals and potential weak P-waves, it is evident that the lack of an S-wave would be the most unlikely case. It is clear that none of the calculated arrival times for reflections match up with signals. Finally, the last case in which the first arrival is an S-wave clearly shows that the P' does not occur and that the second peak can be explained by a side-traveling P-wave or alternatively the resonance of the bender element. As before, the CAR case was disregarded since the transmission of a wave through sand, then to the metal tube, and then back to the sand would likely cause an extensively weakened signal that would not show up in the output. The supporting images are shown in Figures 5-17 and 5-18.

5.3.3 Soft vs. Hard Boundary

As mentioned previously, the boundary can play a part in the wave propagation process. While the CAR reflection was taken to be negligible in the case that the confining material is brass since the signal would travel so quickly and be highly attenuated that it would not be picked up by the receiver, the effect of the boundary was considered in a different aspect. The stiffness of the boundary was altered to observe the effect it could have on the polarity of the signal. Revisiting Geometry A,

which was proven to produce a directly-traveling P'-wave and S-wave, two cases were tested. The first is the brass tube filled with Ticino sand, and the second was was a brass tube lined with paper on the inside and filled with Ticino sand. The brass acts as a stiff boundary while the paper produces a soft boundary that can change the polarity of a P-wave upon contact. Looking at Figure 5-19, the first two waves are identical, but the rest of the waves are almost exactly opposite in polarity. This supports the fact that the very first signal is a directly propagating P-wave, and the second is the arrival of the S-wave, neither of which would have changed in polarity since they do not come in contact with the boundary. The later reflections, however, all come in contact with the side boundary and change in polarity. Hence with the strong evidence that the Geometry A bender elements create P-waves in addition to S-waves, the alternative Geometry B, which clearly produced only S-waves, was adopted.

5.4 Stress Effect on Output Signal

The amplitude of the output signal acquired from the receiver bender element is greatly affected by the lateral restraint acting on the element. The amount of deflection experienced by the bender element, as seen in Equations 4.1 and 4.2, is governed by the geometry of the bender element tip and the differential voltage applied to the bender elements. There is a linear relationship between the deflection experienced by the bender element and the force applied on it by the surrounding material. This relationship seen in Figure 5-20 is derived from the following equations for parallel and series, respectively:

$$F_p = \frac{4VWT}{3Lg_{31}} \tag{5.4}$$

$$F_s = \frac{2VWT}{3Lg_{31}} \tag{5.5}$$

where g_{31} is the piezoelectric voltage constant that relates mechanical stress applied to the electric field generated by the piezoelectric material, with units of Voltmeter/Newton. L, W, T are length, width, and thickness of the bender element tip, respectively. The piezoelectric voltage constant, as specified by manufacturers, was taken to be g_{31}=0.08798 Vm/N. The graph seen in Figure 5-21 depicts the output signal for a range of stresses, with the vertical axis representing the output voltage amplified by 1000 times. As clearly seen in the figure, as the vertical effective stress applied on the laterally confined Ticino sand increases, the output voltage decreases. The lateral force acting on the bender element can roughly be calculated assuming K_0 conditions with K_0=0.5 for sands. Using the equations above, one can calculate the allowable stress range and required input voltage to obtain signals.

5.5 Lag in Response

Similar to most data acquisition systems, the bender elements do have a electrical time lag in the response time from which the signal is activated to the time that it is received. This is partly due to the external wiring as well as the bender elements themselves. The proportion of the lag time attributed to these two parts is indistinguishable and irrelevant.

The lag time measurements can be performed by putting the two bender element tips together and observing the difference between the input and output signal. As can be seen in Figures 5-2 and 5-3, there is a delay between the input signal and the first output. In these two cases, the perceived lag time is not identical. This can be caused by the way the two tips are held together. If they are held exactly aligned, they produce a lag seen in Figure 5-2, whereas if they are slightly misaligned during this process, a greater lag is observed, as seen in Figure 5-3. In each of these, it is clear that the lag is very small and when incorporated in the calculation of the velocity, it is usually negligible. This is especially the case in the triaxial setup which is perfectly aligned, causing minimal lag.

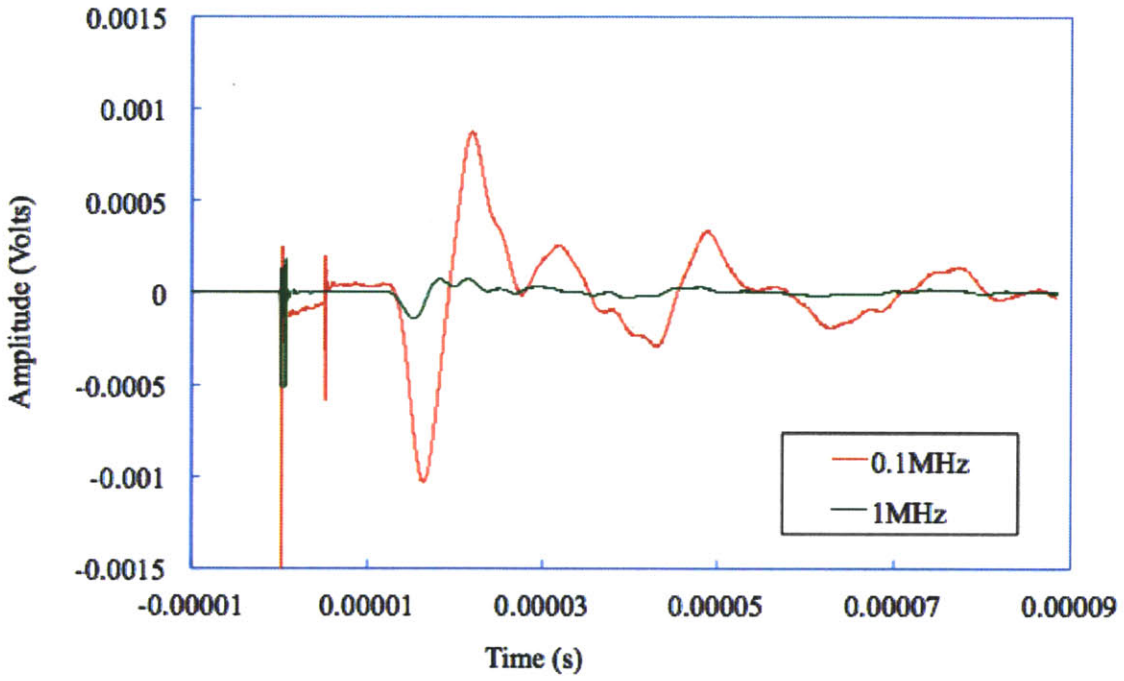

Figure 5-1: Using an ultrasonic piezoelectric S-wave transcuder of 1MHz, when altering the input frequency the amplitude of the voltage can change depending on the material tested. In this case, 300micron quartz sand is tested at 61kPa. Due to the attenuative properties of sand, the lower frequency input signal yields a signal of better quality. Note that the arrival time remains constant when the frequency is varied

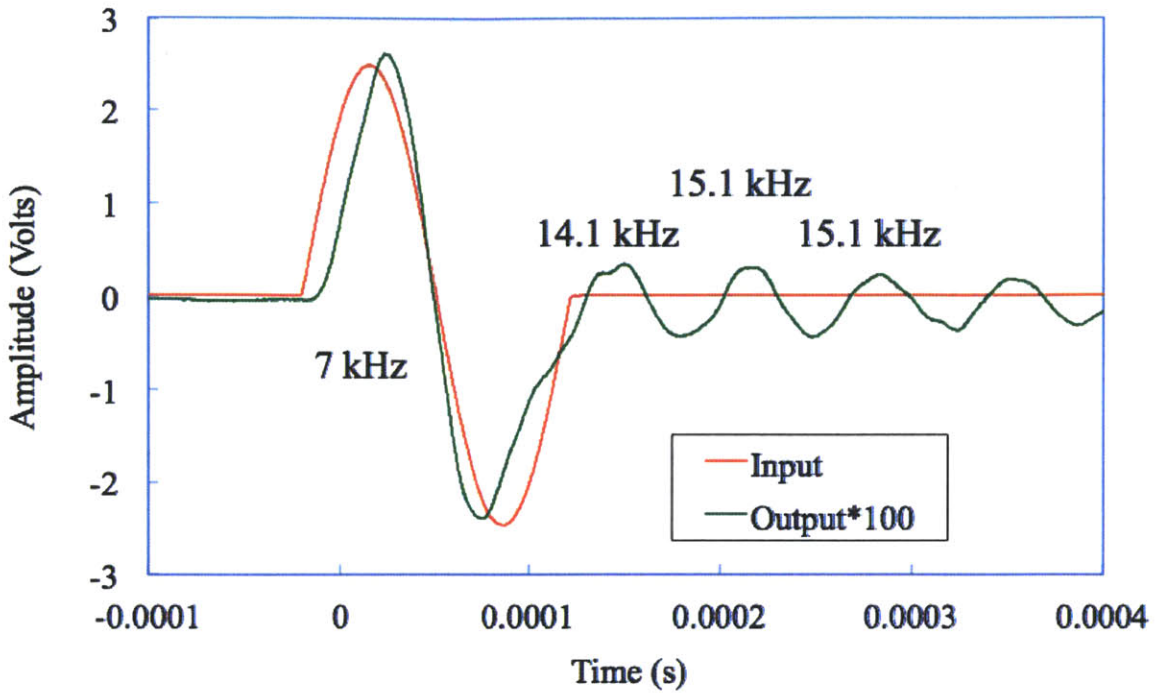

Figure 5-2: When the bender element is driven at a frequency below its natural resonant frequency, such as at 7kHz, the output wave is at that driving frequency, while the later waves remain at the natural resonant frequency

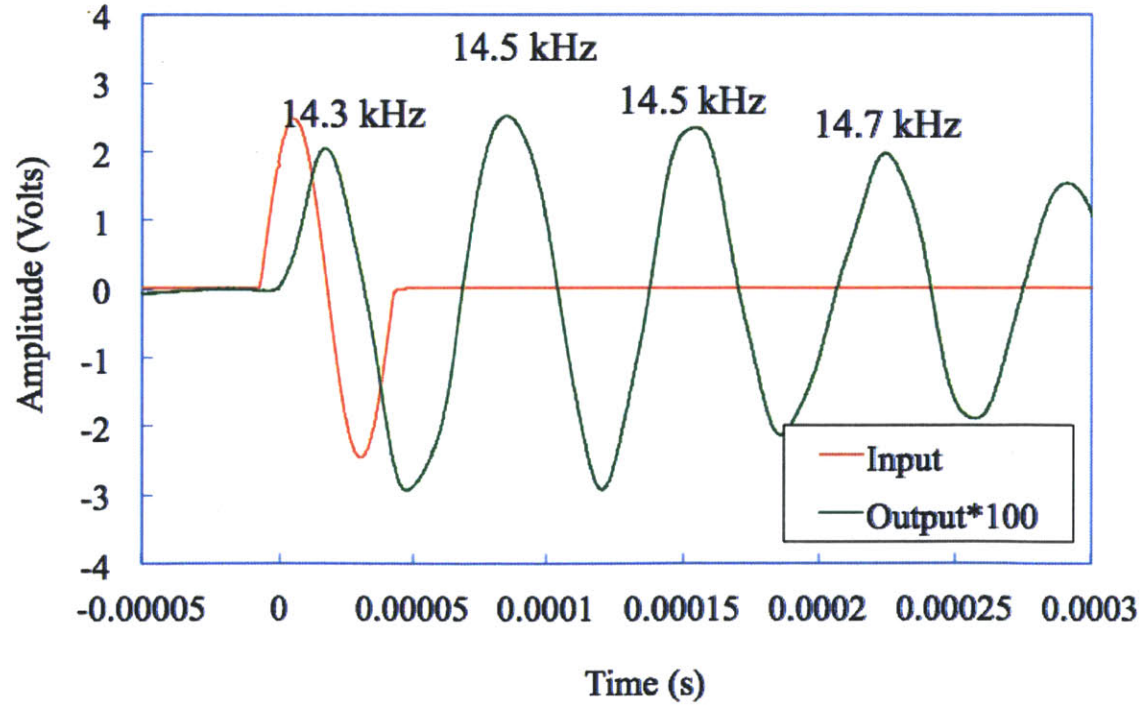

Figure 5-3: When the bender element is driven at a frequency higher its natural resonant frequency, such as at 20kHz, the output wave is at the resonant frequency

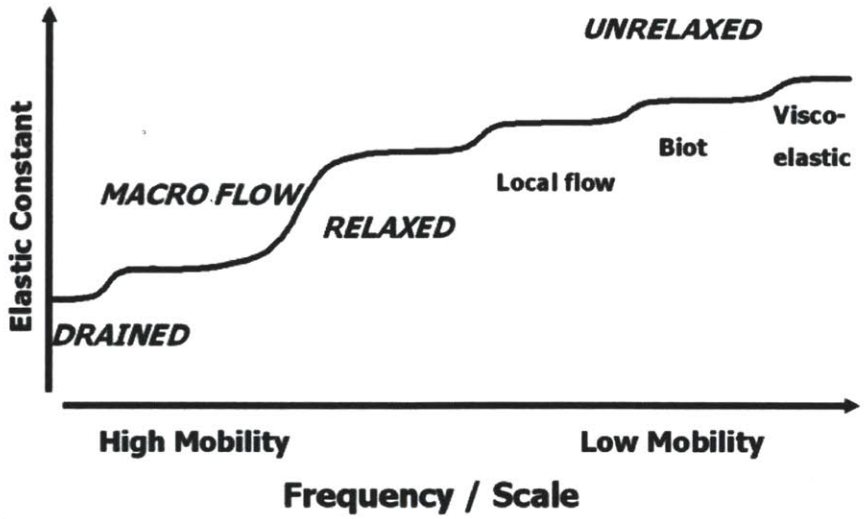

Figure 5-4: As the frequency of the input wave increases, there is a larger tendency for frequency-dependent properties to govern the results [Hofmann, 2006]

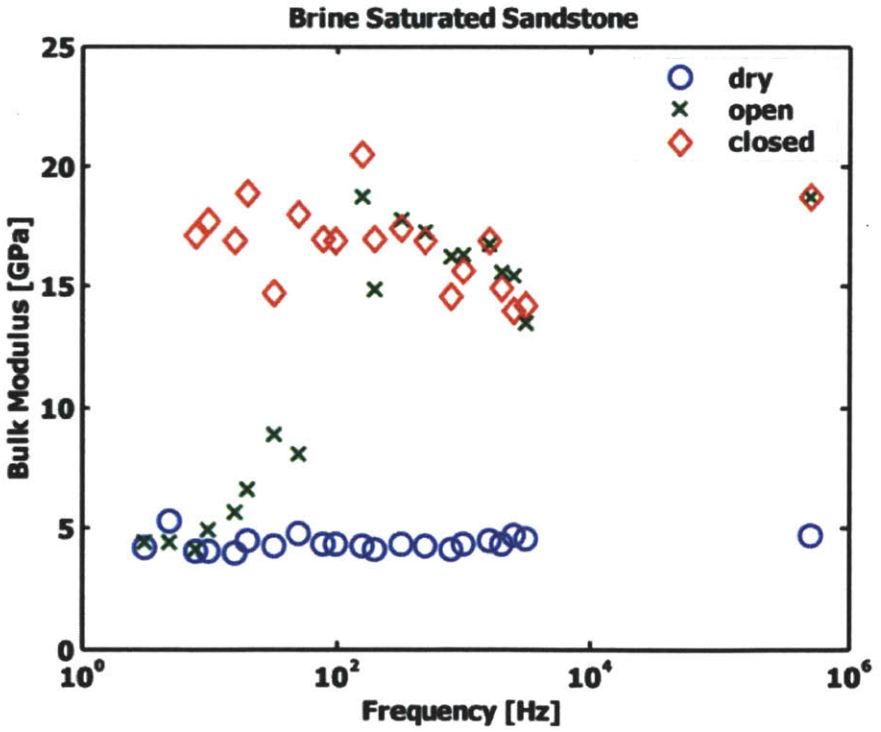

Figure 5-5: The frequency effect was observed to have the largest impact on bulk modulus results for a partially saturated drained specimen. Under higher frequencies, fluid migration causes higher stiffness values [Hofmann, 2006]

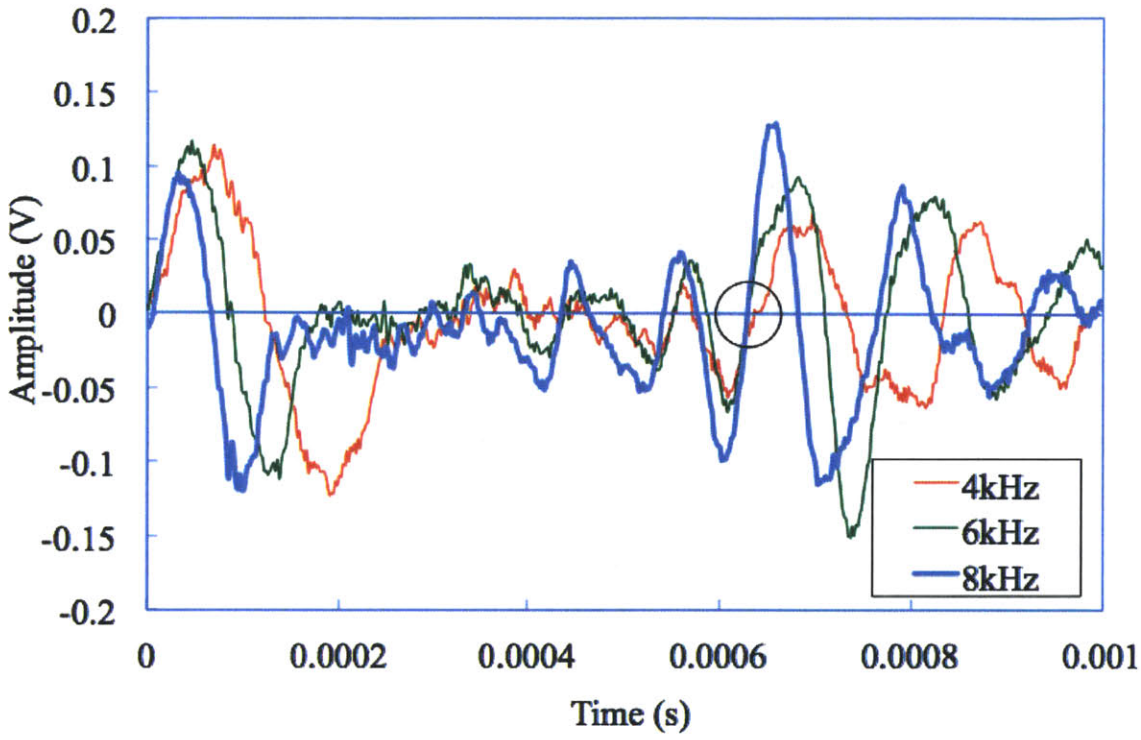

Figure 5-6: The frequency was varied for a saturated BBC specimen at 400kPa using bender elements. There is no discernible difference in arrival times, as seen in the circled region

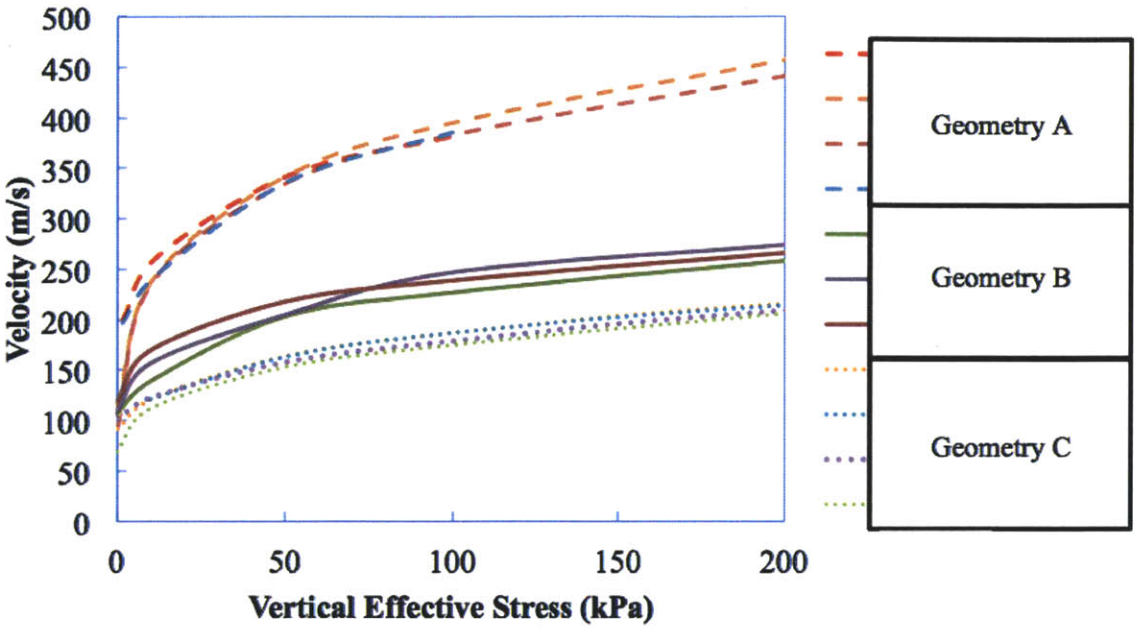

Figure 5-7: A parametric study of the bender element tip geometry shows that depending on the way the epoxy is deposited on the tip and the alignment of the tip, the results can vary by a factor of 2

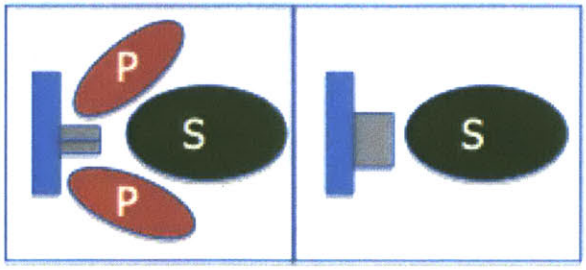

Figure 5-8: The deflecting bender element produces an orthogonally-propagating S-wave and in certain cases can also produce side-traveling P-waves

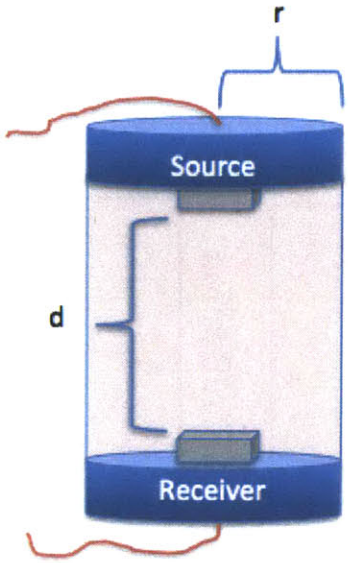

Figure 5-9: This schematic representation shows bender element endcaps on either side of a cylindrical specimen. The aspect ratio and wavelength ratio limits are based on these dimensions

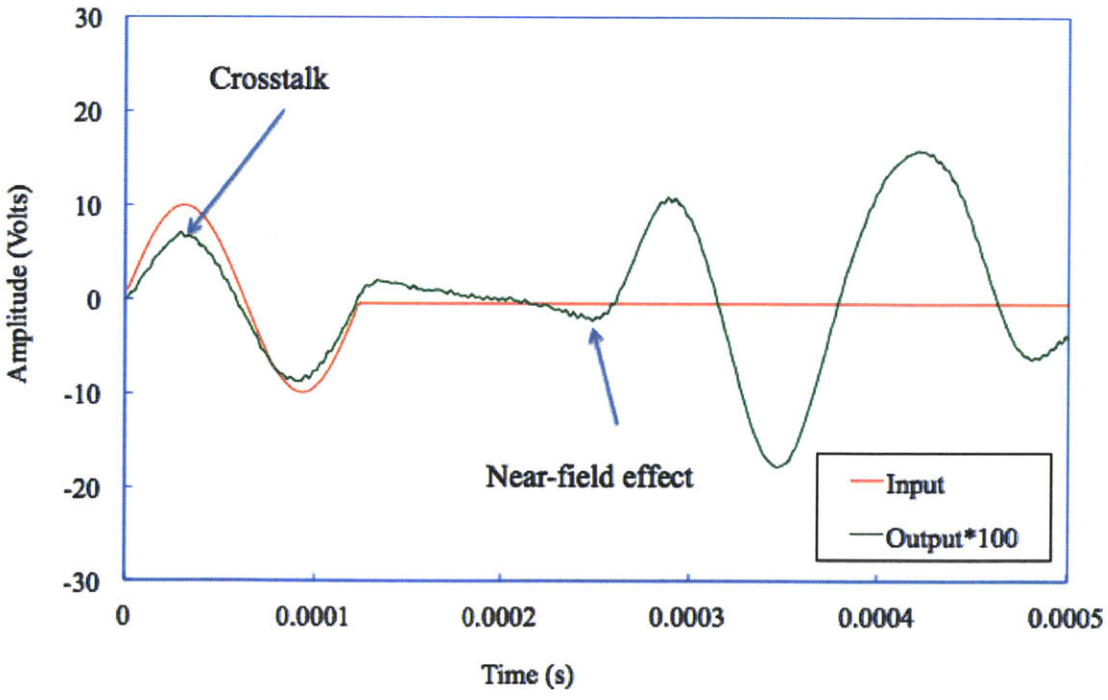

Figure 5-10: This signal obtained from an experiment on Ticino sand at 8kHz demonstrates the result of having a wavelength ratio lest than 2, where the near-field effect occurs. Additionally, this signal exhibits crosstalk, which is electrically induced when the bender elements are not electrically isolated

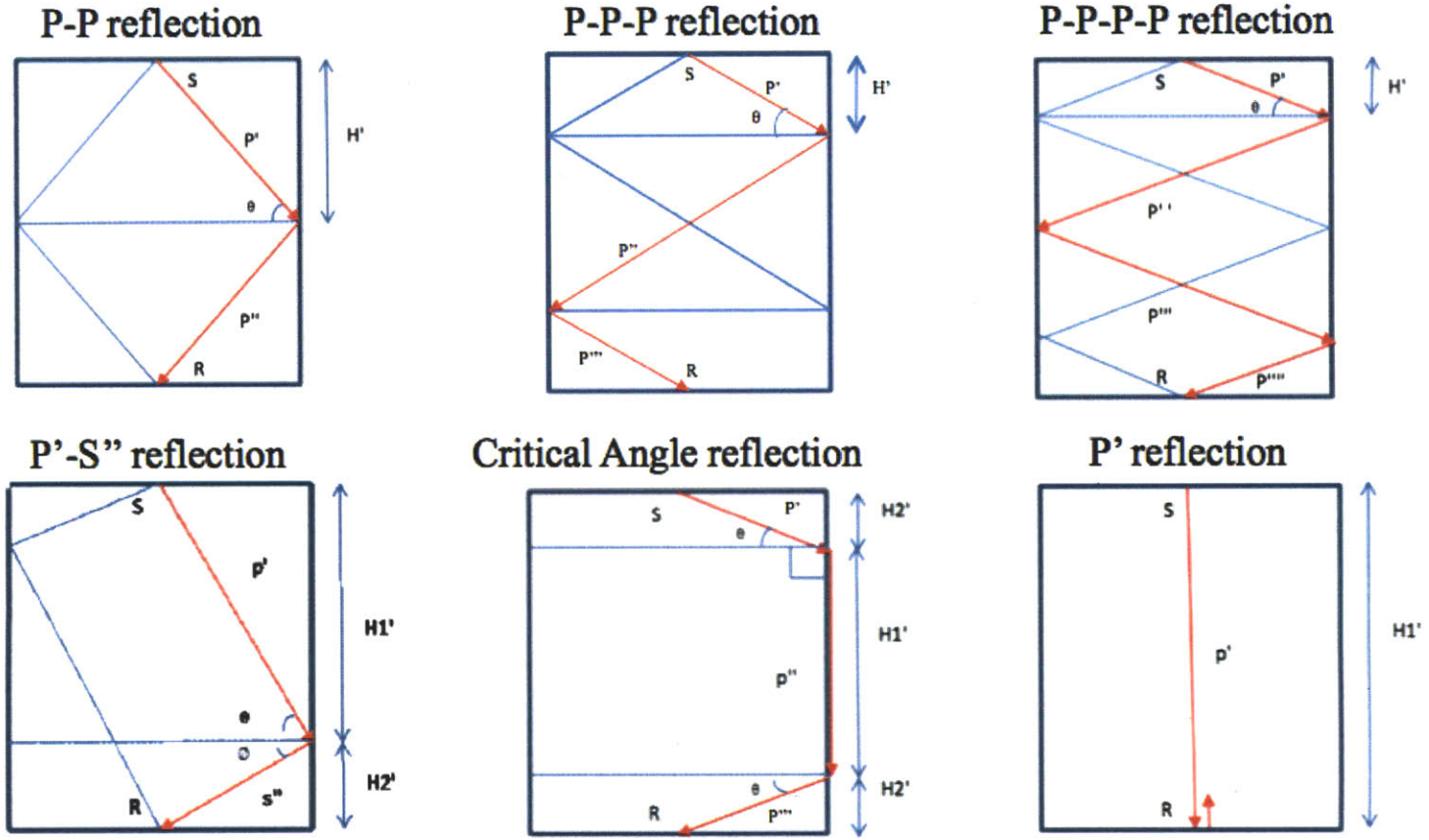

Figure 5-11: A ray path analysis was performed to evaluate the position of the various possible arrivals if a P or S wave were sent at the origin. Although this analysis assumes a perfectly elastic medium, it does provide insight into approximate arrivals to verify the possibility of signal interference (Adapted from [Johnson, 2011])

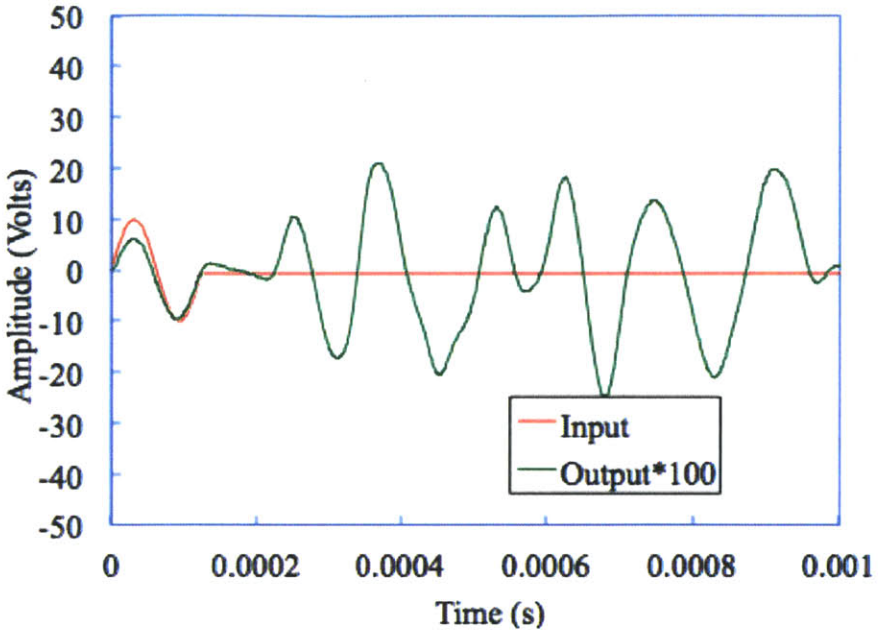

Figure 5-12: A small diameter is used with a d=8cm and r=3.75cm at a stress of 100kPa. As can be seen, the signal arrives very early and there are a lot of reflections. The likelihood that there boundary reflections is high and the signal does not have a distinct arrival

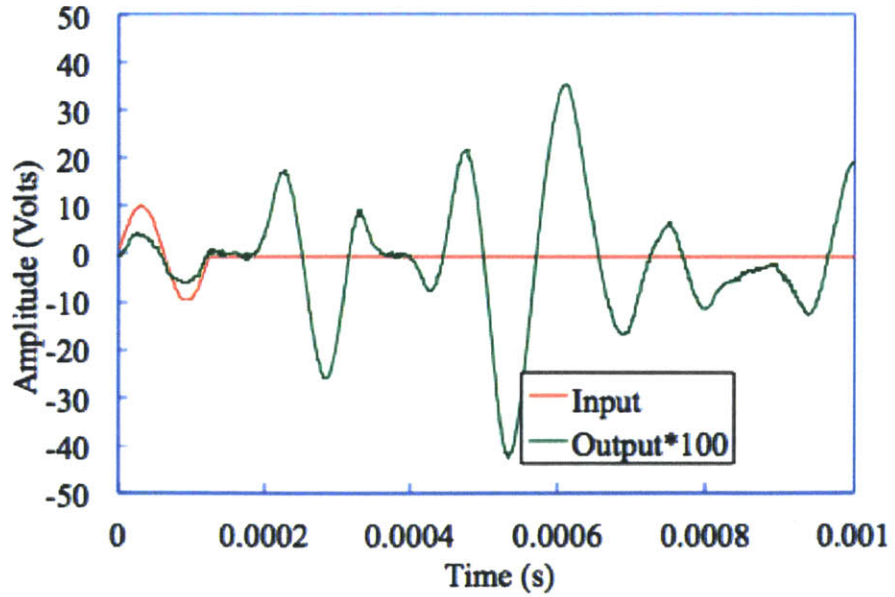

Figure 5-13: A medium diameter is used with a d=7.9cm and r=5.65cm at a stress of 88kPa. As can be seen, the signal arrives early but there are fewer reflections than in the previous case. It is more evident which signal is the arrival

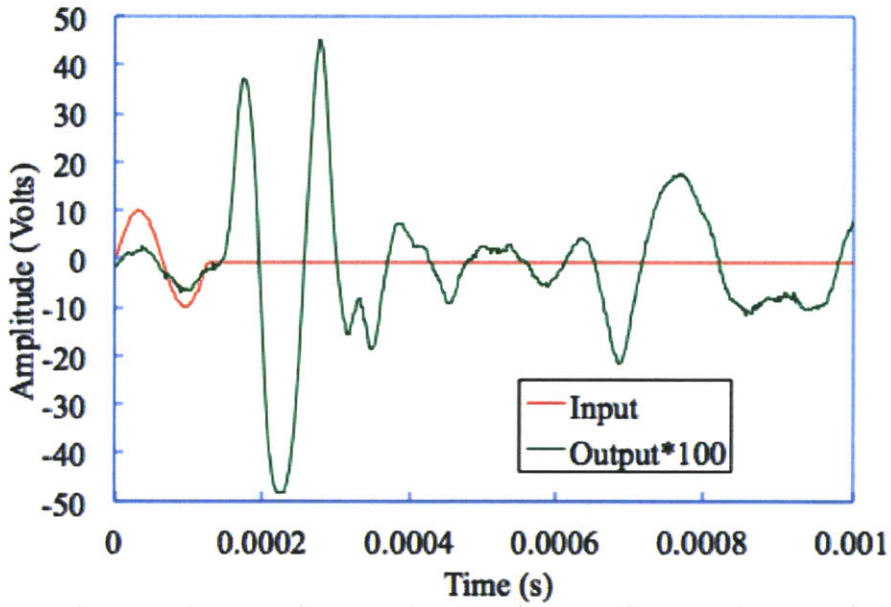

Figure 5-14: A small diameter is used with a d=7.6cm and r=10cm at a stress of 100kPa. As can be seen, the signal arrives very early but this time the signal is very distinct and there are far fewer boundary reflections and interferences. This allows for a more unambiguous selection of the arrival time

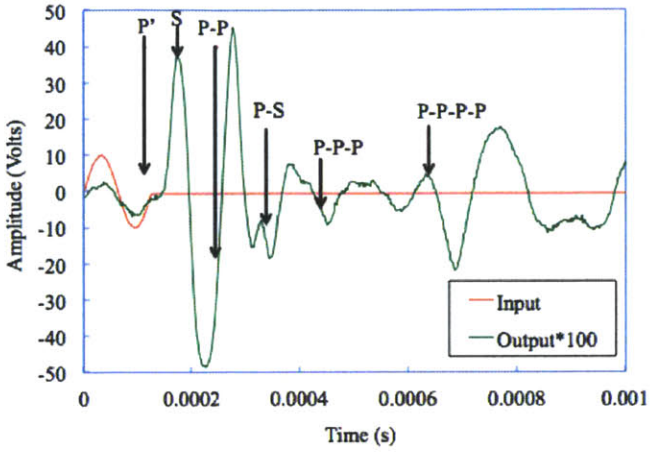

(a) Assuming first wave is S-wave

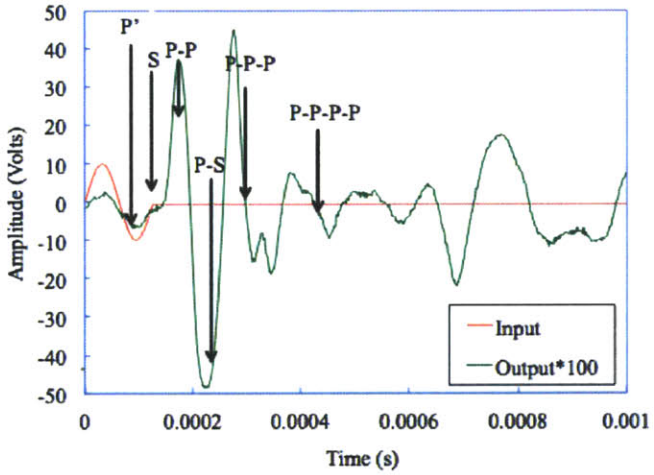

(b) Assuming first wave is P-P reflection

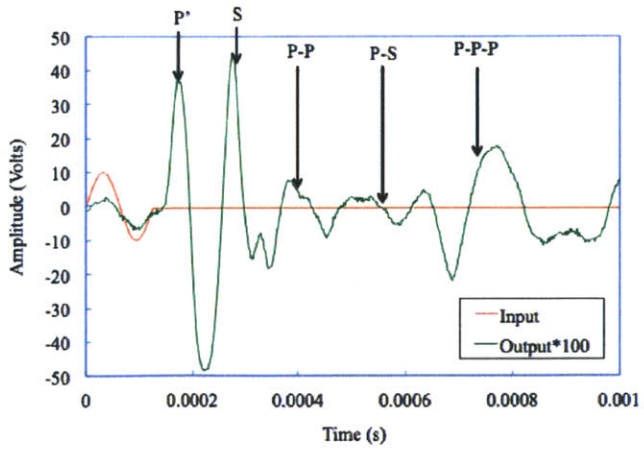

(c) Assuming first wave is direct P' wave

Figure 5-15: An extensive ray path analysis on Figure 5-14 provides more insight into the waves registered by the receiver bender element for Geometry A

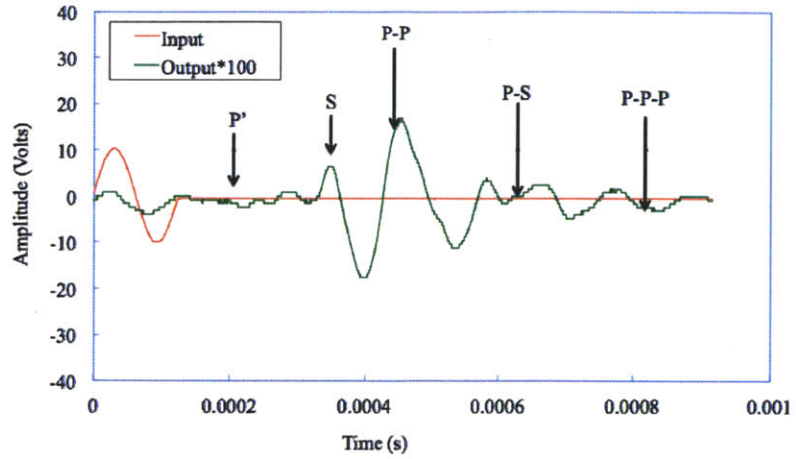

(a) Assuming first wave is S-wave

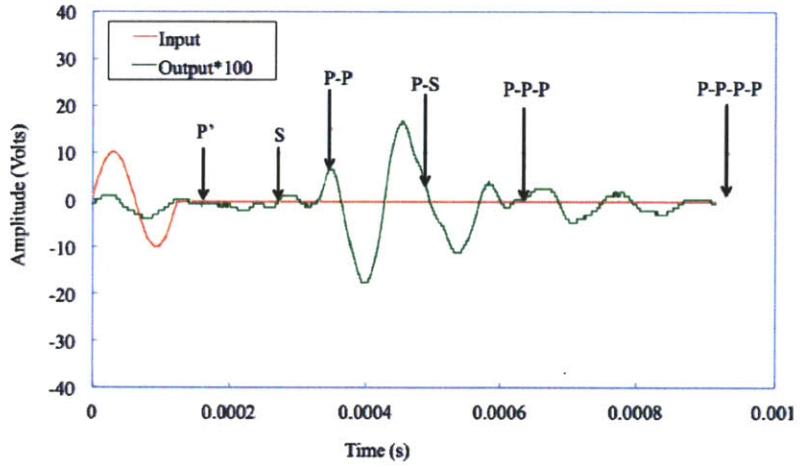

(b) Assuming first wave is P-P reflection

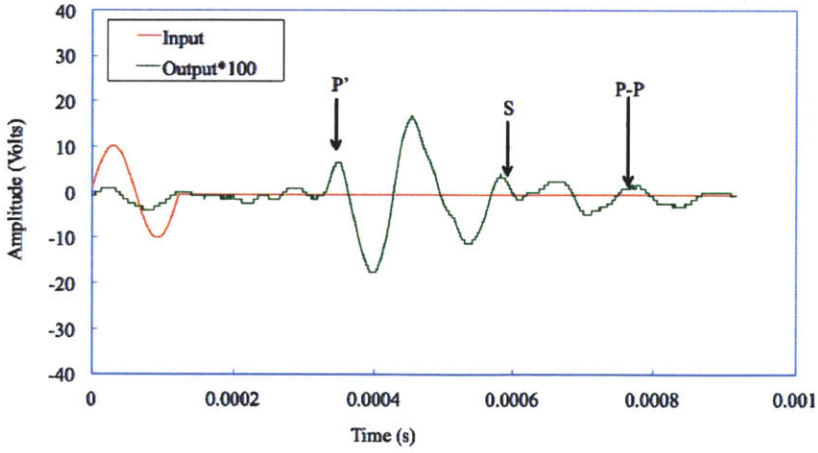

(c) Assuming first wave is direct P' wave

Figure 5-16: An extensive ray path analysis on Figure 5-14 provides more insight into the waves registered by the receiver bender element for Geometry B

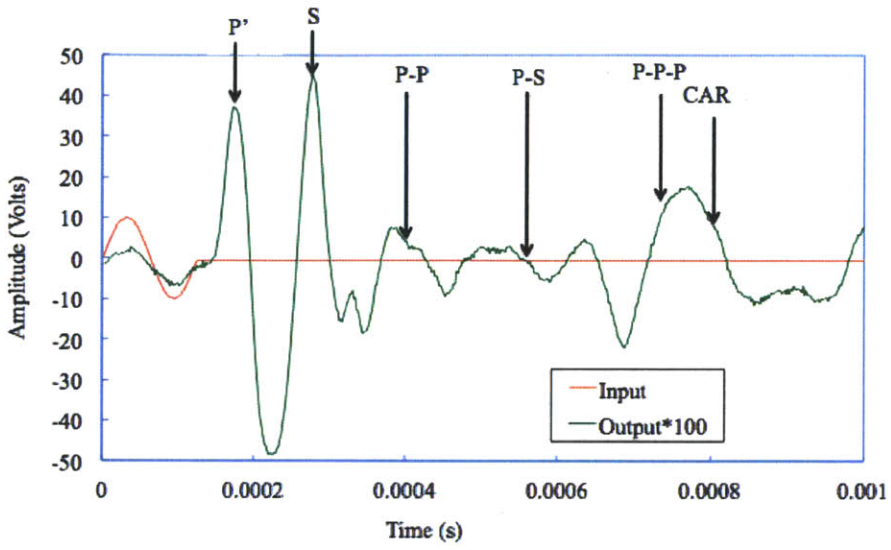

Figure 5-17: The arrival of the CAR was shown to not have an impact on the output signal due to its high attenuation. This image is for Geometry A assuming first arrival is P'

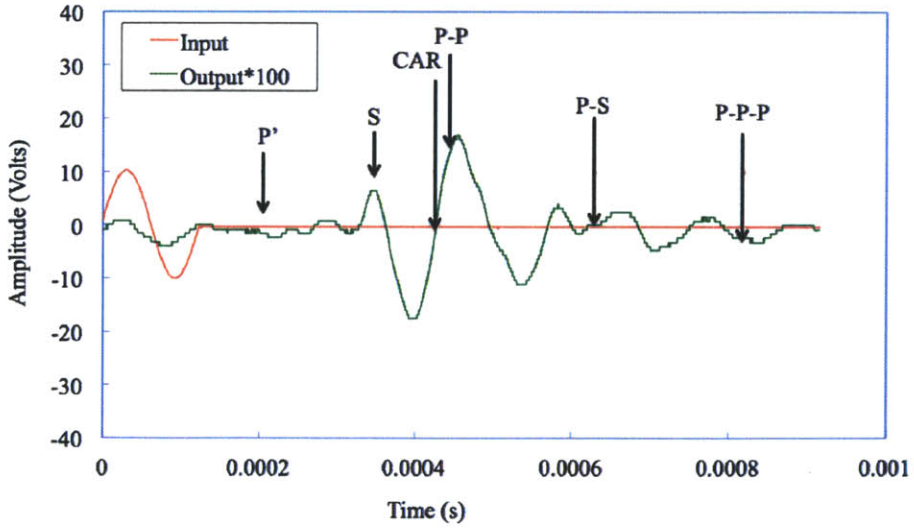

Figure 5-18: The arrival of the CAR was shown to not have an impact on the output signal due to its high attenuation. This image is for Geometry B assuming first arrival is S

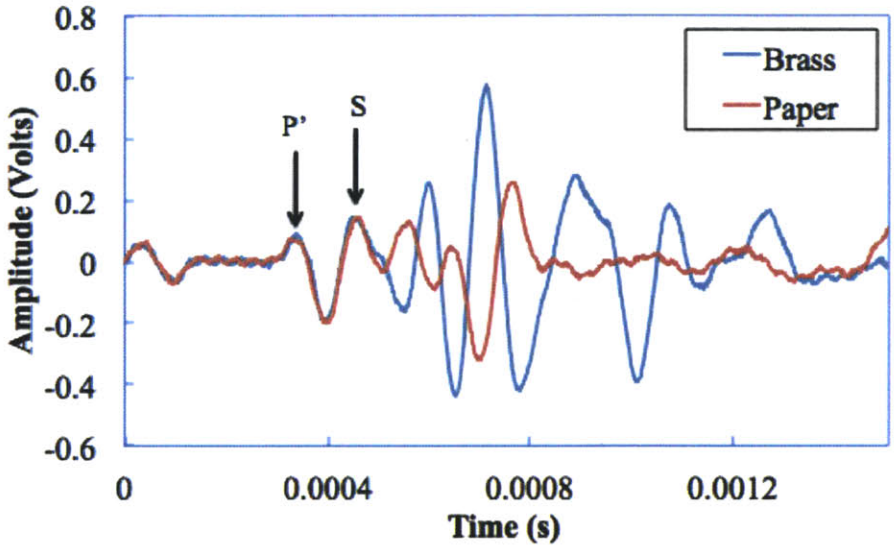

Figure 5-19: The same experiment was conducted on Ticino sand in a brass tube using Geometry A. In one case the inside of the tube was lined with paper, which simulated a soft boundary, while the other case was just the brass shell, which is considered a hard boundary. As can be seen here, after the arrival of the first wave, the subsequent waves flip in polarity, confirming that they are side-boundary reflections

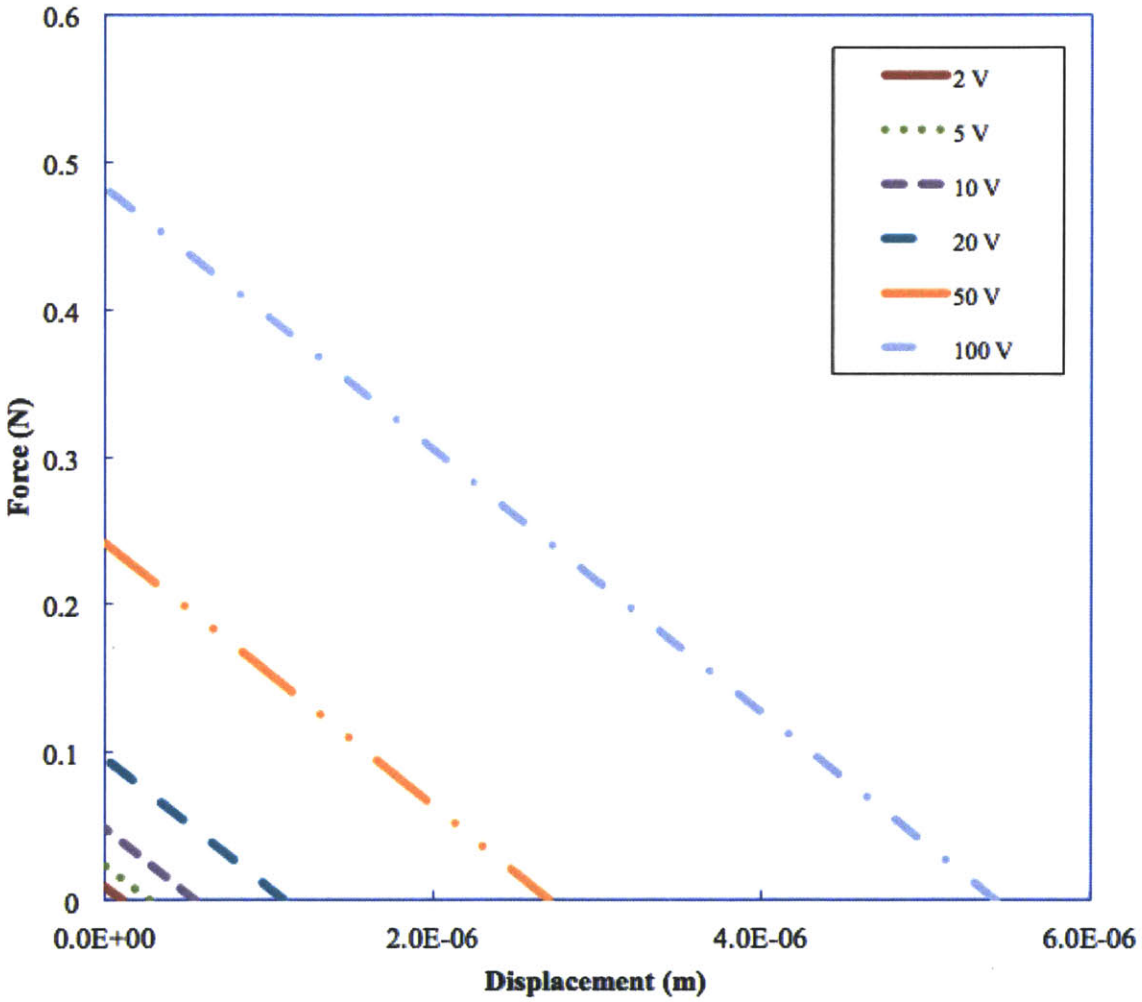

Figure 5-20: Relationship of displacement of the bender element tip versus lateral confining force as a function of various input voltages. This example is using Geometry B and the series configuration

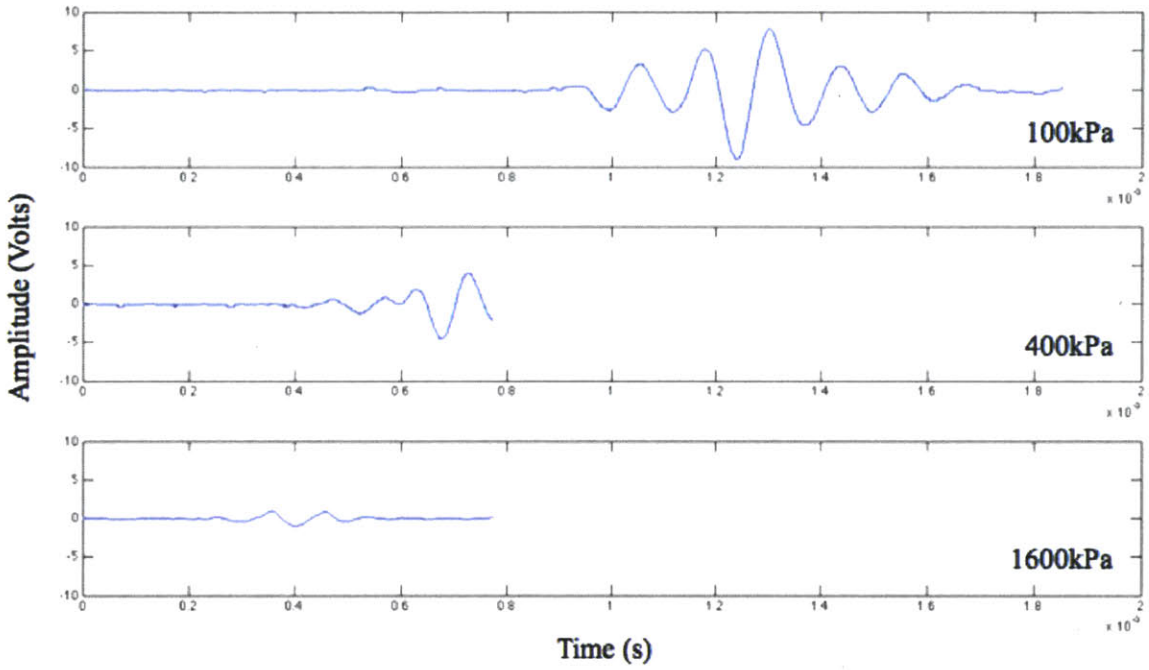

Figure 5-21: The amplitude of the output signal diminished with increased confining stress

Chapter 6

Data Analysis Methods

The data processing component of bender element testing has proven to be the largest challenge faced by new testing facilities. The dominant form of signal processing is the time domain method and manual selection of the arrival waves in the signal. While this remains the most-used method, as well as the method used in this research, there have been attempts at procuring a methodology that bypasses the manual selection component that can be tedious and user-dependent, such as the cross correlation method and the frequency domain method.

6.1 Arrival Time Selection

The three main types of analyses done on the output signal are time domain, cross-correlation, and frequency domain. The time domain can be further separated into two types of arrival selection: peak-to-peak or start-to-start. While this research does not experimentally investigate the effects that these data analysis methods have on the velocity results, this chapter provides an explanation and comparison of the various methods commonly used. This research has maintained the use of the start-to-start method due to the results seen in published papers as well as to avoid potential dispersion effects caused to the wave from the source to receiver, as will be discussed in the following sections.

6.1.1 Time Domain

The time domain method is the simplest to implement as far as computational capabilities; however, it can prove to be more difficult than the other methods due to the need for the user to manually decide which arrival to select. It is best performed by a researcher with experience at selecting the arrival time and with a knowledge of wave propagation principles as well as the mechanical behavior of the bender elements. Since the traces are time-averaged, the selection of the arrival time becomes even more unambiguous.

There are two primary ways in which the arrival time can be selected. The first is the start-to-start method, which is essentially self-descriptive. The travel time from the beginning of the input wave to the beginning of the output wave is taken. An example can be seen in Figure 6-1. The portion when the signal departs from 0V and begins to form a positive peak is where the travel-time ends. It is known that a positively trending signal is the arrival of the shear wave if the bender element tips are checked to see whether they are in phase with each other. This is accomplished by putting the two bender element tips to each other. It will be evident that in one orientation, the output signal will match the polarity of the input signal, whereas if the bender element is rotated 180°, the first output signal will be a negatively-polarized wave. Example results performed by [Asaka et al., 2008] using the start-to-start method are seen in Figure 6-2, where the input frequency was varied and the observed arrival time was monitored. It was evident that irrespective of the frequency, the starting point at which the signal arrives at the receiver remained constant. This highlights the frequency-independent benefit of the start-to-start method.

The second type of time domain travel time selection is the peak-to-peak method, also shown in Figure 6-1. This method is easier to visually detect in many cases, thus is chosen for the ease of identifying the maximum peak of the signal. One shortcoming of this system is the inability to account for dispersive effects that might widen the period of the output signal, as compared to the input signal. While it some cases it might be a negligible effect, in other cases, the dispersion could be considerable,

depending on the soil being tested. This is particularly a concern for sand, especially saturated sands. One can evaluate whether dispersion has occurred by measuring the period of the input wave versus the output wave to assess whether it is a concern.

6.1.2 Cross-Correlation

Since one of the uncertainties of interpreting velocity results for bender elements is the selection of arrival times, there have been a few attempts at eliminating the human-prone error in arrival time selection by using numerical methods of auto-selecting the arrival time. The cross-correlation method is based on a comparison of the input signal with the first positive output signal. The following equation is used during this analysis:

$$CC_{xy}(t_s) = \lim_{T\to\infty} \frac{1}{T} \int_0^T X(t)Y(t+t_s)dt \tag{6.1}$$

where T is the recording period, t_s is the time shift between the input and output, $X(t)$ is the time history of the input wave, and $Y(t)$ is the time history of the received wave. To obtain the cross correlation maximum value CC_{xy}, the fast Fourier transform (FFT) is taken of the $X(t)$, after which it is multiplied by the complex conjugate of $Y(t)$ and the inverse FFT is taken of the product. This maximum value CC_{xy} corresponds to the total travel time of the wave. A more detailed explanation can be found in [Viggiani and Atkinson, 1995].

One of the disadvantages of the cross correlation method is that it takes the first positive peak of the output to produce a travel time calculation. In some cases, there are precursory waves that present themselves in the output signal (i.e. caused by near-field effect or P-waves), which would not be recognized as such by the computational method of cross-correlation. Another shortcoming of the cross-correlation method is its dependence on the frequency of the signals. If the input signal frequency is different from the output signal frequency, errors will arise in the velocity calculations. Since this is sometimes the case when the bender elements are driven at frequencies higher than their natural resonant frequency, a careful check of the f_n needs to be performed to ensure that the input frequency matches the output frequency before

the CC method can be used. Another factor that can alter the output frequency is dispersion. Since this is a factor that one cannot control, the CC method can prove to be unreliable, depending on the dispersion characteristics of the soil being tested.

6.1.3 Frequency Domain

The frequency domain method of signal interpretation, also called the cross-spectrum method, is based on interpreting the phase of the signal. It decodes the relative phase of the input and output waves using Fourier transforms to separate out the signal into its harmonics. The phase (in radians) is plotted against frequency (in kHz) and the slope of a linear fit of this line is divided by 2π to produce the group travel time [Viggiani and Atkinson, 1995, Chan, 2010]. The phase can be obtained using a continuous sweep function and a spectrum analyzer [Ferreira et al., 2007]. Although the frequency domain method of selecting the arrival time reduces the user-bias associate with arrival selections, it still requires someone with expertise to perform post-processing verification of the experimental results. As opposed to the time domain method, which is continuously performed with the judgement of the user, thus readily identifying anomalous waveforms, the computer automated method of FD is more prone to overlooking such instanced that might greatly affect the subsequent outcome.

6.1.4 Comparison of Different Methods

There have been studies that compare results obtain using various velocity interpretations based on a single data set. One was performed by [Asaka et al., 2008] on Porto residual soil, where the cross correlation method and time domain method were utilized and compared, as seen in Figure 6-3. The solid markers indicate measurements using the TD method while hollow markers indicate CC. The results obtained from CC show much more variability than the hand-picked start-to-start method as a function of input frequency. This is likely due to the frequency effect on the cross correlation method, which takes into account the difference in frequency between the

input and output signal.

Another study conducted by [Chan, 2010] on cement-stabilized kaolin, which varied the input frequency and observed the velocity calculations for each of the above-specified methods. It can be seen that the visual picking method (start-to-start time domain method) produces the most consistent results with increasing frequency. As discussed in section 5.1, there should be no frequency effect on the calculation of the velocity results, given the specific frequency range. The high variability of the cross-spectrum method is likely caused by the fact that the output frequency will behave at the frequency of the input wave up until the natural resonant frequency, after which it will behave at the natural resonant frequency. Since the cross-spectrum method is based on the frequency of the output, which changes until it reaches f_n, the high level of variation is expected. Similarly, the cross-correlation is also affected by the change in frequency, as was also evidenced by the study peformed by [Asaka et al., 2008].

A comparison between the frequency domain (FD) and time domain (TD) start-to-start method can be seen in Figure 2-13, where [Ferreira et al., 2007] tested Porto residual soil. The difference between the two methods of signal analysis are shown to be minimal, mathematically described as shear modulus relations of $G_{TD} = 4.31p'^{0.624}$ versus $G_{FD} = 3.467p'^{0.658}$, where G is the shear modulus and p' is the mean effective stress. The FD results were shown to yield lower shear modulus values than TD methods. It is clear, however, that there is a higher amount of scatter in the FD results than observed in the TD results, likely indicating the FD sensitivity to dispersive effects.

6.2 Square versus Sinusoidal Wave Input

When using a function generator, there are multiple types of input waves that can be selected, including the square, sinusoidal, ramp, and triangle waveforms. For bender element testing, the sinusoidal wave is the most commonly used, followed by the square wave. For ultrasonic transducers, a square wave is used. The primary differ-

ence between ultrasonic transducer and bender elements is that ultrasonic transducer are driven by a pulse, while bender elements are driven by a frequency at or below their natural resonant frequency (f_n).

6.2.1 Bender Elements

While most of the research conducted on bender elements, including this research, use sinusoidal waveforms, there have been some studies that investigated the use of square waves. The reason for the widespread use of sinusoidal waves is because they make the bender element behave in a harmonic fashion, which is conducive to controlling the output signal. When the harmonic motion is used to excite the bender element, the bender element tip reacts in the same harmonic motion, creating a shear wave, as long as the input frequency is at or below the natural resonant frequency (f_n). When a square wave is used, a spectrum of frequencies is sent through the specimen rather than simply one input signal at one particular frequency, which prevents the user from controlling the properties of the wave sent through the specimen. This also makes the data analysis methods of cross correlation and frequency domain impossible. With a sinusoidal wave, all the options are still viable. An example of a signal obtained using a square wave can be seen in an experiment performed by [Jovicic et al., 1996] in Figure 6-5. The x-axis of this graph is normalized by the true arrival of the shear wave. The interpretation of the received wave becomes difficult as the quality of the signal is much more degraded as compared to sinusoidal input waves.

6.2.2 Ultrasonic Transducer

Ultrasonic transducers are excited using pulser systems that have high signal amplitudes of around 100V. Additionally, they usually run at high frequencies on the order of 1MHz. Equipment that has the capacity to drive a high voltage, high frequency signal usually only has one output waveform, which can most aptly be described as a square pulse wave that creates a positive square, without a negative component. The square wave used to excite the ultrasonic transducers in this research can also be

described as a burst that lasts for a duration of 1/f where f=0.65MHz. Most arbitrary function generators run on Direct Digital Synthesis (DDS), which cannot easily run at 1MHz and 100V, since this usually exceeds the capacity of the digital counting techniques used to create the various waveforms. Thus the use of a square wave is the singular option. In addition, at these magnitudes, the waveform becomes irrelevant since the device is no longer sensitive to the type of wave.

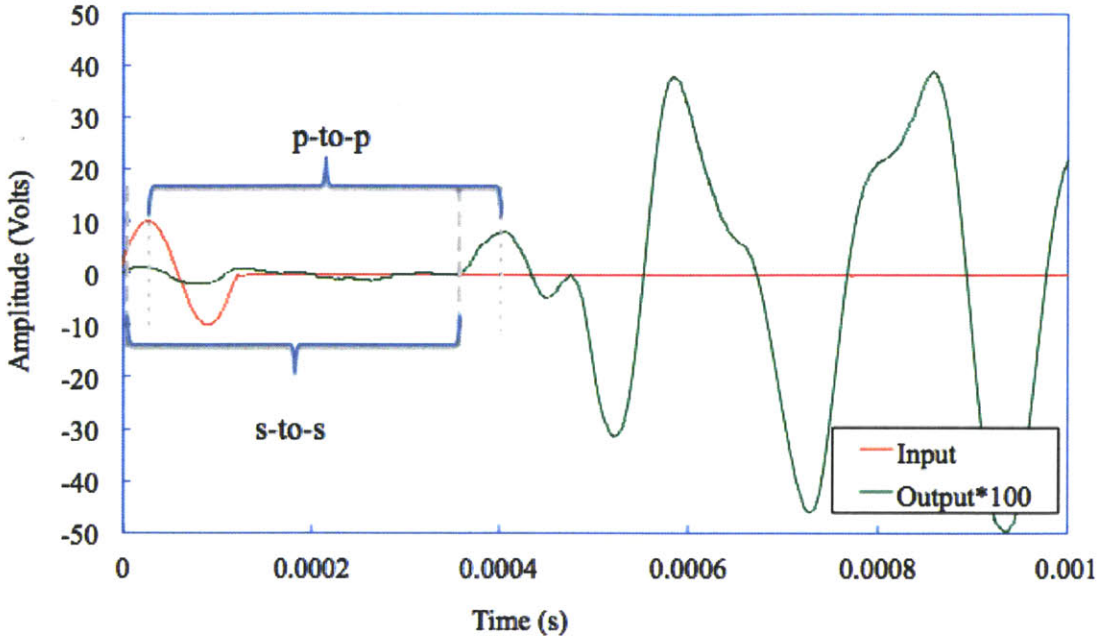

Figure 6-1: This is an example of the time domain method of obtaining the travel time. The start-to-start and peak-to-peak methods are depicted in the figure

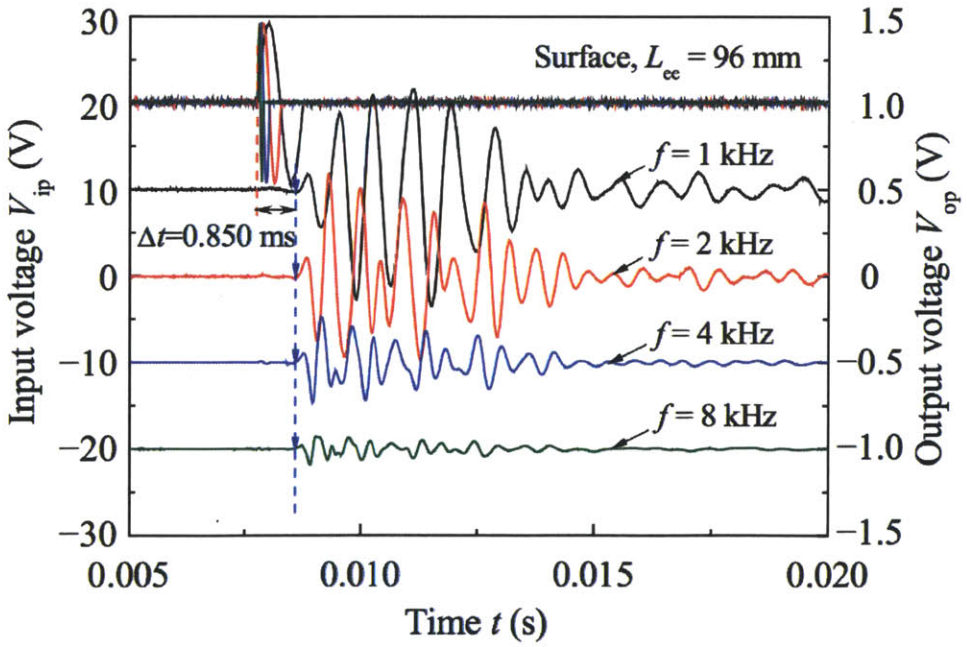

Figure 6-2: Changing the input frequency has shown to have no effect on the arrival time detection when using the start-to-start method for bender element testing on silica sand [Asaka et al., 2008]

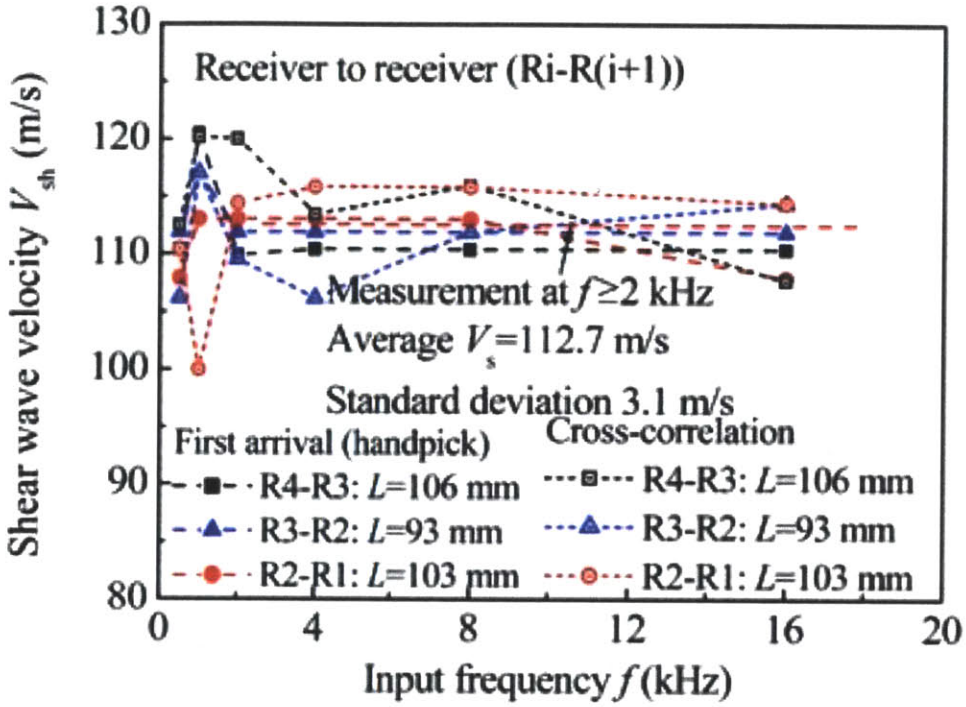

Figure 6-3: The solid markers indicate measurements using the TD method while hollow markers indicate CC. The results obtained from CC show much more variability than the hand-picked start-to-start method [Asaka et al., 2008]

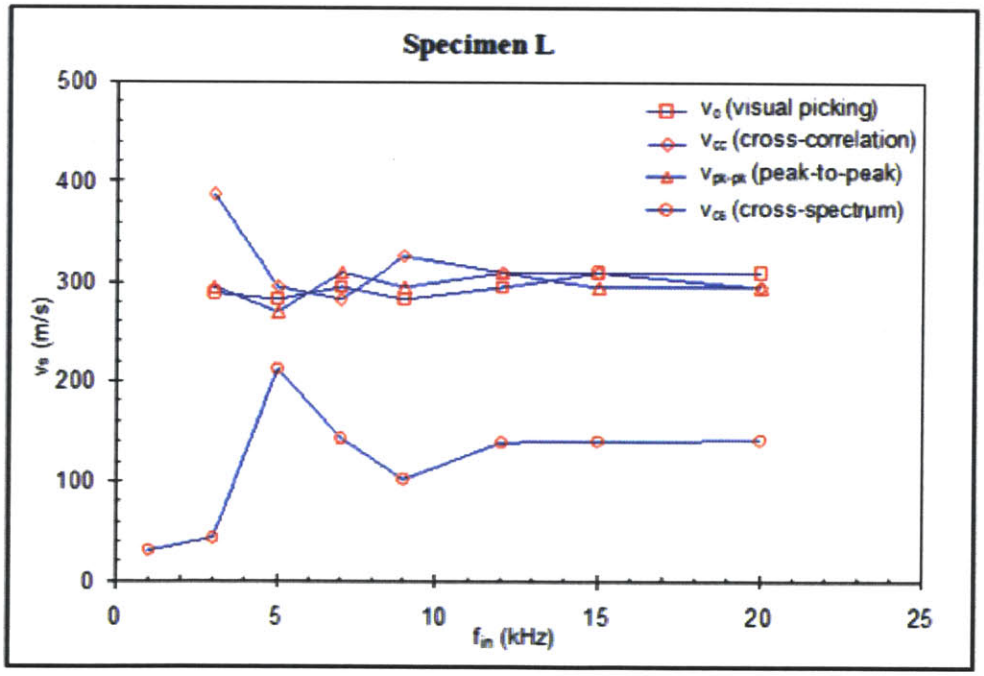

Figure 6-4: As seen in this figure, visually picking has the least variability as a function of input frequency, whereas the other methods are influenced by the frequency change [Chan, 2010]

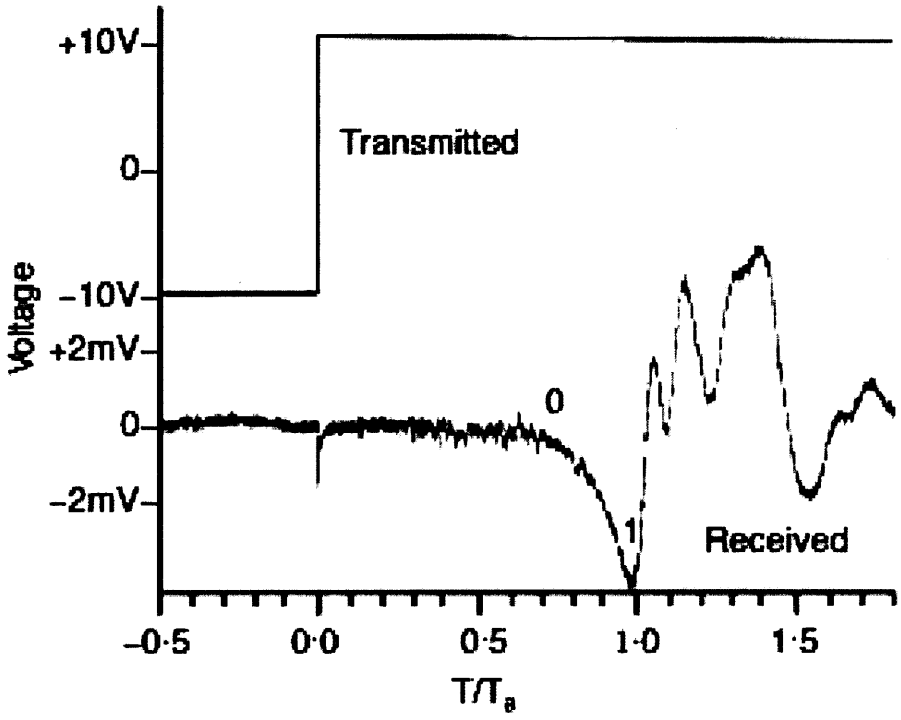

Figure 6-5: A square wave used during bender element testing for the input signal creates a received signal of degraded quality. It becomes difficult to determine whether to select the arrival time at the point labeled 0 or 1 [Jovicic et al., 1996]

Chapter 7

Results and Discussion

Numerous experiments were performed on both BBC and Ticino sand to verify the behavior of the equipment and compile propagation velocities for different conditions. An extensive list of bender element experiments run at the MIT Geotechnical Laboratory can be seen in Tables 7.1 to 7.3. The aim of the experimentation was twofold: a) establish a set of defining parameters that enable the consistent, reliable measurement of the shear modulus of soil using the available bender elements as well as criteria to be followed when using new bender elements, and b) gather measurements of shear velocity in BBC and relate it to the loading pattern during the experimentation. The first goal was achieved through the testing of Ticino sand and was successfully compared to published results. The second goal was accomplished to a capacity that included the loading and unloading cycles that allowed for the development of a relationship between the stress state and the shear modulus of the specimen.

The results from part a) are presented in section 7.1, while the results from experiments conducted on BBC are presented ins section 7.2. Furthermore, some key observations on the anisotropy present in BBC as well as the testing variability present in results depending on mode of experimentation are addressed.

Table 7.1: List of experiments conducted using bender elements. TS=Ticino sand. Comment field left blank if setup consisted of brass tube and no lining

Test ID	Material	BE Geometry	Max. Stress (kPa)	G_s	Saturation (%)	Initial d (cm)	Final d (cm)	Initial Bulk Density (g/cm^3)	Initial Void Ratio, e	Final Void Ratio, e	Comments
BE002	TS	A	205	2.68	0	31.55	31.51	1.46	0.83	0.83	
BE003	TS	A	583	2.68	0	33.14	32.89	1.44	0.85	0.85	
BE004	TS	A	558	2.68	0	20.94	20.49	1.52	0.79	0.76	
BE005	TS	A	200	2.68	0	2.064	2.022	-	-	-	Very Short
BE006	TS	A	200	2.68	0	7.49	7.34	1.5	0.69	0.67	2kHz
BE007	TS	A	200	2.68	0	7.44	7.24	1.51	0.76	0.74	2kHz
BE008	TS	A	5	2.68	0	7.34	7.29	1.53	0.75	0.74	Rotating top cap 360°
BE009	TS	A	200	2.68	0	7.34	7.14	1.53	0.75	0.72	
BE010	TS	A	200	2.68	0	7.49	7.24	1.51	0.77	0.74	Paper liner
BE011	TS	B	200	2.68	0	9.14	8.99	1.54	0.74	0.72	
BE012	TS	B	200	2.68	0	9.44	9.14	1.5 0	0.79	0.75	Paper liner
BE013	TS	A	200	2.68	0	8.24	7.94	1.78	0.50	0.47	Cardboard endcap liner
BE014	TS	A	200	2.68	0	8.24	7.74	-	-	-	Styrofoam spacer
BE015	TS	A	200	2.68	0	8.24	7.99	1.54	0.73	0.70	Paper liner, cardboar endcap liner
BE016	TS	A	88	2.68	0	5.81	-	-	-	-	Wider diameter (11.3cm)
BE018	TS	A	88	2.68	0	8.8	8.67	1.53	0.74	0.74	Wider diameter (11.3cm)
BE019	TS	A	88	2.68	0	7.93	7.885	1.53	0.75	0.75	Wider diameter (11.3cm)
BE020	TS	A	88	2.68	0	8.33	8.08	1.47	0.82	0.81	Wider diameter (11.3cm), paper liner

Table 7.2: List of experiments conducted using bender elements. TS=Ticino sand. Comment field left blank if setup consisted of brass tube and no lining

Test ID	Material	BE Geometry	Max. Stress (kPa)	G_s	Saturation (%)	Initial d (cm)	Final d (cm)	Initial Bulk Density (g/cm^3)	Initial Void Ratio, e	Final Void Ratio, e	Comments
BE021	TS	A	100	2.68	0	7.66	7.565	1.6	0.66	0.67	Wider diameter (20cm)
BE022	TS	A	200	2.68	0	7.14	7.06	1.55	0.73	0.71	Paper liner
BE023	TS	B	600	2.68	0	7.54	7.14	1.47	0.83	0.76	Plastic liner
BE024	TS	B	200	2.68	0	7.016	6.966	1.48	0.81	0.79	Paper liner
BE025	TS	A	600	2.68	0	9.12	8.6	1.49	0.80	0.71	Plastic liner
BE026	TS	A	102	2.68	0	6.64	6.54	1.42	0.89	0.88	Wider diameter (20cm) with springs
BE027	TS	A	200	2.68	0	7.34	7.04	1.41	0.90	0.85	
BE028	TS	A	200	2.68	0	7.19	7.02	1.43	0.88	0.85	Paper liner
BE030	TS	A	102	2.68	0	9.307	9.187	1.52	0.76	0.76	Wider diameter (11.3cm) with springs
BE031	TS	A	102	2.68	0	9.69	9.5	1.53	0.75	0.74	Wider diameter (11.3cm) with springs
BE032	TS	B	200	2.68	0	22.91	22.71	1.42	0.88	0.86	Long tube
BE033	BBC	A	800	2.78	86	9.54	8.7	1.75	1.08	0.91	OCR=1.8
BE034	TS	B	200	2.68	0	9.44	9.25	1.58	0.69	0.68	Wider diameter (11.3cm) with springs
BE035	TS	C	200	2.68	0	7.88	7.73	1.47	0.83	0.80	Paper liner
BE036	TS	C	400	2.68	0	7.87	7.67	-	-	-	Paper liner
BE037	TS	A,B	400	2.68	0	8.54	8.49	1.56	0.72	0.71	A sender, B receiver
BE038	TS	A,B	400	2.68	0	8.64	8.49	1.56	0.71	0.69	B sender, A receiver
BE039	TS	C	200	2.68	0	7.92	7.76	1.55	0.73	0.70	

Table 7.3: List of experiments conducted using bender elements. TS=Ticino sand. Comment field left blank if setup consisted of brass tube and no lining

Test ID	Material	BE Geometry	Max. Stress (kPa)	G_s	Saturation (%)	Initial d (cm)	Final d (cm)	Initial Bulk Density (g/cm^3)	Initial Void Ratio, e	Final Void Ratio, e	Comments
BE040	TS	B	200	2.68	0	9.31	9.21	1.57	0.70	0.68	
BE041	TS	C	200	2.68	0	7.8	7.65	1.57	0.70	0.68	Geometry C epoxy shaved
BE042	TS	C	200	2.68	0	7.76	7.68	1.56	0.71	0.70	Geometry C epoxy shaved
BE043	BBC	B	900	2.78	-	9.47	8.47	1.96	0.98	0.88	OCR=1.8
BE044	RBBC	B	1600	2.78	98.3	10.17	6.89	1.97	0.86	0.81	OCR=1, acrylic tube
BE045	RBBC	B	1600	2.78	100	13.85	10.71	1.98	1.31	0.77	RS217, OCR=1, acrylic tube
BE046	RBBC	B	1600	2.78	95.4	14.08	9.731	1.96	1.64	0.81	RS224, OCR=1, acrylic tube
BE047	RBBC	B	1600	2.78	97	12.98	10.04	1.99	1.31	0.77	RS221, OCR=1, acrylic tube
BE048	TS	B	200	2.68	0	9.5	9.19	1.37	0.95	0.90	
BE049	TS	B	100	2.68	0	14.85	14.75	1.5	0.79	0.78	Wider diameter (11.3cm) with springs
BE050	TS	B	100	2.68	0	9.48	9.04	1.69	0.58	0.57	Wider diameter (20cm) with springs

7.1 Ticino Sand Results

The first series of experiments was performed on Ticino sand. This material was chosen for its ease of preparation and the ability to do many tests in a relatively short time span. In addition, the results were compared with published data to observe how bender elements used in this research relate to other published results.

7.1.1 Ticino Sand Velocity and G_{max} measurements

During the testing of Ticino sand, multiple bender element geometries were used as well as different lateral boundary conditions. Refer to Tables 7.1 to 7.3 for exact descriptions of particular experiments. As discussed in section 5.3, the specimen boundary effects were investigated to assess the optimal experimental setup conditions for the use of bender elements. During this process, wider cylindrical setups were explored. The first set of results pertaining to this stage can be seen in Figure 7-1.

When shifting to a wider setup of up to a large diameter of 20 cm, the velocity results shifted up, as seen in Figure 7-1. These experiments were conducted with 7.5 cm diameter acrylic endcaps that were placed in the middle with a wooden board placed at the surface of either end of the metal tube to restrain the sand and apply the load. It should be noted that this stage of experimentation occurred before the transition to Geometry B bender element tips, thus the results will have higher velocities. The results are still valid in the aim to compare the behavior as wider geometries are adopted. Returning back to the results in Figure 7-1, the shifting of the velocity curve upward as the diameter increased was attributed to the preferential loading of the middle section of the specimen. Since the load was applied on the small acrylic endcap, which was attempting to transfer a portion of the load with a thin piece of plywood along the horizontal surface of the specimen, the core of the specimen was exhibiting much higher stresses than the rest of the specimen. During the calculations of the Vertical Effective Stress, the applied load was taken over the entire area of the specimen, thus averaging the stress within the entire specimen. The velocity measurements for that data point were governed by the high-stress core, thus

skewing the velocity curve. To verify this explanation of the results, experiments were conducted using a spring loading system that would equally apply load to the outer periphery of the cylindrical specimen, seen in Figure 4-7. With the newly distributed load, the results converged, as seen in Figure 7-2.

The next stage in verifying the repeatability of testing procedures, various specimen heights were chosen to observe whether the travel times appropriately changed to yield consistent velocity measurements. As can be seen in Figure 7-3, even with varying lengths d, the velocity curves proved to be extremely consistent. These results were conducted using Geometry A bender elements, which would produce velocities higher than those of the shear velocity expected in Ticino sand, likely caused by direct P-waves as discussed in section 5.3. The next graph (Figure 7-4) shows the same comparison, but this time using bender element Geometry B. The results from Geometry B do not have the same level of repeatability as did Geometry A. This can be attributed by the fact that the setup with Geometry A was more stable than that of B. The bottom acrylic endcap for A has a lip that allowed the brass tube to rest directly on the endcap, preventing the extrusion of sand out the sides. Being able to more aptly restrain the sand from extruding out the sides allowed for a more precise estimation of the height and density of the specimen, as well as the alignment of the bender element tips. Moreover, the higher consistency with Geometry A might be attributed to the propagation of P-waves through the specimen, which usually have a lower percentage of error than S-waves [Piane et al., 2011]. Besides these two factors, the results seen in Figure 7-4 are relatively consistent with an overall error band of less than $\pm 7\%$.

The results found in Figure 7-4 will be further analyzed since the Geometry B provides reliable results of the desired shear wave velocity. The velocity results were used to obtain the shear modulus curves seen in Figure 7-5. As mentioned above, there is a likelihood that the density calculations are prone to error due to the extrusion of sand. This fact is evident in Figure 7-5 where the error band has increased to $\pm 23\%$ due to both multiplication of the velocity term as well as density variability.

7.1.2 Comparison with Published Data

To put the scatter in the G_{max} into better perspective, the shear modulus results are compared to other experiments conducted on Ticino sand. The shear modulus results obtained with Geometry B are compared to two published sources: [Fioravante and Capoferri, 2001] and [Pestana-Nascimento, 1994], as well as Geometry A for reference. The Geometry A results were included to once again reiterate the fact that this bender element geometry produced much higher velocities that correspond to P-waves rather than S-waves.

Fioravante, as mentioned previously in this paper, conducted bender element testing on Ticino sand. The shear modulus curve obtained from Fioravante is based on individual data points, as are the curves from this research. The results agree very favorably, as seen in Figure 7-6.

The next shear modulus curve was obtained from an empirical relation developed by Pestana. The relation was based on a large database of shear modulus results for Ticino sand, mostly comprised of resonant column tests. The equation is as follows:

$$(G_{max}/p_a)n = \frac{3}{2}C_b\frac{(1-2\mu')}{(1+\mu')}(\sigma'/p_a)^{1/3} \tag{7.1}$$

where p_a is the atmospheric pressure, n is the porosity, σ' is the mean effective stress, while C_b and μ' are experimentally derived constants. An average $n = 0.426$ was used in the calculations, with $p_a = 101kPa$. C_b and μ' range from 600-975 and 0.2-0.3 respectively. The mean effective stress is defined as follows:

$$\sigma' = \frac{1}{3}(\sigma'_v + 2\sigma'_h) \tag{7.2}$$

where σ'_h is calculated assuming $K_0 = 0.5$, meaning $\sigma'_h/\sigma'_v = 0.5$, thus yielding the following relation:

$$\sigma' = \frac{2}{3}\sigma'_v \tag{7.3}$$

Using equation 7.1 and converting the mean effective stress to vertical effective stress, the corresponding curve is obtained in Figure 7-6. Once again, the results match up

very well with each other, thus showing the reliability of the results obtained during this research with both published bender element results as well as results obtained from different methods. A closer look at the comparison between the published results and the results from this research can be seen in Figure 7-7, where all the shear modulus experimental data from from this research was combined with a polynomial fit for clarity.

7.2 Boston Blue Clay

7.2.1 Compression Behavior

As prescribed in previous chapters, BBC was tested in either thin-walled sample tubes (the same ones which were used to collect the intact samples), or acrylic consolidation tubes used for resedimentation. All the compiled compression curves can be seen in Figure 7-8 and 7-9, with labels referring to the test id and material tested, as can be seen in Table 7.1-7.3. Figure 7-8 is in e-σ'_v space, while Figure 7-9 is shown in e-logσ'_v space. As is evident, the RBBC specimens that were resedimented to an stress of 50kPa (BE044, BE046) start at approximately the same void ratio and follow similar compression curves, while the specimens resedimented to 100kPa (BE045, BE047) start at a lower void ratio but eventually converge with the other RBBC specimens. The tube specimens of natural BBC start at much lower void ratios but also eventually converge with the RBBC specimens. BE047 is shifted slightly below the other curves, likely indicating that some extrusion occurred. The unloading portions are also seen in the figure, which indicates when load was reduced and the specimens were allowed to swell. The unloading portion will be examined more carefully in section 7.2.4. The repeatability of the curves agrees very well considering the frequency of data points and the setup conditions. As compared to triaxial cell measurements that have a higher degree of control than the resedimentation tubes used for these experiments, the results align very closely.

The first specimens tested were natural samples of BBC. The tube specimens were

cut directly with the tube, with the surface on both sides extracted via hand scraper to create a recess for the bender element endcaps. A wire was run around the inside perimeter of the tube between the clay and the brass to relieve the adhesion of the clay on the inner surface of the brass tube. This was only done for the second tube specimen (BE043) and not the first test (BE033), which made the measurements before the breakthrough not representative of consolidation behavior. Since consolidation cannot fully occur until the clay breaks free from the side walls, the beginning portion, up until around 500kPa, may show underestimations of stress levels as well as lower amount of vertical deformation.

7.2.2 In situ v. Resedimented Behavior

A comparison of the velocity behaviors for the two tube BBC specimens versus a resedimented specimen (RBBC) is shown in Figure 7-10. As can be seen, the initial portion for the BBC has a much higher velocity since it begins in an overconsolidated state; however, when it reaches its preconsolidation pressure of 450kPa, it enters the normally consolidated region and begins to follow a similar trend to the resedimented specimen. The eventual slope of BE043 matches up with the normally consolidated RBBC, whereas the BE033 line plateaus, which implies there was likely error in the experiment or data processing.

Further comparison was conducted on the velocity curves that included all tests performed during this research on BBC. The complete graph of velocity curves including the unloading portion can be seen in Figure 7-11. The results indicate a curved logarithmic trend in linear space for velocity versus vertical effective stress. The unloading portions tend to have a decreased slope as compared to the normally consolidated region. Some unloading portions also exhibit slight curving downwards, which is not evident in the e-σ'_v plot, thus indicating a velocity effect. While the natural BBC specimens do not align very well with the normally consolidated specimens in this graph, they were left in for reference. In a different setup, with the elimination of the adhesion to the side walls, they might align better than at present, although, the difference could also be a function of the composition of the specimens.

The unloading portions for RBBC seen in Figure 7-11 introduce some scatter in the results, however, when taken out, the resulting velocity curves show good agreement, as seen in Figure 7-12.

7.2.3 Comparison with Published Data

In order to verify the results with published data, the velocity curves were transformed into shear modulus curves, using Equation 2.1. Since there is a squared factor in the relation, the differences between the respective velocity curves are expected to be amplified to an extent, as can be seen in Figure 7-13 as compared to Figure 7-12. There has not been an extensive amount of testing performed on clay, especially BBC, with respect to shear modulus values. Hence [Santagata, 1998] was considered a reliable source that performed Young's modulus measurements on RBBC, and more specifically used the same Series IV batch material to resediment her specimens. [Santagata, 1998] developed a correlation for the elastic modulus of a specimen as a function of void ratio and vertical consolidation stress (σ'_{vc}). The equation can be seen as follows:

$$E_{uMAX} = 270e^{-2.45}(\sigma'_{vc})^{0.43}(MPa) \tag{7.4}$$

where e is the void ratio and σ'_{vc} is the vertical consolidation stress in MPa. This captures the behavior of the loading portion only, and the unloading portion will be discussed in section 7.2.4. Note that this equation hold for undrained conditions.

Since [Santagata, 1998] developed a correlation to calculate the elastic modulus, it had to be converted to the shear modulus to compare with the results from this research. Assuming undrained conditions ($\mu = 0.5$), Equation 2.5 can be used to calculate the shear modulus. The results are plotted in Figure 7-15, showing both the E_{uMAX} and G_{max} from [Santagata, 1998], as well as the G_{max} results obtained during this research. As can be seen, the results compare relatively well, with the bender element results yielding higher stiffness results than those obtained by [Santagata, 1998] using mechanical deformation measurements. This can be explained by the strain-softening theory discussed in section 2.6, causing an underestimation in the

TX aparatus.

7.2.4 OCR Effect

The OCR effect on velocity results has been a topic of interest recently with respect to its application for pore pressure predictions at great depths below the ground. When a layer of soil is overpressured, either due to undercompaction (similar to an undrained behavior), fluid expansion, and unloading [Bowers, 1995,Bowers, 2001], the velocity results could cause the incorrect calculation of overburden stress and hence pore pressure. In such cases of undercompaction, there is usually an underprediction of pore pressure, which can have serious implications. Thus the relationship of the OCR to the slope of unloading is observed for two of the RBBC specimens (BE046 and BE047). The slope of unloading from the compression curve (C_s) in semi-log space is compared to the slope of the shear modulus (m) in semi-log space in order to maintain consistency in units. Additional unloading experiments were performed, but the results did not yield accurate deformation behavior, as is the case for BE033, in which the specimen had insufficiently separated from the boring tube. All the cases are summarized in Table 7.4. Although the BE033 experiment with natural BBC in the brass tube is included in the table, it is not included in the analysis since it evidently did not exhibit normal deformation behaviors, as supported by its calculated C_s value.

The two primary experiments chosen to support the unloading trend are BE046 and BE047, which were both RBBC specimens tested in their acrylic consolidation tubes. The velocity curves for the respective experiments are shown in Figures 7-16 and 7-17. As is seen in these figures, the unloading portion is initially linear, but develops into a curved shape as unloading continues. Studies such as [Bowers, 1995] have been performed that attempted to describe this curved shape with fitted equations; however, due to the semi-log space use in the compression curves, as well as the ability to better fit a linear curve in semi-log space, the rest of the analysis is performed with the axial consolidation stress in log scale.

When comparing the unloading slopes of the compression curve (C_s) at different

unloading loops, there is a small discrepancy between the slopes, which is attributed to the elasto-plastic behavior of soil. The second and third slopes tend to be steeper than the first one. The results observed in Table 7.4 do not entirely convey a consistent trend unless the second loop in BE047 is disregarded, in which case there would be a trend of increasing slopes with increasing stress level. This trend is also supported by [Adams, 2011], who found that the unloading RBBC portions slope C_s tended to lie between -0.0269 to -0.0348 from 60 - 600kPa range, with increasing slopes for increasing stress level increments. The scatter produced in the bender element results is attributed to the crude use of bender element endcaps applied to either side of a free-standing consolidation tube, with possible extrusion and infrequent data points. Graphs of the compression curves of BE046 and BE047 in semi-log space can be seen in Figures 7-18 and 7-19. While there is a perceivable trend in the slopes of the compression curves, the changes are very small relative to the overall changes experienced by the specimen.

Finally, shear modulus curves in semi-log space can be seen in Figures 7-20 and 7-21. When comparing the slopes of the compression curve (C_s) to shear modulus curve (m), the slope tends to decrease with increasing max stress level. Since the unloading portions were all taken to approximately the same OCR, they can be readily compared. It is expected that as the OCR increases, the slope of the unloading portion m should increase, therefore the low value seen for m_2 for BE046 is partly attributed to the lower OCR level that was reached. Additionally, the second loop for BE047 once again does not agree with the trend, therefore is likely an outlier, since m_2 is lower than m_3. The trend of decreasing slope m with increasing max stress level conceptually can be explained by the travel path of the velocity through a compressed medium. With increasing stress level, the particle alignment produced a more direct transmittal of energy that presented as an increase in the velocity measurements. As the specimen was unloaded, the contacts established during compression remained more intact than the state at which they were at the same stress level but during normal consolidation. A schematic of this concept can be seen in Figure 7-22. Another contributing factor that can explain the behavior is the achievement of higher horizontal stresses during

Table 7.4: The unloading portions of bender element testing on RBBC were compared, with a summary of results is shown

Test	Unloading Loop	Max Stress Level (kPa)	OCR	G_{max} slope, m (kPa/kPa)	Compression Curve slope, C_s ($1/kPa$)
BE033	1	600	3	22,489	-0.0023
BE046	1	800	2	29,241	-0.0230
	2	1600	1.6	7,721	-0.0258
BE047	1	400	2	61,187	-0.0527
	2	800	2	36,257	-0.0318
	3	1600	2	38,644	-0.0571

incremental loading.

7.3 Anisotropy Measurements in Clay

7.3.1 Evaluation of cross-anisotropic behavior

The resedimentation process has been shown to repeatedly yield results supporting its cross-anisotropic behavior. For example, in [Germaine, 1982], based on the directional shear cell measurements, the lateral directions proved to have consistent strength properties and yield criteria. Furthermore, [Adams, 2011] showed that in cubic triaxial resedimented specimens, the permeability was uniform in both lateral directions, which were arbitrarily squared-off. Generally in the field, the historical depositional process occurred in the vertical direction, building upon laterally-homogeneous layers; however, there is also possibility of erosional effects and differential lateral movements which would cause uneven smearing between layers causing an arbitrary sample to have orthotropic symmetry. When samples are made in the laboratory using the resedimentation technique, the clay is K_0 consolidated, preventing any lateral heterogeneities as the uniaxial vertical compression is performed.

The effectiveness of producing a cross-anisotropic specimen during resedimen-

tation has also been evaluated with respect to the boundary interactions with the resedimentation tube. During the consolidation process, as is well known for oedometer testing [Germaine and Germaine, 2009], the side wall friction has an effect on the homogeneity of the specimen. The stress distribution along the wall will not necessarily be uniform, especially with tubes that have higher aspect ratios, as the stress at the top is higher than at the base [Abdulhadi, 2009]. The specimen can also vary laterally, with the center having no knowledge of the sidewall friction. Tests were performed by [Germaine, 1982] to ensure the homogeneity of water content throughout the specimen using x-ray diffraction pattern and air-drying vertical and horizontal cuts the test for stratification. Both results showed reliable uniformity throughout specimens.

In the case of the testing performed during this research, sidewall friction was deemed irrelevant. When bender element testing was performed in the resedimentation tubes, the bender elements were centrally placed so that the shear wave propagated vertically down the middle of the tube, away from the side walls. Additionally, when cubic triaxial specimens are cut, the area of clay that was adjacent to the wall during resedimentation would be cut away to form the desired geometry.

7.3.2 Anisotropy Results in Clay

As previously mentioned, the future development of this research is to simultaneously measure P and S-waves in the vertical and horizontal directions to populate the anisotropy matrix. Before this occurs, some preliminary anisotropy testing was conducted on oven-dried specimens that ranged in stress from 300kPa to 10MPa. These specimens of RBBC had been previously tested in both CRS and Cubic Triaxial Permeability tests. The stress level reported was the maximum stress level that the specimen was resedimented to. All of them, however, were unloaded to an OCR=4, which means that when they were tested by [Adams, 2011], they were at 1/4th of the maximum stress level listed. The specimens were then oven-dried and used for P-wave testing at atmospheric stress. The results of the P-wave velocities using ultrasonic transducers measured in the vertical and horizontal directions can

be seen in Figure 7-23. The velocity in the horizontal direction is considerably faster than the vertical direction, which can be explained by the preferential clay particle alignment in the horizontal direction. There is also a consistent trend according to the increasing stress level, demonstrating that the velocities in the two directions diverge as the stress goes up. The rate at which the velocities vary as a function of stress are not equal for the different directions. The horizontal velocity increases linearly with a slope of 27 (m/s)/MPa, while the vertical direction decreases with a slope of -9 (m/s)/MPa. The rate of change of the horizontal velocity is 3 times as fast as the vertical velocity. The increasing horizontal velocity is a material-dependent property caused by the preferential alignment of clay particles in the horizontal plane. The decreasing vertical velocity is, however, difficult to explain and could be attributed to a drying effect. With oven-drying, there is a high likelihood that horizontally-oriented cracks occurred, which would decrease the P-wave velocity. A similar behavior was exhibited in a study done by [Piane et al., 2011] that vertically loaded shales and recorded a decrease in shear and compressional velocities when confining stress was held constant. This decreasing trend was attributed to crack formation.

In order to more readily compare the velocities in the horizontal and vertical directions, the anisotropy value is calculated as follows:

$$r_{vp} = V_{ph}/V_{pv} \tag{7.5}$$

where V_{ph} is the P-wave velocity in the horizontal direction and V_{pv} is the velocity in the vertical direction. The results of the anisotropy calculation are shown in Figure 7-24. The P-wave velocity anisotropy for dry RBBC can be roughly described by the following equation:

$$r_{vp} = 0.045\sigma_{max} + 1.62 \tag{7.6}$$

σ_{max} is the max vertical consolidation stress in MPa.

In Figure 7-24, a data point from Fioravante is shown for comparison [Fioravante and Capoferri, 2001]. As previously mentioned, Fioravente conducted bender element testing on Ticino sand and measured the P-wave velocity in vertical and horizontal

directions under isotropic effective stress levels. Although his experiments were under isotropic conditions while this research was conducted on K_0 consolidated, it is clear that clay has a much higher anisotropy ratio, relatively speaking, than sand due to the particle geometry and contact distribution.

While most anisotropy measurements conducted on clays are performed while the clay is saturated, the tests performed here were done on oven-dried specimens for two reasons. Firstly, the specimens tested were readily available from previous testing and would provide immediate results at a wide range of stress levels, which would normally take many months to make. Secondly, with the absence of water, the P-wave velocity behavior through the clay specimens can be singled out. The velocity of P-waves through water is similar to a threshold. If the velocity through the porous medium is lower than the P-wave velocity of water (V=1480m/s), then the readings will be that of water. Only when it reaches values higher than that of water will the P-waves represent the velocity through the medium, which is at high stresses, usually greater than 500kPa. Looking at Figure 7-23, the measured vertical P-wave velocity is lower than the velocity through water, in which case the velocity would primarily be that of water. Although drying the specimen can modify its behavior, the velocity anisotropy results of dehydrated materials are a better indicator of the clay specimen behavior and the structure of the clay particles.

7.3.3 SEM Image Analysis

In order to develop a better understanding of the behavior exhibited by RBBC tested during this research, Scanning Electron Microscope (SEM) images were taken of the some of the tested specimens post-experiment. These SEM's were taken on cubic specimens produced by [Adams, 2011] that underwent permeability testing before being cut and imaged. This batch of cubic specimens from [Adams, 2011] comprise the majority of the data points seen in the anisotropy relationships in Figures 7-23 and 7-24. The anisotropy seen in the velocity results clearly transcend to the visual realm. Observing Figures 7-25 and 7-26, the two directions are very different. These particular images were taken from a specimen that was consolidated to a maximum

stress of 8MPa and rebounded to an OCR=4, with a porosity of n=0.536 at the maximum stress level. In Figure 7-25, the majority of the voids are relatively small and there are a few larger-sized grains that have been cut, so that the large diameter of the particle is exposed. Since the specimen was cut horizontally, the likelihood that one of the larger grains to be cut at the wide point is very slim, as is seen by the scarcity of large-sized particles. When looking at the vertical cut in Figure 7-26, many of the long, flat clay particles are seen since there is a much higher possibility of cutting through them due to their platey geometry. It is also evident that the flat clay particles are preferentially oriented in the horizontal direction, with a few of them still tilted at a much smaller angle relative to the horizontal than they originally were during deposition. The orientation of the particles becomes closer to zero degree tilt with increasing stress level, unless there is a large particle underneath it to prevent this, such as seen in the area circled with a red box in Figure 7-26.

7.4 Comparison of Different Methods of Measuring the Constrained Modulus, and Others

In order to evaluate different techniques of obtaining the elastic properties for various materials, a series of experiments were performed on cylindrical samples of multiple materials including the following: steel, aluminum, acrylic, and rubber. These samples were all approximately 7.1cm in height and 3.4cm in diameter. The three techniques were ultrasonic P-wave transducers, extensometers, and accelerometers.

The P-wave transducers were used for their ability to easily test solid materials. The transducers were placed on the top and bottom flat surfaces of the specimen with the help of couplant (specifically vacuum grease in this case). The couplant ensures the transmittal of energy between two flat, hard surfaces. No additional force was applied except to keep the transducers in place. The start-to-start arrival time method was used to determine the travel time of the wave over the length of the specimens. Using the density of the material and the velocity of the P-wave, the

Table 7.5: Constrained modulus (M) for various materials obtained using different methods

	Steel	Aluminum	Acrylic	Rubber
Published values[1] (GPa)	283	102	8.5	0.2
P-wave transducer (GPa)	227.5	89.8	8.2	-
Accelerometer (GPa)	193.1	81.7	4.13	0.093

constrained modulus was computed. The results can be seen in Table 7.5, as well as graphically in Figure 7-27. It should be noted that the rubber specimens were too long to obtain a P-wave measurement using the ultrasonic transducer due to the highly attenuative nature of the material.

The accelerometers introduced in section 4.4 were used to measure both the compressional and shear wave velocities through the various materials. The cylindrical test specimens were placed between two endcaps with mounted dual-axis accelerometers (Figure 4-15). The accelerometers were placed in an orientation so that the Y-axis was in the vertical direction and the X-axis was in the horizontal direction. To propagate an arbitrary waveform through the specimen, the load frame was struck with a hard object. A steel ball was dropped at the top of the load frame to send a compressional wave through the specimen, which would be registered by the Y-axis component of the accelerometer. To create a shear wave, a metal object was used to strike the side of the top bar of the load frame. This would send a SH wave that would be picked up by the X or Y-axis component of the accelerometer. The height of the plug is divided by the time between the arrivals of the first signals passing the accelerometers on either endcap to obtain the velocity of the signal. This calculated velocity is corrected by the measured "blank" velocity. This is obtained by omitting the specimen and placing the two endcaps on top of each other. This facilitates the seamless testing of multiple specimens of various heights without the need to consider the distance between the accelerometers and whether to measure the distance between

[1]The published values were found in [Callister and Rethwisch, 2011] and [Harper, 2001]

Table 7.6: Shear modulus (G) for various materials obtained using different methods

	Steel	Aluminum	Acrylic	Rubber
Published values[1] (GPa)	79.3	26	1.18	0.0034
Accelerometer (GPa)	22.2	7.28	0.44	0.058

the centerline of the accelerometers or the extreme ends of the accelerometers. The P-wave velocities obtained were used to calculate the constrained modulus M, and can be seen in Table 7.5. The tangential accelerometer measurements were used to calculate the shear modulus of the specimens. The results can be seen in Table 7.6 and Figure 7-28. The accelerometers have consistently been shown to under-predict the elastic parameters of the materials tested, with an especially large discrepancy in the shear modulus values.

Some of the difficulties exhibited during the testing with accelerometers included the variability in the signals recorded. Manually sending the wave through the specimen introduces the opportunity for human-induced variability. The frequency or force with which the wave is propagated is likely to change from one trial to the next. Although this would theoretically be irrelevant to the measurement of travel time from one accelerometer to the next, there is a chance of mis-hits or double hits that might interfere with the signal readings. Furthermore, there is a sensitivity factor that needs to be considered. Materials with high travel speeds are more likely to have errors and variability between multiple iterations due to the sensitivity of the material. Slight variability in user-defined travel times can have large effects on the velocity readings. This makes the accelerometers sub-optimal for high stiffness materials.

As described in section 4.5, 2 extensometers were mounted on either side of the curved portion of the cylinder with elastic bands. The vertical load was increased while the deformation was monitored by the extensometers. One advantage of the extensometers is its ability to measure the Young's modulus of both very hard ma-

Table 7.7: Young's modulus (E) for various materials obtained using different methods

	Steel	Aluminum	Acrylic	Rubber
Published values[1](GPa)	207	69	3.34	0.01-0.1
Extensometer (GPa)	206.5	71.2	3.7	0.012
Accelerometer (GPa)	62.4	17.9	1.25	-
Accelerometer using M and published G (GPa)	182.6	65.9	3.1	0.0099
Accelerometer assuming measured M is rod modulus (GPa)	193.1	81.7	4.1	0.093
P-wave transducer (GPa)	195.5	67.4	3.3	-

terials (i.e. steel, concrete) as well as that of soft materials with large deformations like rubber. Although, in order to capture the deformation behavior of extremely stiff materials, higher resolution is usually needed, thus the AD1170 data acquisition card was used with a high integration time. Multiple experiments were performed on each material, with the averaged results presented in Table 7.7. They are compared to published values that are generally found in literature. Since even the published values tend to vary slightly, an approximate average was taken. Additionally, it should be noted that for the materials tested, even though they were common materials, it was unknown the exact type of material grade they were, for example whether the aluminum was Aluminum 1100-0, 2024-T4, or 6061-T6. Rubber has an especially wide range comparatively, since there is a wide variety of rubbers and rubber composites. Additionally, this variation in results could also be amplified by end conditions during testing. The values seen in Table 7.7 from the extensometers correspond very well with the well-established results. They are consistently slightly higher than the published results, which could be a function of the extensometers or the type of steel tested. A graph of the results can be seen in Figure 7-29.

As can be seen in Table 7.7, the calculated Young's modulus from the measured shear and compressional velocities show some discrepancies between the expected

values and the obtained values, although this is based on the poor quality shear modulus results. As a better point for comparison, two other cases were considered for Young's modulus calculations with respect to the accelerometers. The first case is using the measured M from the accelerometers and the published values for G. This allows for a more accurate comparison for Young's modulus values rather than using the innacurate G values obtained via accelerometer. The results are seen in Figure 7-29. Another consideration taken into account was that the wave propagating through the specimen behaved more like a rod wave, thus the modulus calculated from the P-wave velocity via accelerometer is actually the Young's modulus. These results can be seen in Figure 7-30. Although this research does not advocate that this is the correct type of wave in this case, it is an interesting mode of comparison that leaves room for interpretation.

In addition to the Young's modulus obtained from accelerometers and extensometers, P-wave transducers are included in the comparison by taking the P-wave velocity obtained from the ultrasonic transducers and calculating the Young's modulus by assuming a published shear modulus value. The calculations can be seen in Table 7.7.

The two dominating factors that had an effect on the accelerometer seemed to be the endcap issue and the length of the specimen. All the results presented above were based on measurements conducted on 7.1cm tall specimens with the use of circular endcaps that were mounted with accelerometers using a strong adhesive. The endcaps created an interface which would cause possible reflections and conversions, thus altering the signal. Without continuous contact, the signals were likely affected by a lack of solid contact between the accelerometers and specimen. In addition, the short specimens did not allow the waves to develop, which leaves the signals prone to near-field effects. Both of these issues were eliminated in testing performed on a long solid steel rod on which the accelerometers were mounted directly. When waves were sent through the steel rod of 2m length, the average P-wave velocity was $V_p = 6005m/s$, which would give $M = 281GPa$. Under these testing conditions, the S-wave velocity yielded an average of $V_s = 1740m/s$, which would give $G = 24GPa$, which is less than half of the expected value. Thus, the results support the use of accelerometers

on non-sensitive materials of low stiffness with a large distance over which the waves can travel to establish separation of the received signals. Furthermore, no setup used during this research could provided reliable shear wave results, indicating an area of concern for use in future experimental programs.

The variability would have been reduced if a consistent source of wave propagation were established. The P-wave transducers function at a frequency range outside the capacity of the accelerometers, which deems them inoperable with accelerometers. Bender elements, on the other hand, did not have the capability to send a strong enough signal through stiff materials. While it is evident that accelerometers are not well-suited for testing materials such as steel or aluminum under the current testing procedures, further testing needs to be conducted whether it would be a viable option for testing of soils.

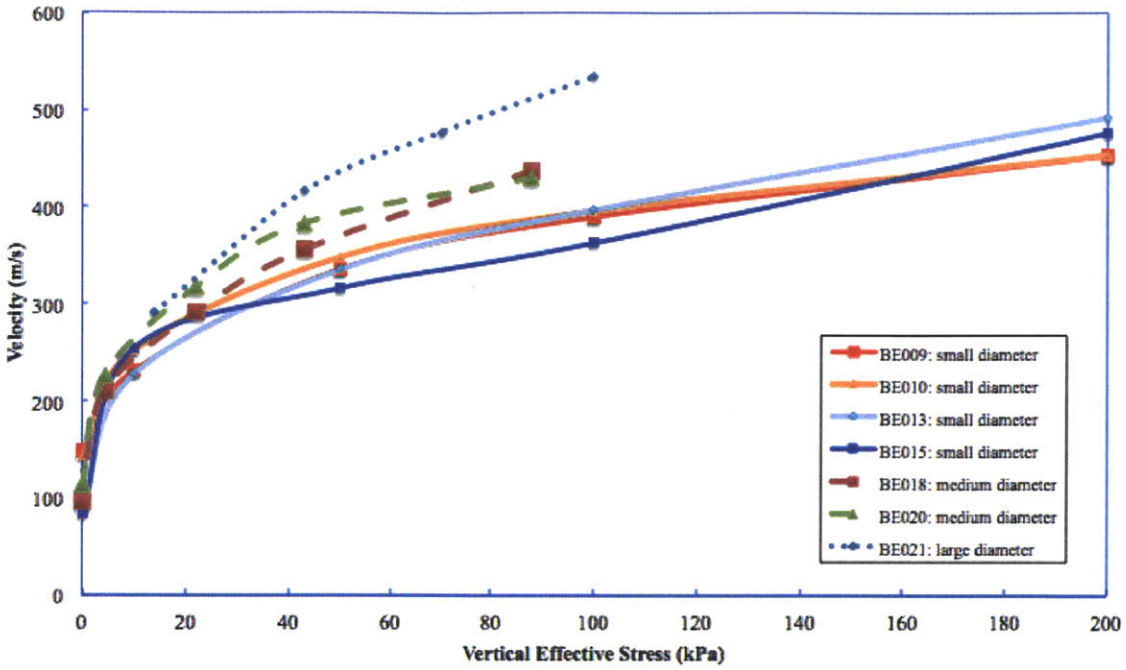

Figure 7-1: Different diameter tubes loaded with thin wooden ends

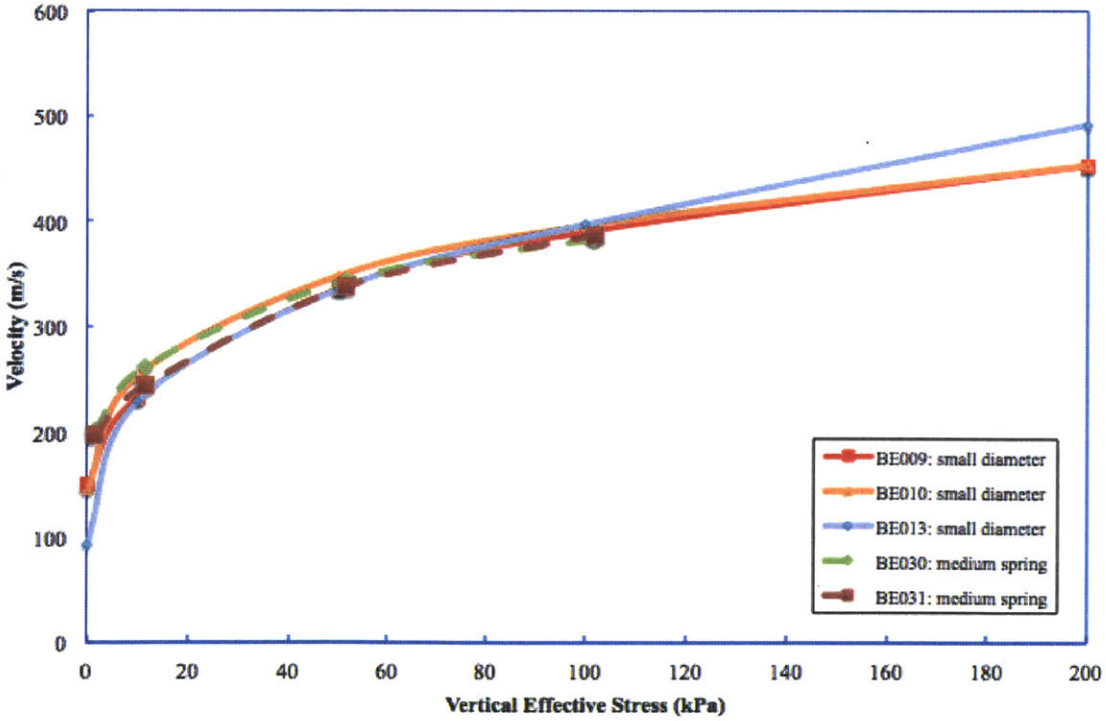

Figure 7-2: Different diameter tubes loaded with a spring system

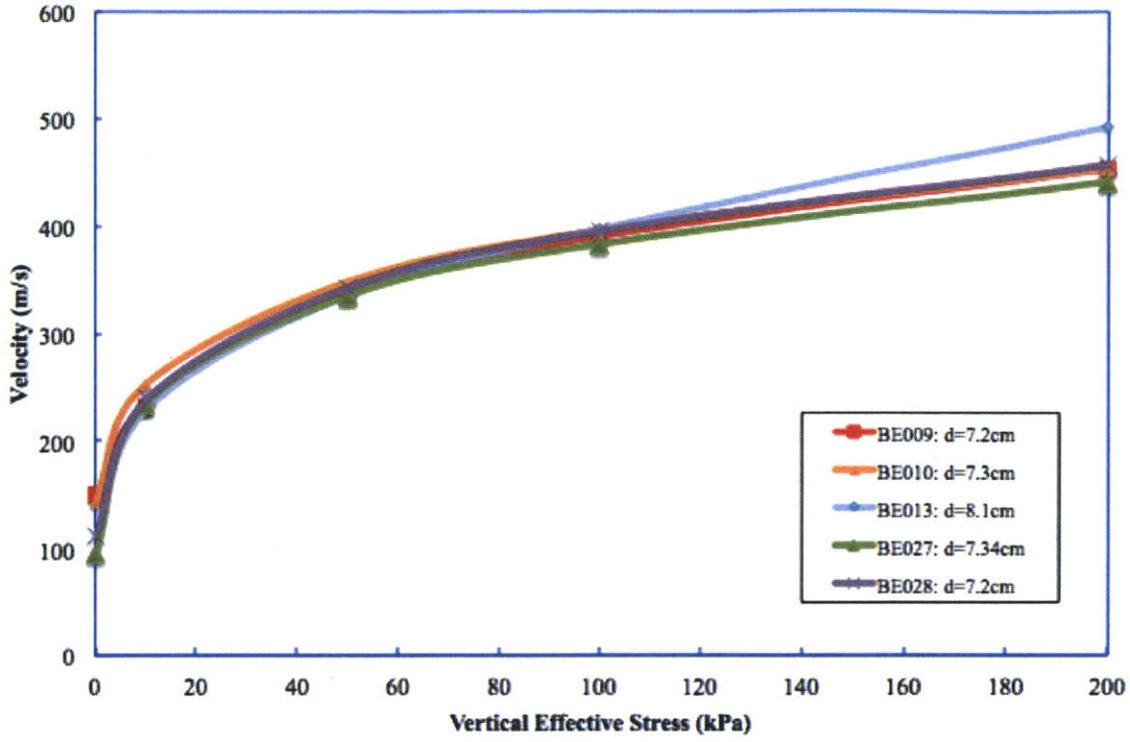

Figure 7-3: Ticino sand velocity results performed with different lengths using Geometry A

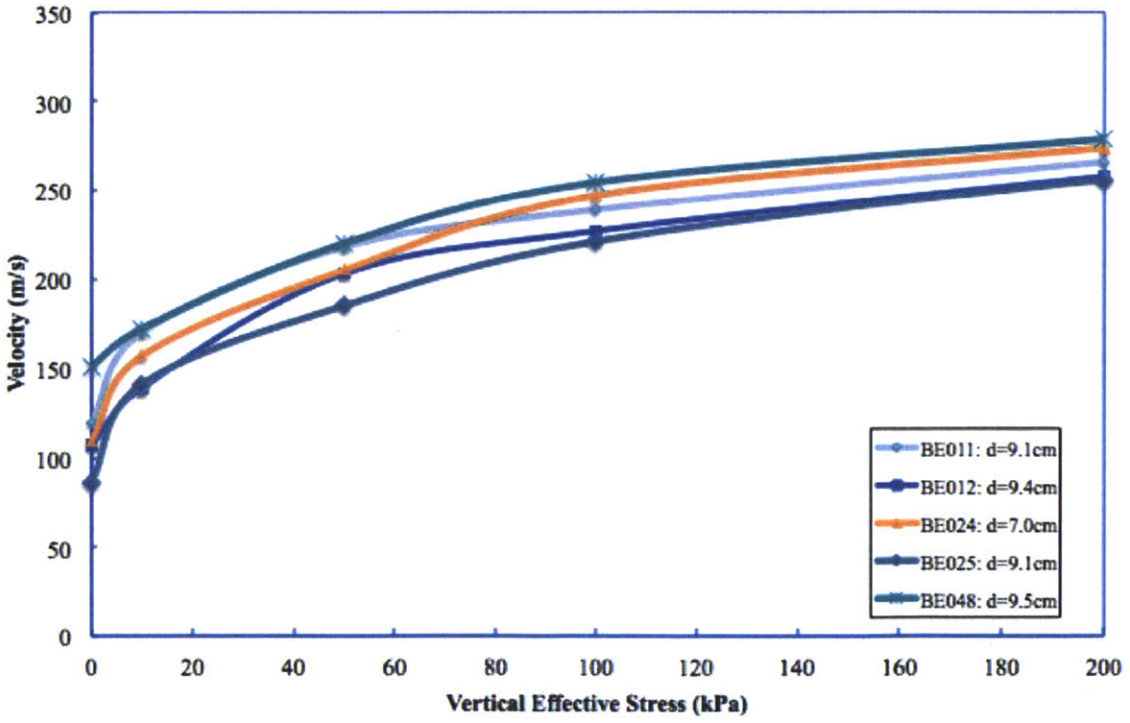

Figure 7-4: Ticino sand velocity results performed with different lengths using Geometry B

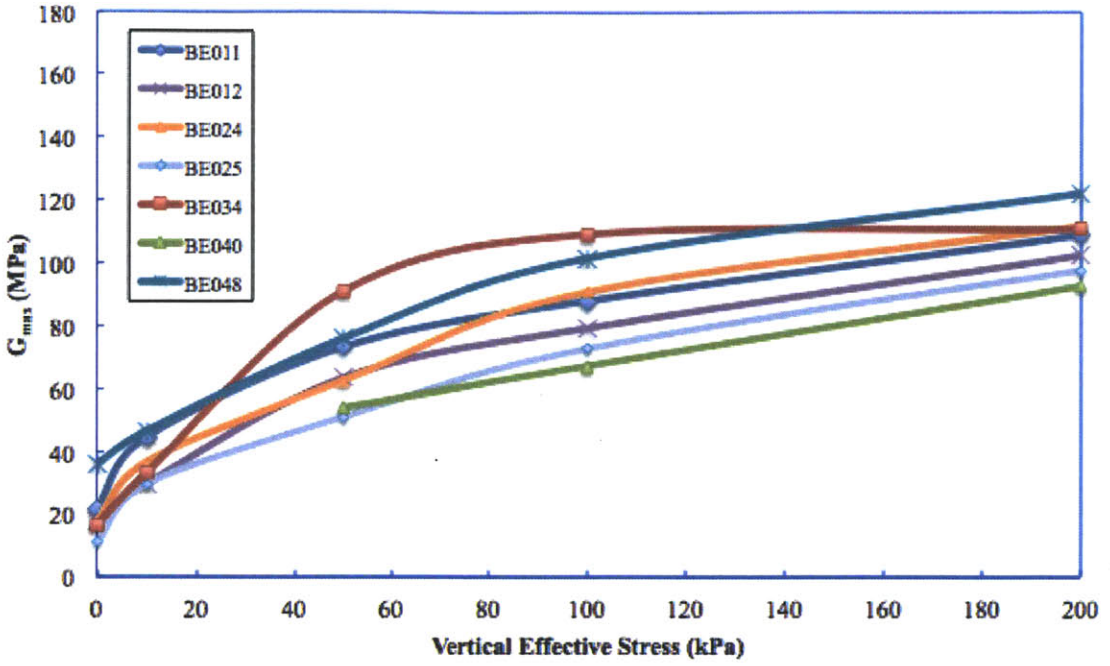

Figure 7-5: All the shear modulus results for Ticino sand using Geometry B

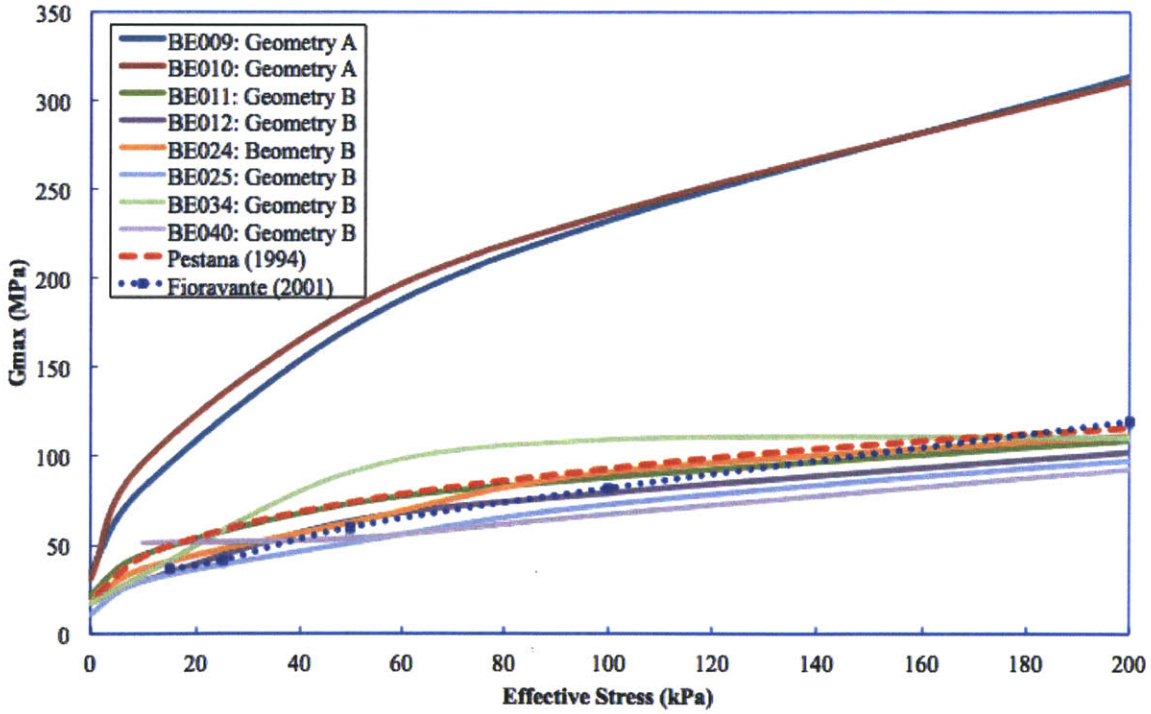

Figure 7-6: All the shear modulus results for Ticino sand for Geometry A and B as compared to the published results

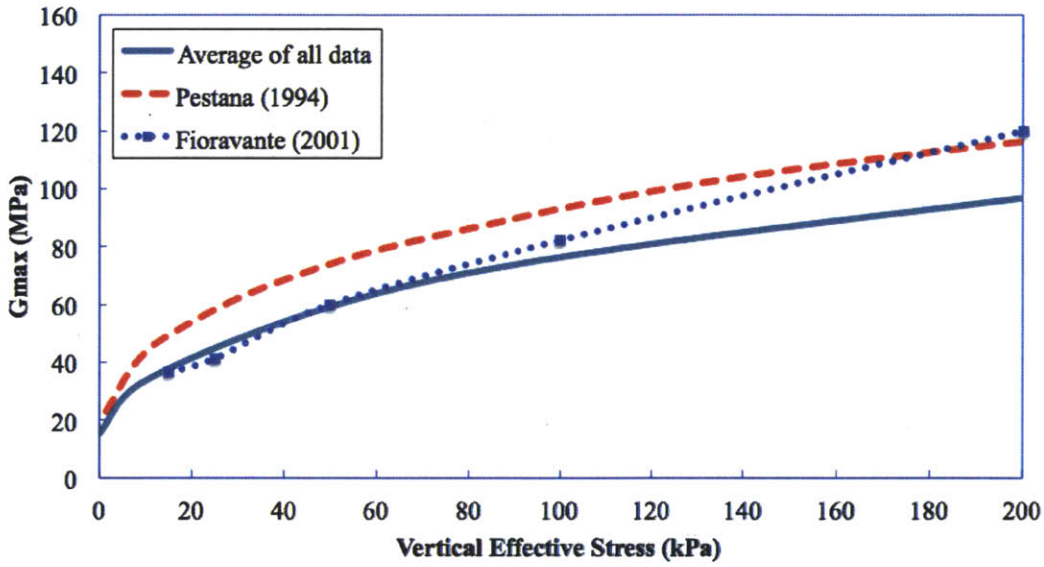

Figure 7-7: A polynomial fit for all the Ticino sand G_{max} results performed using Geometry B compared to published data

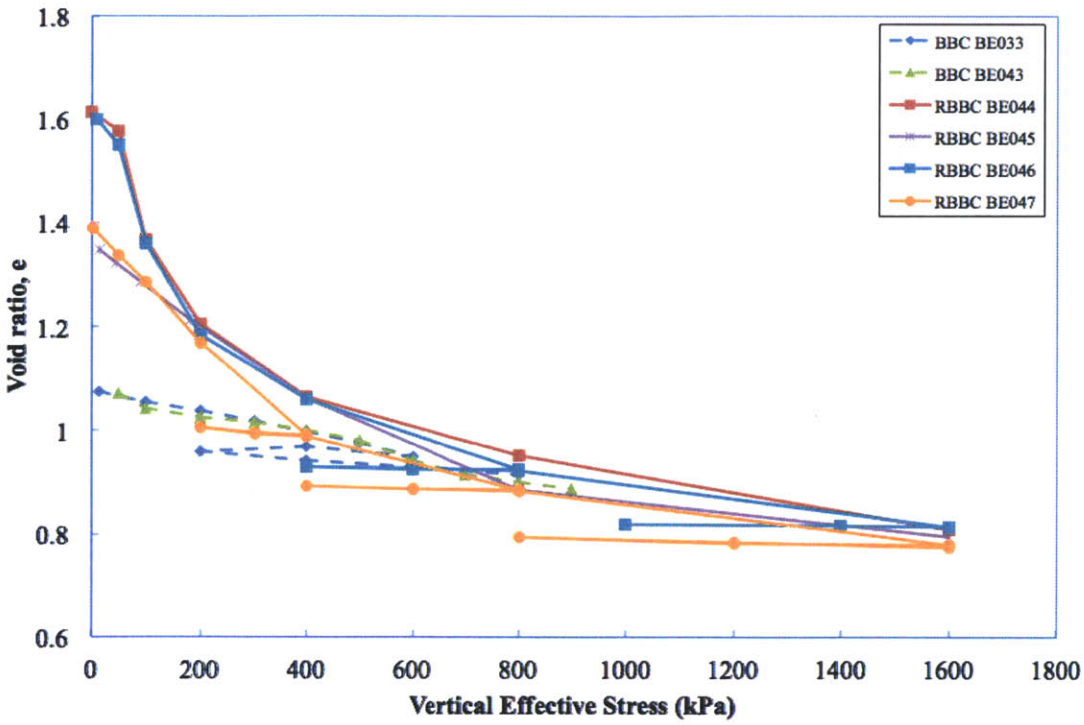

Figure 7-8: Compression curves of the BBC specimens tested with bender elements, shown in linear space ($e - \sigma'_v$)

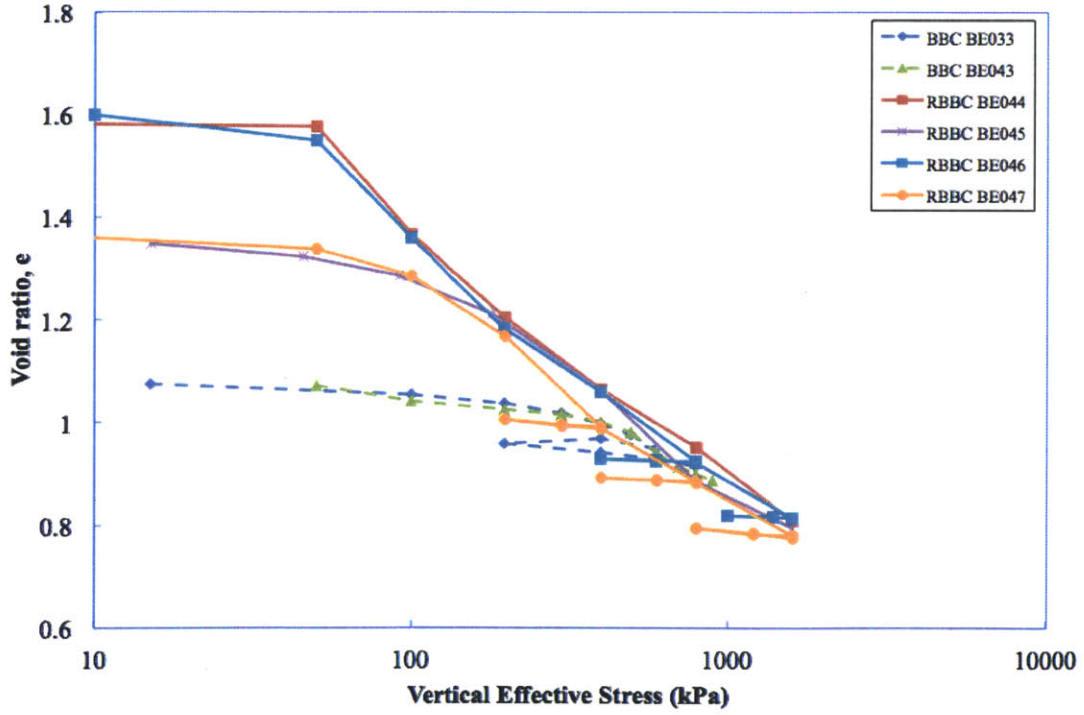

Figure 7-9: Compression curves of the BBC specimens tested with bender elements, shown in semi-log space ($e - log\sigma'_v$)

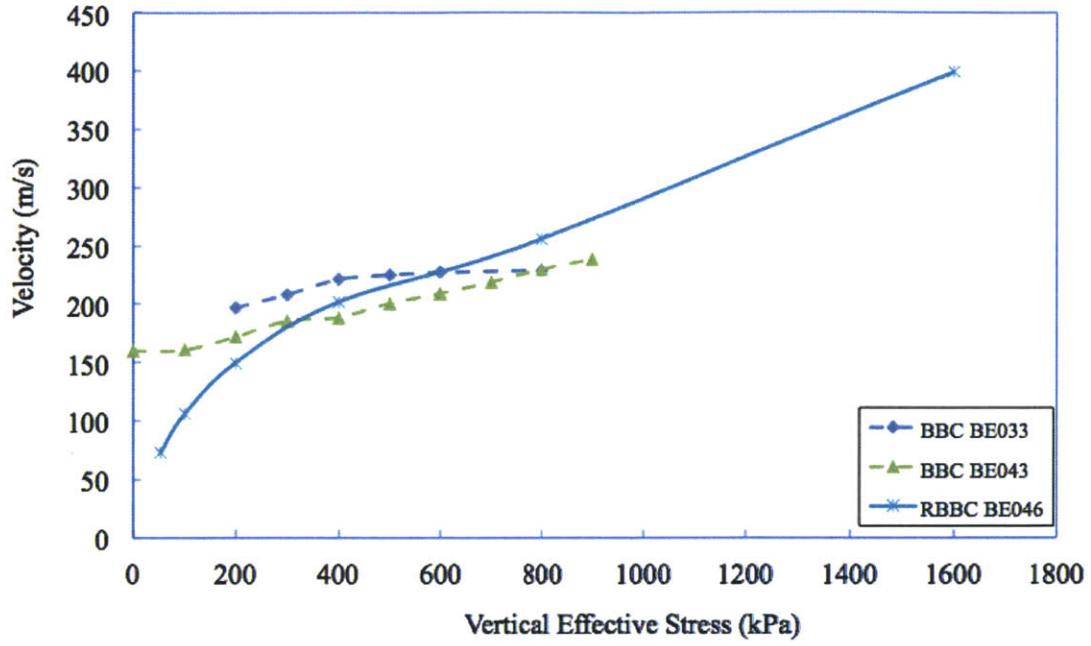

Figure 7-10: Velocity curves are seen for resedimented (BE046) versus natural BBC still in boring tubes

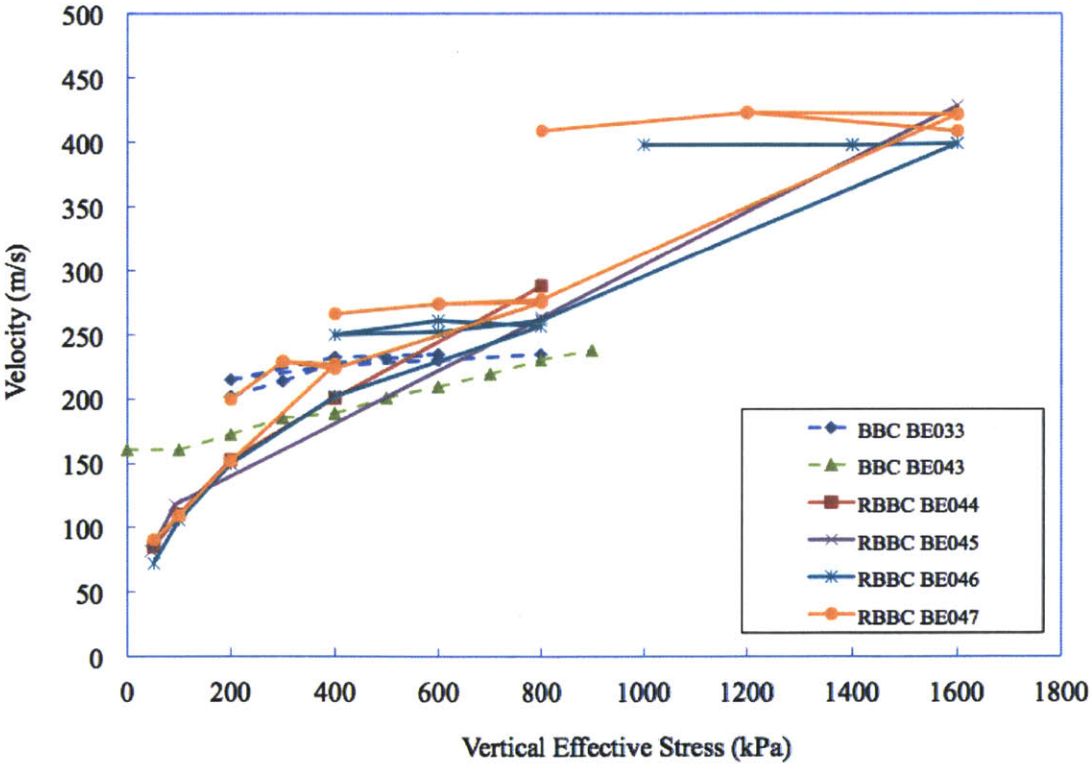

Figure 7-11: Velocity curves of the BBC specimens tested with bender elements, shown in linear space

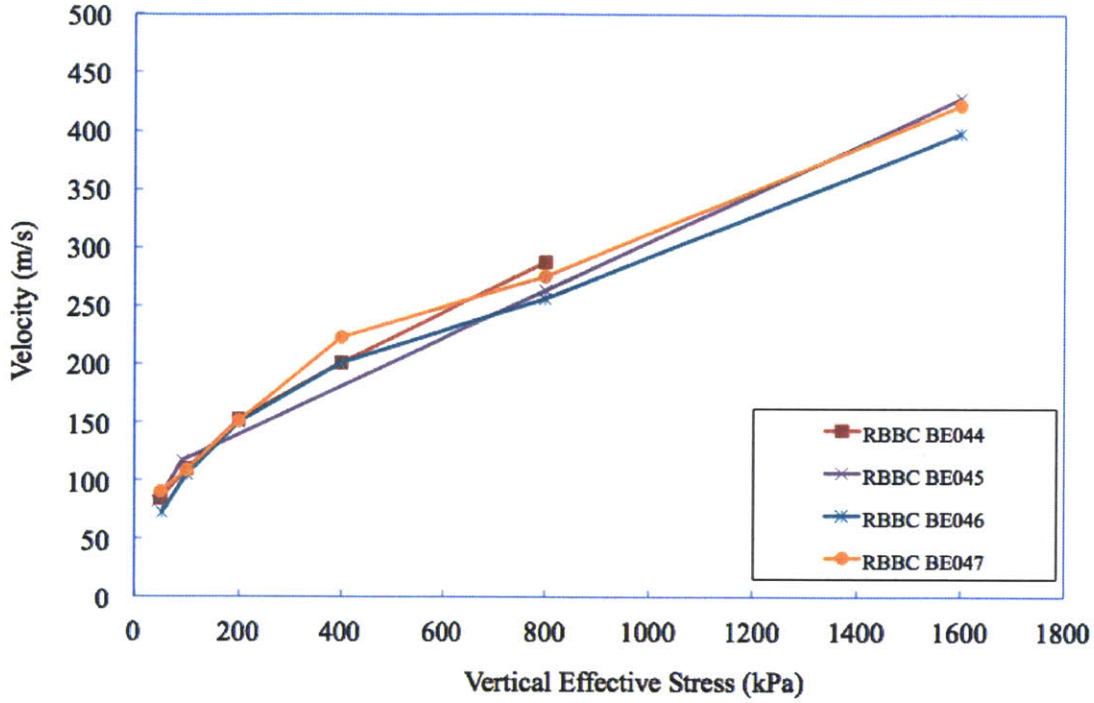

Figure 7-12: Velocity curves of the RBBC specimens tested with bender elements, shown in linear space, without the unloading portions or the natural BBC specimens

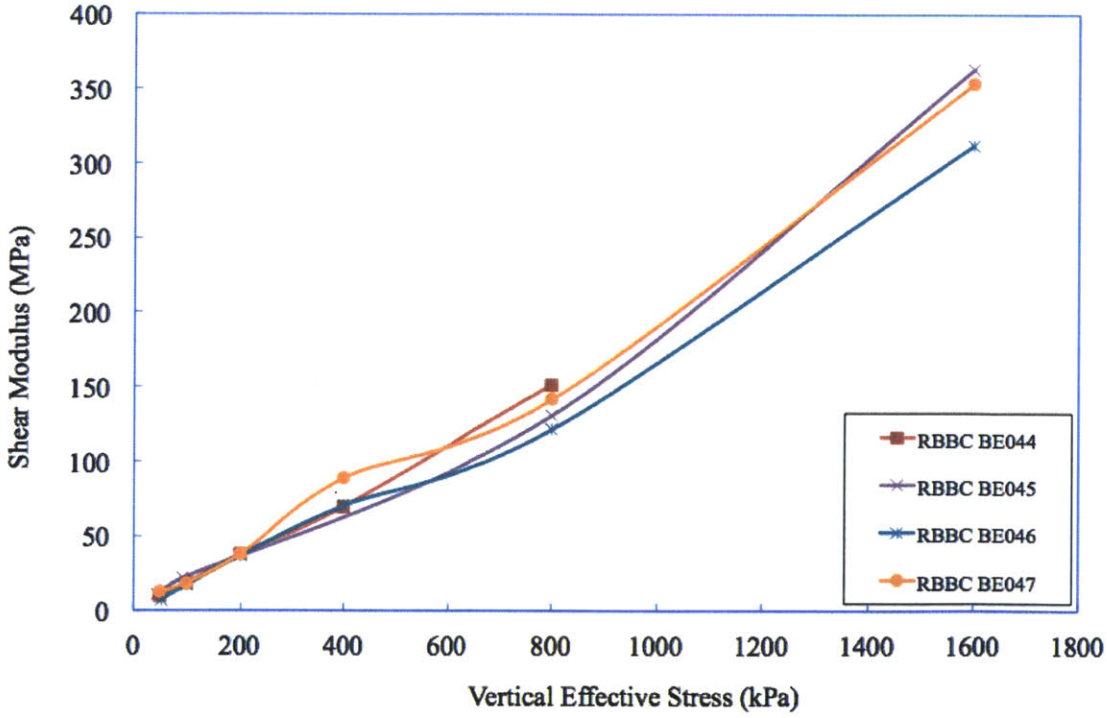

Figure 7-13: Shear modulus G_{max} curves of the RBBC specimens tested with bender elements, shown in linear space, without the unloading portions or the natural BBC specimens

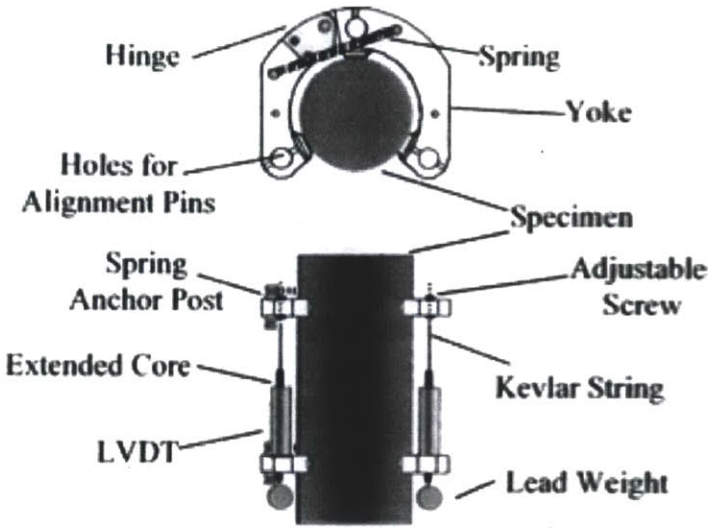

Figure 7-14: [Santagata, 1998] performed on-specimen strain measurements with the setup seen here. It includes a yolk with LVDT's attached to it that monitor deformation

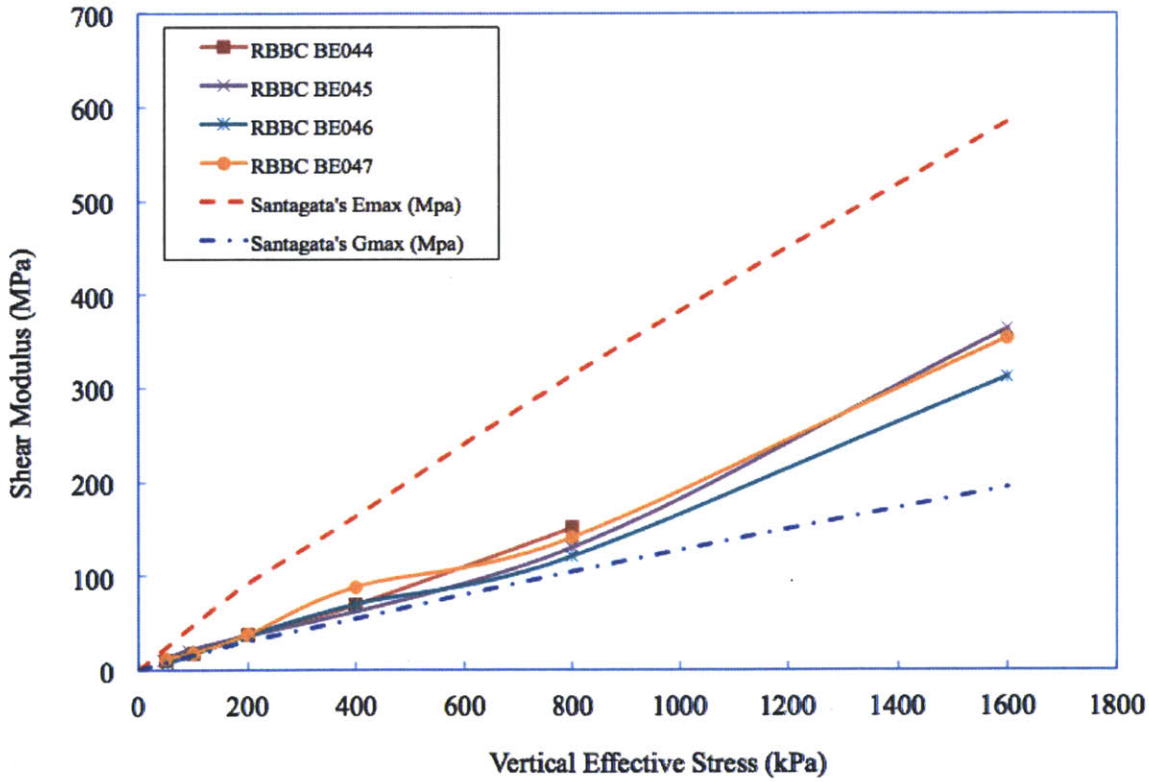

Figure 7-15: Results obtained in this research are compared to a correlation established by [Santagata, 1998] for BBC (more specifically the same Series IV batch was used in both cases)

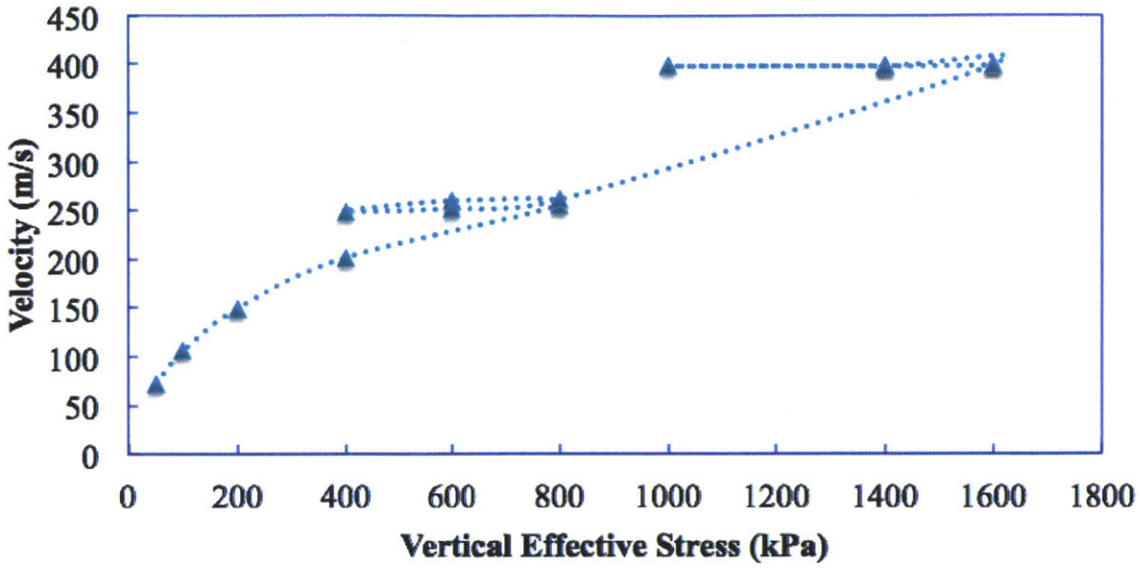

Figure 7-16: A velocity curve for BE046 in linear space

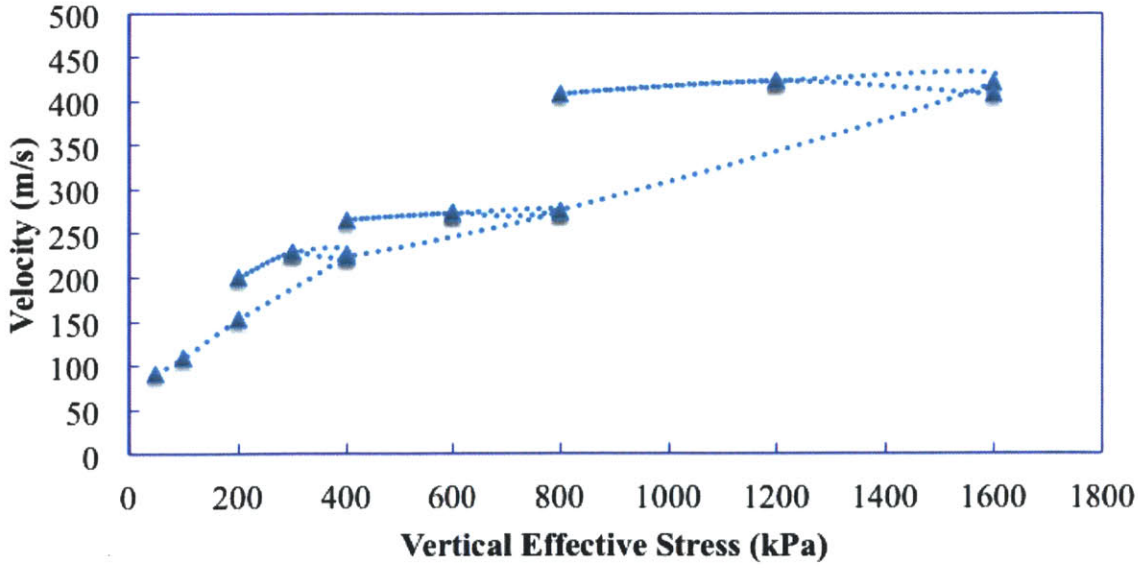

Figure 7-17: A velocity curve for BE047 in linear space

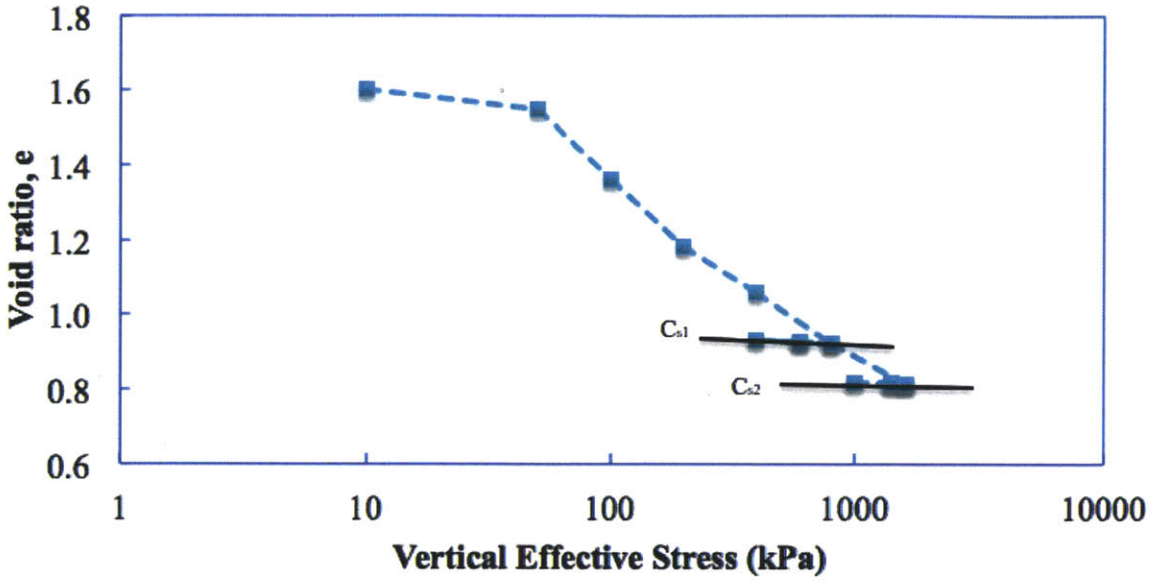

Figure 7-18: A compression curve for BE046 in semi-log space

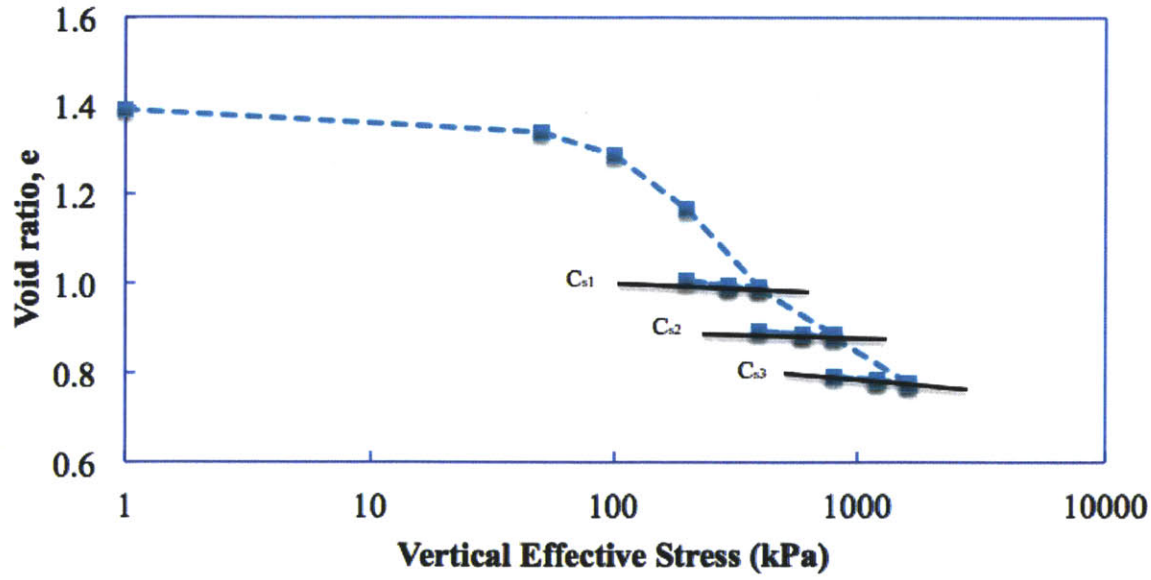

Figure 7-19: A compression curve for BE047 in semi-log space

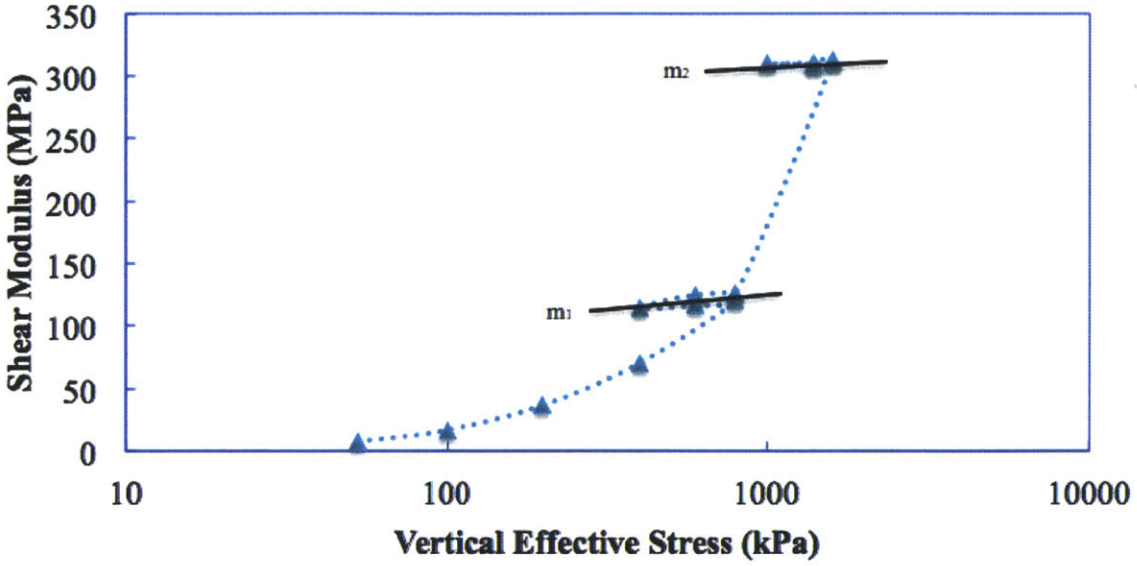

Figure 7-20: A shear modulus curve for BE046 in semi-log space

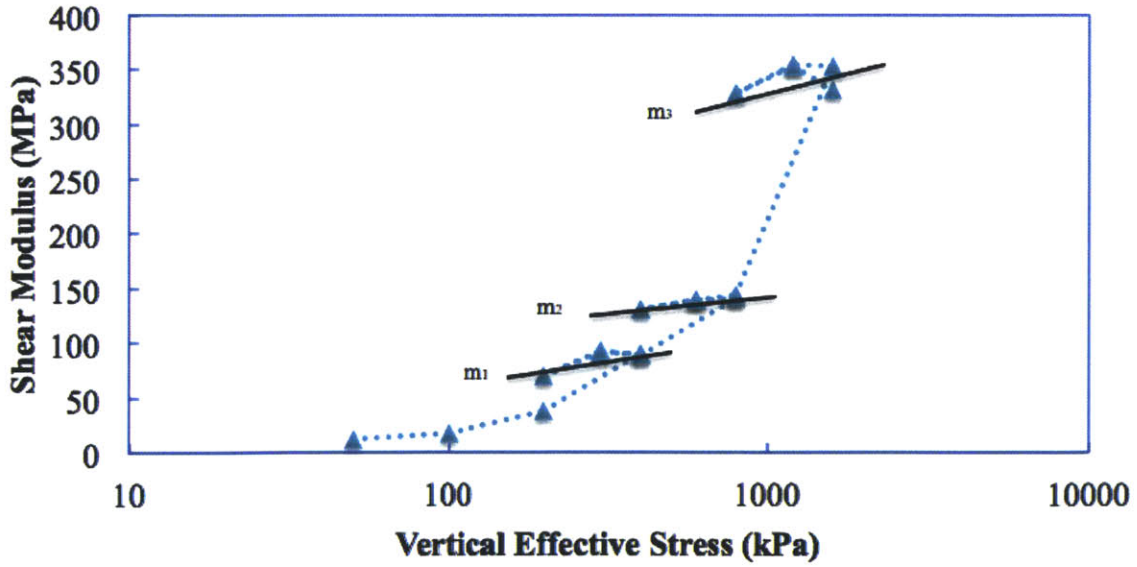

Figure 7-21: A shear modulus curve for BE047 in semi-log space

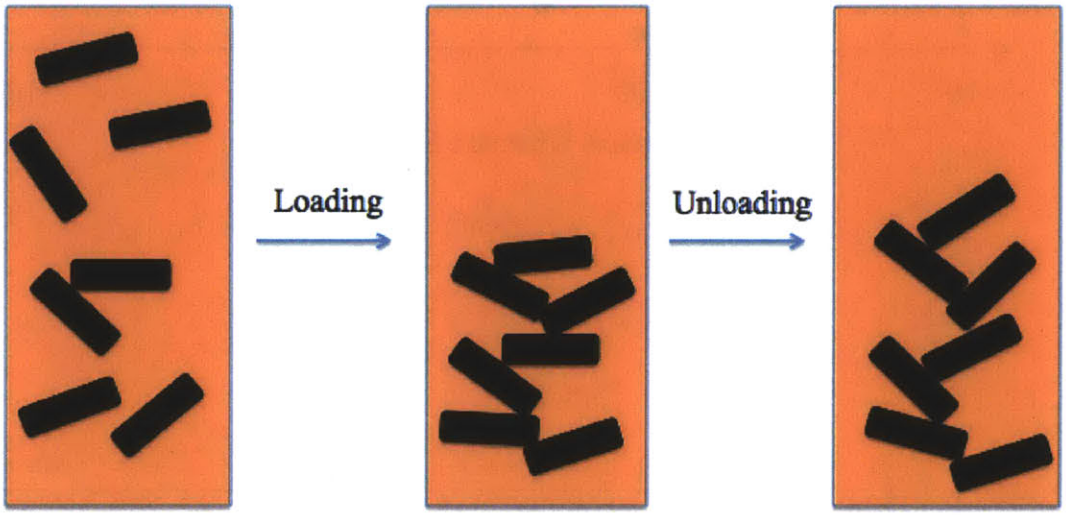

Figure 7-22: The schematic represents what is occurring during loading and unloading. The particle contacts established during loading are maintained to a certain extent, which lead to higher velocities during these unloading stages than a normally consolidated specimen at the same stress level

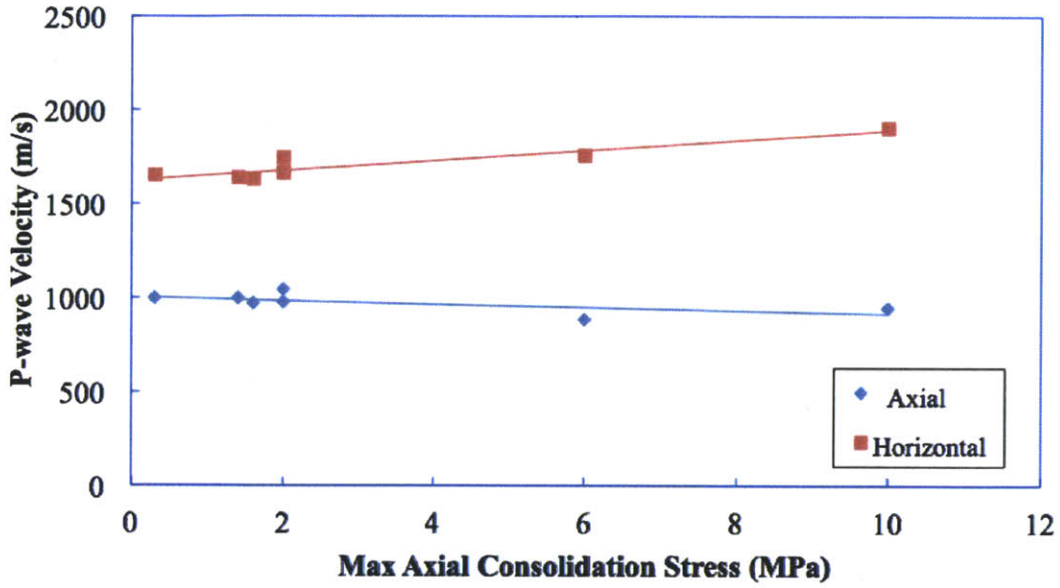

Figure 7-23: The P-wave velocity in two directions is measured on dried RBBC with the max. stress level being the maximum stress level the specimen was taken to before unloading to an OCR=4, then testing and oven-drying, and finally P-wave velocity measurements were performed

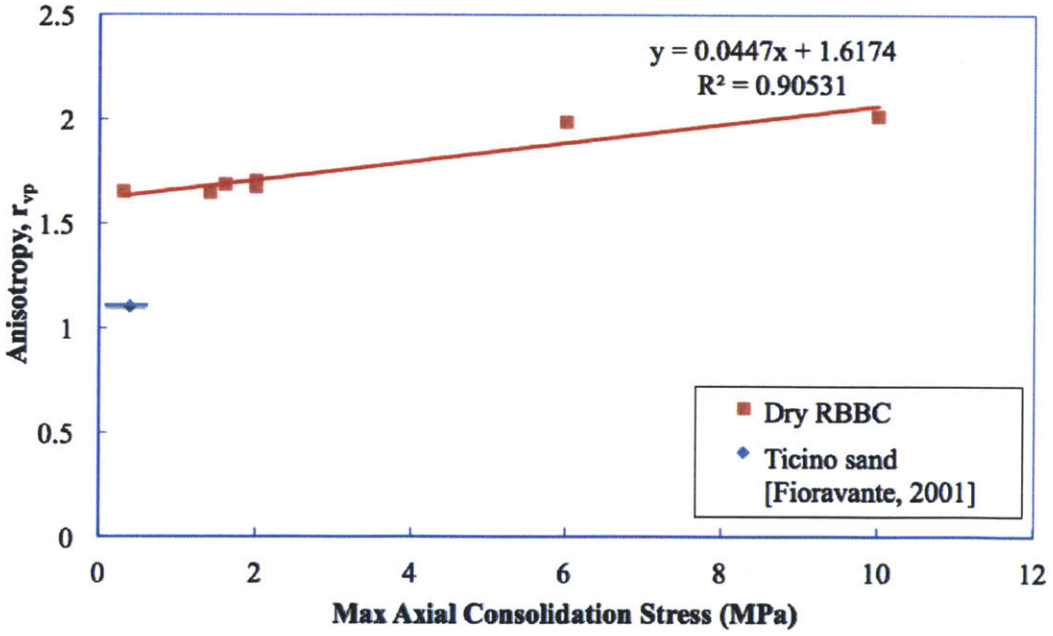

Figure 7-24: The P-wave anisotropy is measured on dried RBBC with the max. stress level being the maximum stress level the specimen was taken to before unloading to an OCR=4, then testing and oven-drying, and finally P-wave velocity measurements were performed

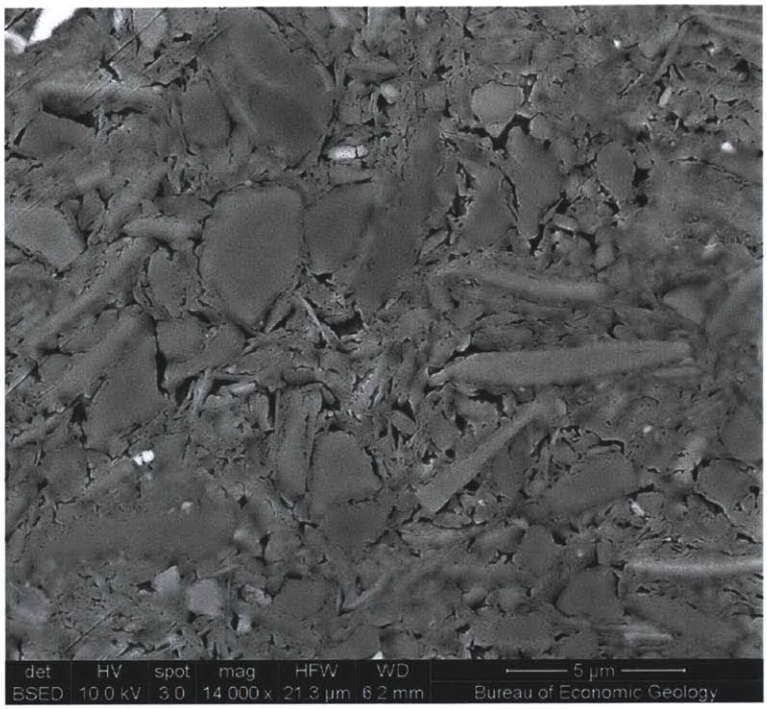

Figure 7-25: Horizontal SEM Image of RBBC cubic specimen consolidated to a maximum stress of 8MPa with a porosity of n=0.536 [Courtesy of UT Austin]

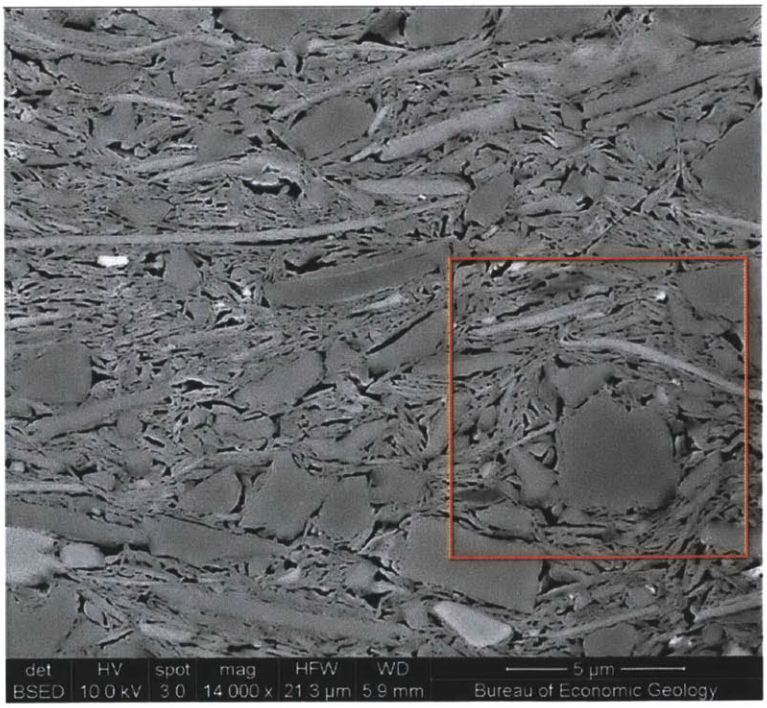

Figure 7-26: Vertical SEM Image of RBBC cubic specimen consolidated to a maximum stress of 8MPa with a porosity of n=0.536 [Courtesy of UT Austin]

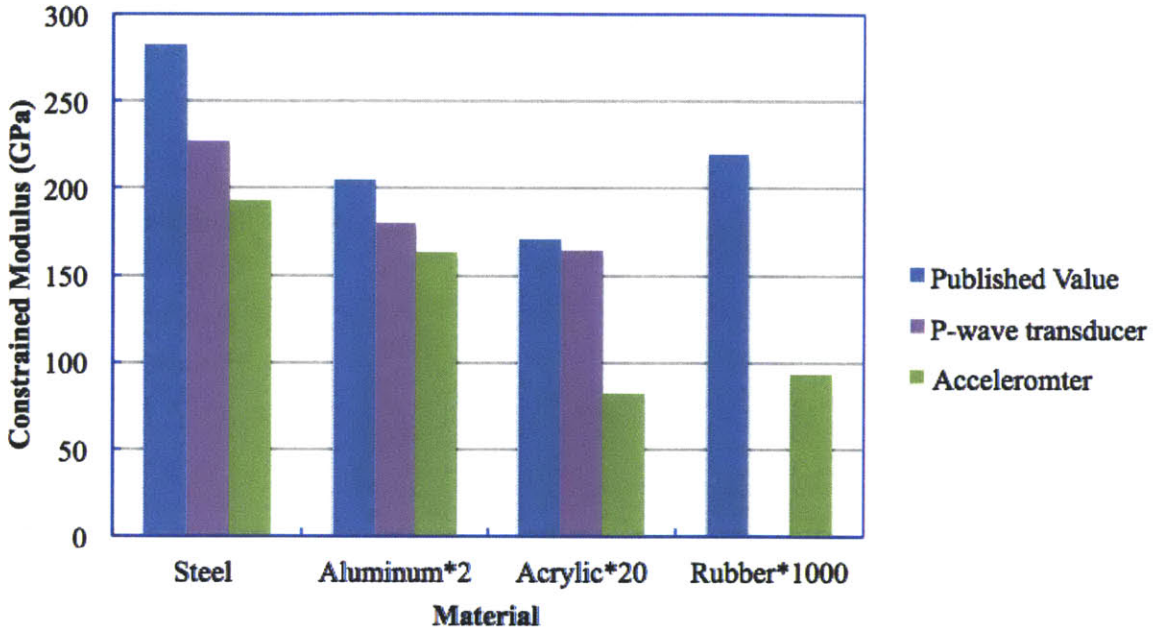

Figure 7-27: Shown here are constrained modulus values for various materials obtained using different methods

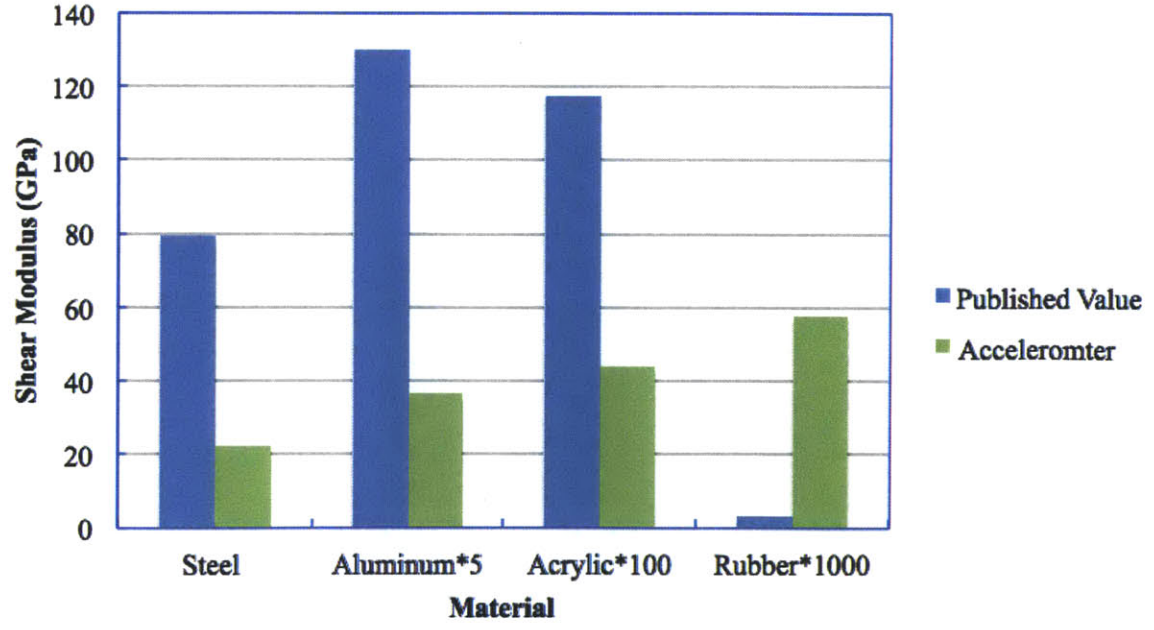

Figure 7-28: Shown here are shear modulus values for various materials obtained using different methods

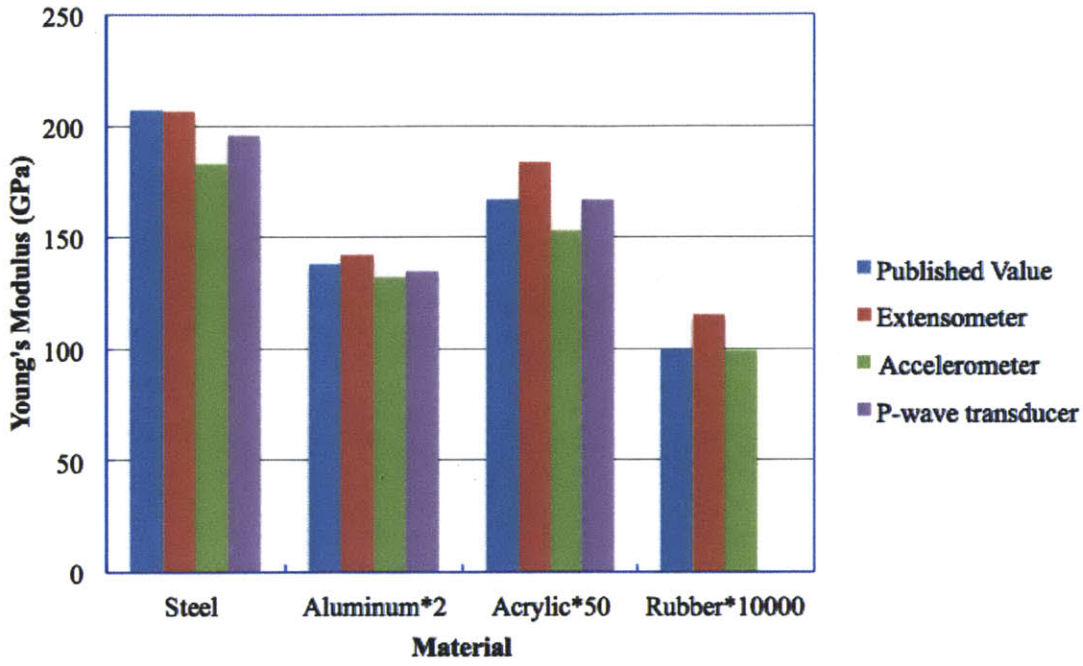

Figure 7-29: Shown here are Young's modulus values for various materials obtained using different methods. The accelerometer results are calculated using the M measured with accelerometers and a published G value

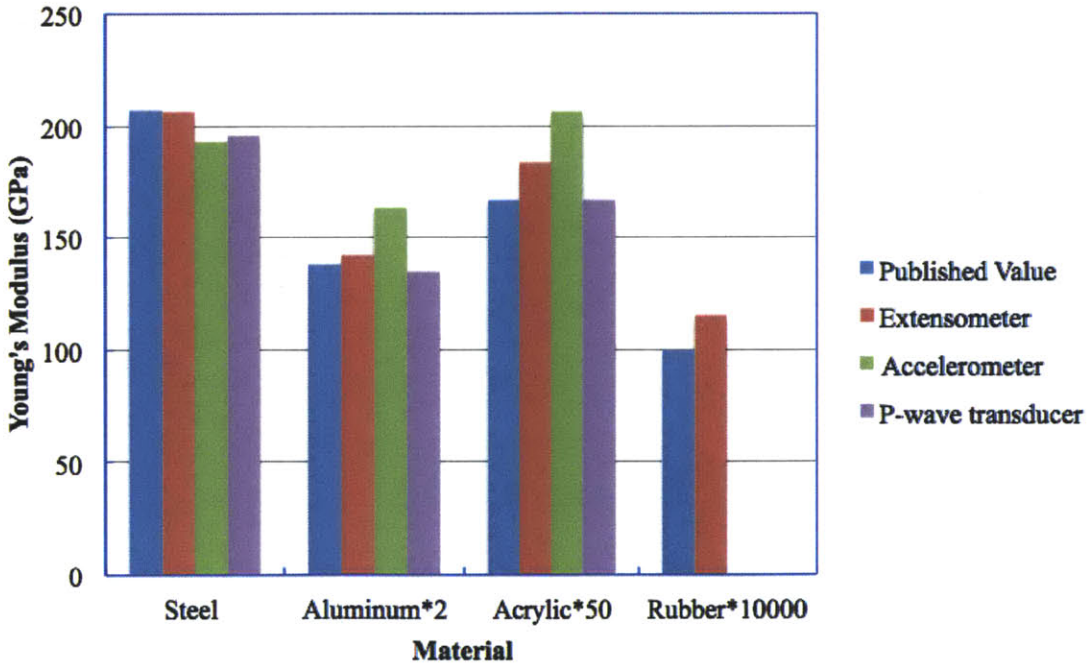

Figure 7-30: Shown here are Young's modulus values for various materials obtained using different methods. The accelerometer results are calculated using the M measured with accelerometers directly by assuming that the wave is in fact more representative of the rod modulus

Chapter 8

Conclusions and Further Research

8.1 Summary of Conducted Work

The overarching goals of this research consisted of understanding the behavior of the relatively novel technology of bender elements, as well as beginning to describe the velocity measurements observed during bender element testing of both sands and clays, with a primary focus on Boston Blue Clay. With the ability to measure the dynamic shear modulus of a material, the progression onto the characterization of its stiffness properties is readily achievable.

The published results available for bender elements were compared and have been shown to yield inconsistent results. In order to better understand the reasons behind the variability present in published data, a study of the behavior of bender elements and the results they produce was conducted by performing a parametric study on the bender element tip geometry, as well as varying certain boundary conditions including the wavelength ratio and aspect ratio. This stage of testing was conducted on Ticino sand due to ease of setup and fast turnover rate.

The next stage consisted of performing experiments on BBC, using both bender elements and ultrasonic P-wave transducers. This facilitated a better understanding of the unloading effect on the shear modulus of BBC as a function of OCR and maximum effective consolidation stress. The anisotropy behavior of velocity in clays was also recorded using ultrasonic transducers as a means to bring foresight into the

development of the stiffness matrix.

Finally, the use of various forms of wave propagation testing and deformation monitoring enabled a cross-comparison of results based on the technology used. During this portion of the experimental work, extensometers, accelerometers, and ultrasonic P-wave transducers were used to test common materials such as steel, aluminum, and acrylic, which have all been extensively tested and have available published results for comparison purposes.

The additional aspect of this research included the modification and development of the cubic triaxial setup for velocity testing. Although the cubic triaxial has been utilized already at the MIT geotechnical laboratory, it was only used for permeability measurements without further consolidation of the specimen. This setup was developed for the capabilities of measuring P and S-wave velocities during K_0 consolidation of the cubic specimen.

8.2 Interpretation of Velocity Results

With the conclusion of the experimental program, the performance of bender elements has been sufficiently assessed to ensure a confident interpretation of the obtained output signals. The parametric study conducted with different bender element tip geometries showed the significance that the tip geometry has on the signals that are transmitted. The long, slender geometry was shown to more likely produce directly-traveling P-waves as opposed to shorter, wider geometries, which can be attributed to the amount of axial displacement of the bender element with respect to its original position, which induces weak P-wave signals in addition to directly-traveling S-waves and side-traveling P-waves. Altering the specimen geometry allowed for the elimination of side-traveling wave interactions with the received signal allowing for a more confident assessment of the arrival of the directly-traveling signals. The ray path analysis showed the possible arrival times of various waves depending on the classification of the first arrival wave, which also made it clear that for long, slender bender tip geometries, a weak P-wave arrival can be expected. This supported the further use

of the short, wide bender element tips in order to eliminate ambiguities and maintain the bender element as a device that singularly measures S-wave velocities to avoid complications in signal interpretations. Additionally, after conducting extensive ray path analyses and modifying the specimen geometry, the optimal experimental setup chosen for further velocity testing in clays was the cubic triaxial setup. This prevents side-boundary reflections that can interfere with signal interpretation and enables an easier mounting configuration for the introduction of horizontal velocity testing.

It was also observed that for the ranges of stress and frequency tested, which consisted of 50-1600kPa and 2-8kHz, the results remained consistent irregardless of the input frequency used. The selected input voltage similarly did not show any effect on the travel times of the waves but did indicate a increase in amplitude directly proportional to an increase in the input voltage. This is a useful behavior to note when transitioning to higher stress levels that exhibit weak signals. The stress level applied to the specimen corresponds to the amplitude of the signal, as well as show an increasing trend in the measured velocity. As the stress increases, the stiffness properties of the specimen also increase, leading to a roughly logarithmic trend of velocity as a function of stress level, proven consistently with the experiments conducted on both Ticino sand and BBC.

The unloading behavior of BBC introduced an interesting trend reversal evident when comparing the compression curves and the shear modulus curves of a specimen of BBC in semi-log space. The swelling behavior during unloading becomes more pronounced, indicated by an increase in the absolute C_s value of a e-logσ'_{vc}. On the other hand, the shear modulus tends to maintain the increased stiffness even as the specimen is unloaded, which is more exaggerated as higher stress regimes are encountered. This indicates that when soils have been overconsolidated, the stiffness level after unloading is likely higher than usually expected, thus causing underestimations of stiffness parameters which can lead to inaccurate deformation predictions. Studies such as [Santagata, 1998] attempt to describe the OCR effect on the stiffness parameters; however, the amplitude of stiffness is generally underestimated with respect to the actual values. The bender element results propose a more significant impact on

the stiffness results attributed to hysteretic effects.

8.3 Equipment Effect on Stiffness Parameters

The appropriate method that should be used to measure the stiffness parameters of a material have long been a topic of debate. The results can greatly vary as a function of the technique used employed in the experimentation, which was evident through the parametric study conducted on common materials using both dynamic wave propagation testing as well as static deformation measurements. The reliability of extensometers, which are based on on-specimen strain gauge measurements, was supported by the results obtained during this research. P-wave transducers were also found to yield reliable results that were consistent with the extensometers, however the use of accelerometer is still a topic of discussion. During this experimental program, they proved to be unreliable for S-wave measurements; however, they did exhibit somewhat consistent results for the P-waves, especially when directly mounted on the specimen and separated by a substantial distance (1m) that allowed the waves to separate. The limiting factor for the accelerometers is also the natural resonant frequency. In the case of the ones used for this research, the $f_n = 5.5kHz$, which renders testing above this frequency sub-optimal. Additionally, the geometry of the specimen is a parameter that can determine the ability to use these various forms of measuring the elastic properties. In the case of the P-wave transducer, if the medium is highly attenuative, only short distances can be used, whereas the accelerometers work well for long distances and long wavelengths.

8.4 Future Work

There are many areas related to this work that warrant further research, both topics that were briefly covered in this research as well as other topics not addressed. Since this field of research is relatively new to the geotechnical engineering environment, there is much work to be done in order to accumulate a coherent understanding of

velocity testing in soils.

The first area of expansion is the actual testing of cubic specimens in the triaxial setup to obtain shear velocity measurements using bender elements and compressional wave velocity measurements using ultrasonic P-wave transducers. A systematic testing of a particular soil needs to be conducted over a wide range of stress level, ranging from very low stresses (50kPa), when bender elements are optimal, up to high stresses of 1MPa when the P-wave transducers will acquire signals that reflect the P-wave velocity through the soil rather than only through water. Both forms of equipment would be concurrently used throughout the duration of the experiment to the best of their ability. While the capacity of the current triaxial cell used for this research would only permit reaching a level of 1MPa, further modifications can be implemented to reach higher stress levels. The aim would be to eventually reach a stress of 100MPa, which would allow for a more comprehensive set of velocity measurements.

Related to the first topic that can be further researched is the inclusion of shear ultrasonic transducers in addition to the bender elements and P-wave ultrasonic transducers. When the stress level is reached at which the bender elements can no longer deflect due to the confining pressure, the ultrasonic S-wave transducer can be utilized to continue to high stresses with the capability of obtaining S and P-waves concurrently up to 100MPa

With the development of the experimental tested indicated above, the addition of horizontal velocity measurements would allow for the characterization of the anisotropy matrix. As described in section 2.5, the horizontal P and S-wave velocities are needed to complete the stiffness matrix for a cross-anisotropic medium. This could be seamlessly integrated onto the vertical surfaces of the cubic specimens. Furthermore, a verification of cross-anisotropic behavior can be conducted by performing horizontal velocity measurements in two distinct directions. One component needed to be explored for the completion of the stiffness matrix is obtaining the P-wave velocity in the 45° angle, which could be obtained by sending a wave from the side transducer and receiving it at an axial transducer.

While the effect of OCR and the unloading stress path was introduced in this

research, a further study is warranted. With additional testing, the unloading portion can be characterized systematically as a function of OCR and maximum stress level, which would permit a better understanding of velocity behavior during unloading of soils. While the unloading behavior in shales has been somewhat documented (i.e. [Bowers, 1995]), to the authors knowledge there have been no studies investigating the unloading velocity patterns associated with clays. Whereas unloading of shales can introduce cracking that would alter the results, clays would provide a better relationship between unloading and velocity independently of irreversible deformation mechanisms.

Due to the importance of pore pressure prediction in the field, a more in-depth look into the effect of pore pressures on velocity measurements is warranted. By inducing pore pressure in the triaxial setup and observing its effect on the clay specimen, an attempt to make a distinction between the undercompaction versus unloading behavior exhibited in the field can be made, both of which have a significant effect on the velocity measurements.

Finally, given the profound effects of bender element tip geometry on the velocity measurements, the geometry needs to be limited to a range where the P-waves are no longer a concern. This would eventually lead to an industry quality ASTM standard on the BE technique for soils.

Bibliography

[Abdulhadi, 2009] Abdulhadi, N. O. (2009). *An Experimental Investigation into the Stress-Dependent Mechanical Behavior of Cohesive Soil with Application to Wellbore Instability.* PhD thesis, Massachusetts Institute of Technology, Cambridge, MA, USA.

[Adams, 2011] Adams, A. L. (2011). Laboratory evaluation of the constant rate of strain and constant head techniques for measurement of the hydraulic conductivity of fine grained soils. Master's thesis, Massachusetts Institute of Technology, Cambridge, MA, USA.

[Alramahi et al., 2008] Alramahi, B., Alshibli, K. A., Fratta, D., and Trautwein, S. (2008). A suction-control apparatus for the measurement of p and s-wave velocity in soils. *Geotechnical Testing Journal*, 31(1):1–12.

[Asaka et al., 2008] Asaka, Y., Zhou, Y.-g., Abe, T., and Chen, Y.-m. (2008). Surface-mounted bender elements for measuring horizontal shear wave velocity of soils. *Journal of Zhejiang University Science A*, 9(11):1490–1496.

[Bowers, 1995] Bowers, G. L. (1995). Pore pressure estimation from velocity data: Accounting for overpressure mechanisms besides undercompaction. *SPE Drilling and Completion*, 10(2):89–95.

[Bowers, 2001] Bowers, G. L. (2001). Determining an appropriate pore-pressure estimation strategy. In *Offshore Technology Conference, 30 April-3 May 2001, Houston, Texas*, pages 1–14. Offshore Technology Conference.

[Callister and Rethwisch, 2011] Callister, W. and Rethwisch, D. (2011). *Fundamentals of Materials Science and Engineering: An Integrated Approach.* John Wiley & Sons.

[Casey, 2011] Casey, B. A. (2011). The significance of specimen end restraint in high pressure triaxial testing of cohesive soil. Master's thesis, Massachusetts Institute of Technology, Cambridge, MA, USA.

[Cauble, 1996] Cauble, D. (1996). *An Experimental Investigation of the Behavior of a Model Suction Caisson in a Cohesive Soil.* PhD thesis, Massachusetts Institute of Technology, Cambridge, MA, USA.

[Cha and Cho, 2007] Cha, M. and Cho, G.-C. (2007). Shear strength estimation of sandy soils using shear wave velocity. *Geotechnical Testing Journal*, 30(6):1–12.

[Chan, 2010] Chan, C.-M. (2010). Bender element test in soil specimens: Identifying the shear wave arrival time. *Electronic Journal of Geotechnical Engineering*, 15:1263–1276.

[Cho and Finno, 2010] Cho, W. and Finno, R. J. (2010). Stress-strain responses of block samples of compressible chicago glacial clays. *Journal of Geotechnical and Geoenvironmental Engineering*, 136(1):178–188.

[Dellinger and Vernik, 1994] Dellinger, J. and Vernik, L. (1994). Do traveltimes in pulse-transmission experiments yield anisotropic group or phase velocities? *Geophysics*, 59(11):1774–1779.

[Dewhurst and Siggins, 2006] Dewhurst, D. N. and Siggins, A. F. (2006). Impact of fabric, microcracks and stress field on shale anisotropy. *Geophysical Journal International*, 165(1):135–148.

[Ferreira et al., 2007] Ferreira, C., Fonseca, A., and Santos, J. A. (2007). Comparison of simultaneous bender elements and resonant column tests on porto residual soil. In Ling, H. I., Callisto, L., Leshchinsky, D., Koseki, J., and Gladwell, G., editors, *Soil Stress-Strain Behavior: Measurement, Modeling and Analysis*, volume 146 of *Solid Mechanics and Its Applications*, pages 523–535. Springer Netherlands. 10.1007/978-1-4020-6146-2-34.

[Fioravante and Capoferri, 2001] Fioravante, V. and Capoferri, R. (2001). On the use of multi-directional piezoelectric transducers in triaxial testing. *Geotechnical Testing Journal (GTJ)*, 24(3):243–255.

[Gajo et al., 1997] Gajo, A., Fedel, A., and Mongiovi, L. (1997). Experimental analysis of the effects of fluid-solid coupling on the velocity of elastic waves in saturated porous media. *Geotechnique*, 47(5):993–1008.

[Germaine, 1982] Germaine, J. T. (1982). *Development of the Directional Shear Cell for Measuring Cross Anisotropic Clay Properties.* PhD thesis, Massachusetts Institute of Technology, Cambridge, MA, USA.

[Germaine and Germaine, 2009] Germaine, J. T. and Germaine, A. (2009). *Geotechnical Laboratory Measurements for Engineers.* John Wiley and Sons Inc, Hoboken, New Jersey.

[Gist, 1994] Gist, G. (1994). Interpreting laboratory velocity measurements in partially gas-saturated rocks. *Geophysics*, 59:1100.

[Gonzalez, 2000] Gonzalez, J. H. (2000). Experimental and theoretical investigation of constant rate of strain consolidation. Master's thesis, Massachusetts Institute of Technology, Cambridge, MA, USA.

[Harper, 2001] Harper, C. (2001). *Handbook of materials for product design.* McGraw-Hill handbooks. McGraw-Hill.

[Hofmann, 2006] Hofmann, R. (2006). *Frequency Dependent Elastic and Anelastic Properties of Clastic Rocks.* PhD thesis, Colorado School of Mines, Golden, CO, USA.

[Horan, 2012] Horan, A. J. (2012). The mechanical behavior of normally consolidated soil as a function of pore fluid salinity. Master's thesis, Massachusetts Institute of Technology, Cambridge, MA, USA.

[Isenhower et al., 1987] Isenhower, W. M., Stokoe, K., and Allen, J. (1987). Instrumentation for torsional shear/resonant column measurements under anisotropic stresses. *ASTM International*, 10(4):183–191.

[Iwasaki et al., 1978] Iwasaki, T., Tatsuoka, F., and Takagi, Y. (1978). Shear moduli of sands under cyclic torsional shear loading. *Soils and Foundations*, 18(1):39–56.

[Jardine, 1995] Jardine, R. (1995). One perspective of the pre-failure deformation characteristics of some geomaterials. In *Proc. Int. Symp. Pre-failure Deformation Characteristics of Geomaterials*, volume 2, pages 855–85. AIS-Hokkaido '94.

[Johnson, 2011] Johnson, S. M. (2011). Modeling a bender element test using abaqus finite element program. Master's thesis, Massachusetts Institute of Technology, Cambridge, MA, USA.

[Jovicic et al., 1996] Jovicic, V., Coop, M. R., and Simic, M. (1996). Objective criteria for determining gmax from bender element tests. *Geotechnique*, 46(2):357–362.

[Kim and Stokoe, 1992] Kim, D.-S. and Stokoe, K. (1992). Characterization of resilient modulus of compacted subgrade soils using resonant column and torsional shear tests. In *Transportation Research Record No.1369*, pages 83–90. Advances in Geotechnical Engineering.

[Kuila et al., 2011] Kuila, U., Dewhurst, D. N., Siggins, A. F., and Raven, M. D. (2011). Stress anisotropy and velocity anisotropy in low porosity shale. *Tectonophysics*, 503(1-2):34–44.

[Landon, 2004] Landon, M. M. (2004). Field quantification of sample disturbance of a marine clay using bender elements. Master's thesis, University of Massachusetts, Amherst, Amherst, MA, USA.

[Lee and Santamarina, 2005] Lee, J.-S. and Santamarina, J. C. (2005). Bender elements: Performance and signal interpretation. *Journal of Geotechnical and Geoenvironmental Engineering*, 131(9):1063–1070.

[Leong et al., 2009] Leong, E. C., Cahyadi, J., and Rahardjo, H. (2009). Measuring shear and compression wave velocities of soil using benderextender elements. *Canadian Geotechnical Journal*, 46(7):792–812.

[Mavko et al., 2003] Mavko, G., Mukerji, T., and Dvorkin, J. (2003). *The Rock Physics Handbook: Tools for Seismic Analysis of Porous Media.* Stanford-Cambridge Program. Cambridge University Press.

[Mondol et al., 2008] Mondol, N. H., Jahren, J., Bjorlykke, K., and Brevik, I. (2008). Elastic properties of clay minerals. *The Leading Edge*, 27(6):758–770.

[Nihei et al., 2011] Nihei, K. T., Nakagawa, S., Reverdy, F., Myer, L. R., Duranti, L., and Ball, G. (2011). Phased array compaction cell for measurement of the transversely isotropic elastic properties of compacting sediments. *Geophysics*, 76(3):WA113–WA123.

[Nishimura, 2005] Nishimura, S. (2005). *Laboratory Study on Anisotropy of Natural London Clay.* PhD thesis, Imperial College London, London, UK.

[Pestana-Nascimento, 1994] Pestana-Nascimento, J. M. (1994). *A Unified Constitutive Model for Clays and Sands.* PhD thesis, Massachusetts Institute of Technology, Cambridge, MA, USA.

[Piane et al., 2011] Piane, C. D., Dewhurst, D. N., Siggins, A. F., and Raven, M. D. (2011). Stress-induced anisotropy in brine saturated shale. *Geophysical Journal International*, 184(2):897–906.

[Santagata, 1998] Santagata, M. C. (1998). *Factors Affecting the Initial Stiffness and Stiffness Degradation of Cohesive Soils.* PhD thesis, Massachusetts Institute of Technology, Cambridge, MA, USA.

[Sarout and Gueguen, 2008] Sarout, J. and Gueguen, Y. (September-October 2008). Anisotropy of elastic wave velocities in deformed shales: Part 1 experimental results. *Geophysics*, 73(5):D75–D89.

[Shirley and Hampton, 1978] Shirley, D. J. and Hampton, L. D. (1978). Shear-wave measurements in laboratory sediments. *The Journal of the Acoustical Society of America*, 63(2):607–613.

[Stein and Wysession, 2003] Stein, S. and Wysession, M. (2003). *An Introduction to Seismology, Earthquakes, and Earth Structure.* Blackwell Pub.

[Van Der Hilst, 2004] Van Der Hilst, R. (2004). Massachusetts Institute of Technology: MIT OpenCourseWare. Accessed 1 May, 2012, License: Creative Commons BY-NC-SA.

[Viggiani and Atkinson, 1995] Viggiani, G. and Atkinson, J. H. (1995). Interpretation of bender element tests. *Geotechnique*, 45:149–152.

[Wang et al., 2007] Wang, Y. H., Lo, K. F., Yan, W. M., and Dong, X. B. (2007). Measurement biases in the bender element test. *Journal of Geotechnical and Geoenvironmental Engineering*, 133(5):564–574.

[Yamashita et al., 2004] Yamashita, S., Fujiwara, T., Kawaguchi, T., and Mikami, T. (2004). *International Parallel Test on the Measurement of Gmax Using Bender Elements Organized by TC-29.* Japanese Domestic Committee for TC-29.

[Youn et al., 2008] Youn, J.-U., Choo, Y.-W., and Kim, D.-S. (2008). Measurement of small-strain shear modulus gmax of dry and saturated sands by bender element, resonant column, and torsional shear tests. *Canadian Geotechnical Journal*, 45(10):1426–1438.

[Zeng and Ni, 1999] Zeng, X. and Ni, B. (1999). Stress-induced anisotropic gmax of sands and its measurement. *Journal of Geotechnical and Geoenvironmental Engineering*, 125(9):741–749.

[Zimmer, 2003] Zimmer, M. A. (2003). *Seismic Velocities in Unconsolidated Sands: Measurements of Pressure, Sorting, and Compaction Effects.* PhD thesis, Stanford University, Stanford, CA, USA.